# ADAPTIVE AND HIGH ORDER METHODS FOR TIME DOMAIN BOUNDARY ELEMENTS

*by*

David Stark

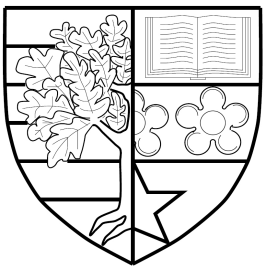

Submitted for the degree of
Doctor of Philosophy

Department of Mathematics
School of Mathematical and Computer Sciences
Heriot-Watt University

March 2018

# Abstract

This thesis concerns efficient and accurate time domain boundary element methods for the wave equation, with an emphasis on wave scattering in singular geometries and also towards higher frequencies in $3d$.

The work focuses on three approaches: Mesh refinements, as obtained in adaptive boundary elements or with algebraically graded meshes; a $p$-version of the boundary element method; and generalized boundary elements based on enriching the approximation spaces with either singular functions or plane waves. An application to traffic noise addresses computations for the sound amplification in the singular horn geometry between tyre and road.

The thesis first shows that algebraically graded meshes recover quasi-optimal convergence rates in polyhedral domains. For more general singularities of the solution, adaptive mesh refinements based on residual and Zienkiewicz-Zhu a posteriori error indicators lead to improved convergence rates. In benchmark examples for wave scattering on screens the convergence rates recover the rates known for time-independent problems.

Then a $p$-version of the time domain boundary element method is presented, based on increasing the polynomial degree on a fixed coarse space-time mesh. Compared to the standard $h$-version the $p$-methods are shown to double the convergence rate on screens.

Generalized boundary elements are studied for both screen and plane-wave scattering. For screens the ansatz and test functions are enriched with the singular functions known from the asymptotic expansion of the exact solution near edges and corners. For plane-wave scattering enrichments based on plane waves are presented. In examples we obtain a rapid convergence to engineering accuracy even on coarse meshes.

The work is supplemented with the study of an efficient preconditioner for the linear systems arising in the time domain method. It leads to efficient computation times for a wide range of discretisations.

# Acknowledgements

Firstly, I would like to thank my supervisor Dr. Heiko Gimperlein for introducing me to finite and boundary element methods, for teaching me how to simulate physical phenomena generally, for indulging my wider queries in science, and for his patience over the last 4 years. His impressive knowledge and ability has shaped my research and bestowed upon me good understanding.

I also wish to thank Prof. Jon Trevelyan and Prof. Dugald Duncan, both for agreeing to examine my work and for their expert suggestions and discussions relating to my work. Thanks also must go to Prof. Omar Laghrouche and Dr. M. Shadi Mohamed in the Institute for Infrastructure and Environment, who have let me engage and converse within their research group during regular meetings and conference visits, and introduced me to the wider area of computational mechanics.

Since the chapters in this work are based on a collection of papers, I wish to thank all of my co-authors for a fruitful cooperation. In particular, I wish to thank Ceyhun Özdemir for his help in understanding and implementing TDBEM code, for his regular discussions, and for executing various experiments.

Finally, I wish to also thank the EPSRC for providing funding for my doctoral work. I also appreciate the small grants and studentships I received from the IMA and LMS for attending and presenting at various conferences throughout my studies.

# Contents

# List of Tables

# List of Figures

# Chapter 1

# Introduction

Modern industrial applications relating to transient phenemona, such as environmental noise [22] or electromagnetic scattering [129], require fast and efficient numerical methods. One such method, the Boundary Element Method (BEM) has gained popularity over many decades, due to its advantages for scattering and emission problems over the Finite Element Method (FEM). Based on an exact representation of the solution in the interior, BEM reduces the computation from an $n$-dimensional, possibly unbounded domain to its ($n$-1)-dimensional boundary, and only requires the discretisation of the boundary conditions. For the linear wave equation, time-dependent boundary element methods (TDBEM) were recently surveyed in [71, 108].

We consider transient sound radiation problems in the exterior of a scatterer $\Omega^-$, where $\Omega^-$ is a bounded polygon with connected complement $\Omega = \mathbb{R}^3 \setminus \Omega^-$. The acoustic sound pressure field $u(t,x)$ due to an incident field or sources on $\Gamma = \partial\Omega$ satisfies the linear wave equation for $t \in \mathbb{R}$:

$$\begin{aligned} c_s^{-2}\partial_t^2 u(t,x) - \Delta u(t,x) &= 0 \quad \text{for } x \in \Omega \\ u(t,x) &= f(t,x) \quad \text{for } x \in \Gamma \\ u(t,x) &= 0 \quad \text{for } t \leq 0. \end{aligned} \tag{1.1}$$

Here $c_s$ denotes the wave velocity, and we set $c_s = 1$ for simplicity. From a single-layer

ansatz,

$$u(t,x) = \int_\Gamma \frac{\phi(t-|x-y|,y)}{4\pi|x-y|} ds_y \qquad \text{for } x \in \Omega \tag{1.2}$$

where $\phi$ is the density, with $\phi = 0$ for $t \leq 0$ due to causality of the wave equation, and the integration is over $y$. With the Dirichlet boundary conditions (1.1), we obtain an equivalent formulation of (1.1) as integral equation

$$V\phi(t,x) = \int_\Gamma \frac{\phi(t-|x-y|,y)}{4\pi|x-y|} ds_y = f(t,x) \qquad \text{for } x \in \Gamma. \tag{1.3}$$

With a focus on the single-layer equation (1.3), this thesis presents various approaches to efficiently solve time-domain boundary integral equations, and improve the convergence rates of these methods. We consider mesh refinements (space and space-time adaptive methods, algebraically-graded meshes), $p$-methods, and enriched methods based on non-polynomial basis functions. The forthcoming chapters will deal with each of these approaches in turn, discussing their implementation, some fundamental error analysis relating to the approach, and experimental results which have been obtained with each method. This will be introduced in more detail below.

Computationally, this work builds upon the $h$-TDBEM Galerkin method implemented by Ostermann [102]. Related earlier implementations go back to the French school around Nedelec [120, 72]. Our code solves a weak form of Equation (1.3) using a carefully-chosen quadrature method, and forms the foundation of the various novel methods presented in this thesis.

Starting with some work on mesh refinements, Chapter 4 focuses on static, algebraically-graded meshes for the edge and corner singularities which arise in polyhedral domains and screens. Such refinements are shown to produce quasi-optimal convergence, and we test this on a series of screen geometries, complemented by an error analysis. This chapter is based on paper [61] with H. Gimperlein, F. Meyer, C. Oezdemir and E.P. Stephan.

Chapter 5 then introduces adaptive methods. First we consider static mesh refine-

ments (space-only adaptivity), where mesh refinements are steered using an a posteriori residual-based error indicator which is time-averaged. Details of the implementation are explained, along with a series of results on various geometries. This space-adaptive work is published in [58] and includes the a posteriori error analysis behind the residual based indicator. We then move on to preliminary results towards dynamic mesh refinements (space-time adaptivity), where we remove the time-averaging of the error indicator. This method allows us to efficiently solve travelling-wave problems, since we can track the location of the largest errors in time. We present details of the implementation and a collection of experimental results.

In Chapter 6, we consider a space-time $p$-method, which converges at twice the rate of the $h$-TDBEM. The algorithmic considerations are discussed along with some analysis relating to the convergence of $p$-methods. This work can be found in [63].

Chapter 7 introduces a partition-of-unity method (PU-TDBEM). This involves using a linear polynomial basis in time, constant in space, and then enriching these shape functions with non-polynomial basis functions; here we enrich with a collection of plane-waves, and seek to solve problems relating to plane wave scattering on various geometries. This chapter relates to work in [62].

Chapter 8 focuses on solving issues relating to the linear system, and in particular a preconditioner which we have developed for their efficient solution. We test this preconditioner on a variety of problems and consider it as both a preconditioner for GMRES and as a stand-alone solver. The details are presented here along with our results, where we have taken this from our work [64]. Other issues related to the solving of the systems are discussed in this chapter.

# Chapter 2

# Background

## 2.1 Background in TDBEM

Hyperbolic boundary integral equations in the time-domain go back to Friedman and Shaw [52] and Cruse and Rizzo [37], who also considered numerical approaches to approximate them. The first modern boundary element methods were developed by Mansur [92], where one can also find some of the first basic algorithmic approaches behind current codes. The analysis of time-dependent Galerkin boundary element methods was initiated in the late 1980s in France by Bamberger and Ha-Duong [16]. This work provided the first weakly-coercive and stable formulation, and is the basis for the approach we follow here. Some relevant works on the numerical implementation of the resulting marching-in-on-time scheme include the Ph.D. thesis of Terrasse [120] and [42, 70], which made the methods competitive for commercial applications.

This approach of Bamberger and Ha-Duong is based on an analysis in the frequency domain. Using the Laplace transform to translate between frequency and time domain, well-posedness and convergence of numerical approximations can be analysed for the infinite time interval $[0, \infty)$. In more recent years, works by Aimi and collaborators [3, 5, 6, 7] emphasize formulations directly related to the conserved energy of the wave equation on a finite time interval $[0, T)$. At the expense of a slightly more involved weak formulation, the intrinsic coercivity directly implies the stability and convergence of these methods. However, the analysis of these methods still seems to be restricted to one dimension or

simple, specific geometries.

A thorough description of the mathematical background of time domain integral equations and their discretisations can be found in the lecture notes of Sayas [108]. For a more concise introduction, one can find this in [35, 71]. [46] is a good source for recent progress in the area.

Compared to frequency-domain methods, time-domain approaches have clear advantages when one considers a broad band of frequencies. Only one computation is required for the whole frequency range to be considered. Time-domain methods are also of particular interest for problems beyond the reach of frequency domain methods, such as the simulation of transient dynamics, moving sound sources or nonlinear and dynamical contact problems. They can also be applied to obtain results in frequency domain, for all frequencies in one computation, using the Fourier transform to move interchangeably between time and frequency.

Time-domain methods are potentially as fast and efficient as the more heavily studied frequency-domain methods. Depending on the problem, they can be more efficient (if one is interested in a broad range of frequencies). Time-domain methods can also be applied to nonlinear problems such as those relating to contact or crack propagation. Fast Multipole methods for frequency-domain problems have been implemented, allowing large reductions in computation times when assembling the stiffness matrix. A similar approach is yet to be implemented for time-domain problems, but the challenges here are very similar since multipoles exist in both problems [119].

We focus on solving the Dirichlet problem here, which requires only the single-layer operator. For Neumann and Robin problems, other operators (double-layer, adjoint double-layer, and hypersingular) are required. Our Green's function (fundamental solution to the wave equation), is singular in both 2D and 3D. This is the main challenge of the quadrature needed to assemble the entries of the Galerkin matrix. The discretisation and

accurate computation of the entries in the Galerkin matrix has been considered in detail by Maischak, Ostermann and Stephan [89, 115], and algorithmic details can be found in the PhD thesis of Ostermann [102]. This is the approach we follow in this work, and our various implementations are built upon the quadrature method presented there. There are alternative Galerkin approaches however e.g. [8]. Collocation methods also have been studied in the engineering literature - see [129] for details, where computations can be performed much faster than with Galerkin methods, but suffer a lack of any mathematical analysis, and as such are unable to guarantee stability. As an alternative to space-time Galerkin boundary elements entirely, recently there has been fast progress using convolution quadrature methods [19, 18, 108].

With respect to physical applications, efficient and accurate computational methods to simulate sound emission in space and time are of interest in many areas; from the modeling of environmental noise to the acoustics of concert halls. Recent work in vehicle tyre noise has been studied extensively in [22, 56, 58], where both analysis and algorithmic details are provided for a range of experiments. In the engineering literature, fast methods are being developed and studied especially in the group of Eric Michielssen, see e.g. [129]. Further engineering applications involve wave propagation in moving coordinate systems or with moving sources [10, 106]. Alternative ansatz functions in time have also been explored in [39, 40].

We consider efficient convergence ourselves, using mesh refinements and $p$-methods/enriched methods, but there are other directions being pursued. For interface problems, Abboud, Joly, Rodriguez and Terrasse [1] initiated the mathematical analysis of FEM-BEM coupling in the time domain, coupling discontinuous finite elements to time domain integral equations. A subsequent work by Banjai, Lubich and Sayas [20] provides the fundamental analysis of the coupling between different discretisations (including convolution quadrature). Certain truly transient phenomena studied by engineers cannot be simulated in the frequency domain because they involve nonlinear contact and damage. See [76, 113] for time domain BEM approaches to such problems. Their mathematical analysis remains a

challenge for future work.

## 2.2 Algebraically-Graded Meshes

Regarding the solutions of elliptic or parabolic equations in a polyhedral domain, the asymptotic behaviour near the edges and corners has been studied for several decades [94]. The explicit singular expansions near edges and corners allow one to numerically achieve optimal convergence rates for finite element [12, 15] and boundary element methods [124, 125].

In the hyperbolic case (where domains contain conical or wedge singularities), a similar asymptotic behavior has been obtained in work by Plamenevskii and his collaborators [84, 86, 93, 105]. Their results imply that at a fixed time $t$, the solution to the wave equation admits an explicit singular expansion with exactly the same behaviour as with elliptic equations. Recently, the work of Müller and Schwab has taken these results and used them to obtain optimal convergence rates for a finite element method in polygonal domains in $\mathbb{R}^2$ [98].

Geometric singularities have a very significant impact on the realistic scattering and diffraction of waves in $\mathbb{R}^3$. In Chapter 4, we consider such problems in the limiting case of a singular geometry - a screen $\Gamma$ in $\mathbb{R}^3$. Physically, such a domain could be interpreted as an opening crack or a thin scatterer. We also apply what we have studied here to the problem of tyre sound emission, and examine the related resonances there. Similar singularities arise also for other integral equations, such as fractional Laplace equations. Also in this context, graded meshes have been studied recently. *hp*-graded meshes studied on elliptic problems by Heuer et al. [78] show exponential convergence.

Work by Chandler-Wilde et al, such as in [34], considers scattering from polygons and screens, where algebraically-graded meshes form a key component.

## 2.3 Adaptive Mesh Refinements

Adaptive mesh-refinement methods are known to improve the convergence rate of Finite element and Boundary element discretisations. Standard textbooks in this area include [41, 112]. In this work, we consider both space-adaptive TDBEM methods and space-time adaptive TDBEM methods.

Numerically, the efficient treatment of boundary integral equations using adaptive mesh refinement procedures has been extensively studied in the elliptic case, for homogeneous problems [27, 29]. [69] provides recent advancements in this area.

Recently, a significant amount of interest in the solution of such problems on adapted meshes has appeared. As in the elliptic case, singularities of the solution can appear at singular points of the boundary - an extensive discussion of this can be found in [105, 84, 85], and also in trapping regions. Some first steps towards time-adaptivity have been made by Sauter and Veit [109] in 2 dimensions, and also with convolution quadrature methods - where graded, non-adaptively chosen time steps have been studied, for example in [111]. The PhD thesis of Gläfke [66] provided some first results towards space-time refinements in 2 dimensions, which is our starting point for going into 3-dimensions. The challenges in 3 dimensions include computing on much larger meshes. Lastly, in unpublished work, Abboud investigates the Zienkewicz-Zhu (ZZ) type error indicators for screen problems, where error-analysis is lacking due to the heuristic nature of his indicator. Our work considers both this ZZ indicator and our mathematically-rigorous residual-based indicators.

Our work in adaptive methods (Chapter 5) extends the numerical analysis of adaptive boundary element methods for Laplace's equation, both for Symm's integral equation and the hypersingular equation [27, 29, 30, 31]. We note that there exists work on different error indicators (in the time-independent case), which includes both the ZZ [28] and Faermann indicators [49, 50]. We also refer to [128] for an earlier approach. Ultimately, future research will provide a comparison of different indicators in the time-domain. A natural direction would also be to design and implement a fully *hp*-adaptive space-time adaptive

TDBEM code. Our work in both adaptive methods and $p$-methods already provides the major steps necessary for such a development.

## 2.4 Partition-of-Unity Methods

Babuska and Melenk [95, 96] introduced and analysed the so-called partition-of-unity (PU) method. Their work suggests using non-polynomial ansatz and test functions (enriched basis functions), to include a priori knowledge about the behaviour of the solution into the approximation spaces. These enrichments may be either used alone or along with a standard polynomial basis functions. One challenge is to find a suitable choice of enrichment - particularly of an optimal nature. It is shown in previous work, however, that such methods result in rapid approximations with engineering accuracy - in particular for low degrees of freedom and on coarse meshes. Typically convergence plots show errors initially dropping rapidly, then stalling for higher numbers of degrees of freedom. A main disadvantage with these methods is that they can quickly provide ill-conditioned matrices; the large number of basis functions in each triangle leads to this, which poses challenges for the accurate solution of the resulting linear system, and limits the accuracy for high degrees of freedom, where the conditioning can push beyond the boundary of typical double-precision accuracy used in computational solvers. Examples of these methods include XFEM (extended finite element method), where singular functions are included as enrichments locally, such as near a crack tip [53], and the use of plane wave enrichments over a whole domain to capture the oscillatory behaviour of solutions to time-harmonic wave problems [117, 118]. In Chapter 7, we extend such work in frequency-domain to the time-domain and include space-time enrichments.

In frequency-domain problems, PU boundary elements have been shown to provide efficient numerical methods. The advantages of this approach are particularly noticable at high frequencies, where numerical pollution increases the required computational effort for other approaches. While pollution is still present in PU methods, its effect is reduced. Seminal works here include [88, 103, 104], where plane waves are included as enrichments

in a boundary element method. The plane waves are chosen such that their directions of propagation are distributed in a uniform fashion in all directions. In other work, methods have been tailored to very specific geometries or based on non-standard integral formulations such as in [33, 79].

PU methods recently have been attempted for transient problems; for wave propagation [45, 75] and also heat propagation [83, 97]. They extend work on the existing time-independent enrichment in space and use typical time-stepping schemes to reduce the time-dependent PDE to something time-independent, where the method can be explicitly used without much change.

# Chapter 3

# Boundary Integral Operators and Sobolev Spaces

To be specific, in $\mathbb{R}^3$ let $\Gamma$ be the boundary of a polyhedral domain, consisting of curved, polygonal boundary faces, or an open polyhedral surface (screen). In $\mathbb{R}^2$, $\Gamma$ is the boundary of a curved polygon, or $\Gamma$ is an open polygonal curve.

We make an ansatz for the solution to (1.1) using the single layer potential in time domain,

$$u(t,x) = \int_{\mathbb{R}^+ \times \Gamma} G(t-\tau, x, y)\ \phi(\tau, y)\ d\tau\ ds_y\ , \tag{3.1}$$

where $G$ is a fundamental solution to the wave equation

$$G(t-\tau, x, y) = \frac{\delta(t-s-|x-y|)}{4\pi|x-y|}$$

and $\phi(\tau, y) = 0$ for $\tau \leq 0$. Specifically in 3 dimensions, we may choose

$$u(t,x) = \frac{1}{4\pi} \int_\Gamma \frac{\phi(t-|x-y|, y)}{|x-y|}\ ds_y\ ,$$

but for applications to traffic noise also different choices are relevant, see (4.17). Taking the Dirichlet boundary values on $\Gamma$ of the integral (3.1), we obtain the single layer operator,

$$V\phi(t,x) = \int_{\mathbb{R}^+ \times \Gamma} G(t-\tau, x, y)\ \phi(\tau, y)\ d\tau\ ds_y\,,$$

It allows to reduce the wave equation (1.1) with Dirichlet boundary conditions, $u = f$ on $\Gamma$, to an equivalent integral equation

$$V\phi = u|_\Gamma = f \ . \tag{3.2}$$

After solving equation (3.2) for the density $\phi$, the solution to the wave equation is obtained using equation (3.1).

We also require the adjoint double layer operator $K'$, as obtained from the Neumann boundary values, as well as the double layer operator $K$ and the hypersingular operator $W$ on $\Gamma$:

$$\begin{aligned} K\phi(t,x) &= \int_{\mathbb{R}^+\times\Gamma} \frac{\partial G}{\partial n_y}(t-\tau,x,y)\ \phi(\tau,y)\ d\tau\ ds_y, \\ K'\phi(t,x) &= \int_{\mathbb{R}^+\times\Gamma} \frac{\partial G}{\partial n_x}(t-\tau,x,y)\ \phi(\tau,y)\ d\tau\ ds_y\,, \\ W\phi(t,x) &= \int_{\mathbb{R}^+\times\Gamma} \frac{\partial^2 G}{\partial n_x \partial n_y}(t-\tau,x,y)\ \phi(\tau,y)\ d\tau\ ds_y\ . \end{aligned} \tag{3.3}$$

The boundary integral operators are considered between space-time anisotropic Sobolev spaces $H^r_\sigma(\mathbb{R}^+, \widetilde{H}^s(\Gamma))$, see [56] or [71]. To define them, if $\partial\Gamma \neq \emptyset$, first extend $\Gamma$ to a closed, orientable Lipschitz manifold $\widetilde{\Gamma}$.

On $\Gamma$ one defines the usual Sobolev spaces of supported distributions:

$$\widetilde{H}^s(\Gamma) = \{u \in H^s(\widetilde{\Gamma}) : \text{supp } u \subset \overline{\Gamma}\}\ , \qquad s \in \mathbb{R}\ .$$

Furthermore, $H^s(\Gamma)$ is the quotient space $H^s(\widetilde{\Gamma})/\widetilde{H}^s(\widetilde{\Gamma}\setminus\overline{\Gamma})$.

To write down an explicit family of Sobolev norms, introduce a partition of unity $\alpha_i$ subordinate to a covering of $\widetilde{\Gamma}$ by open sets $B_i$. For diffeomorphisms $\phi_i$ mapping each $B_i$ into the unit cube $\subset \mathbb{R}^n$, a family of Sobolev norms, depending on a time-frequency variable $\omega \in \mathbb{C}\setminus\{0\}$, is induced from $\mathbb{R}^d$:

$$||u||_{s,\omega,\widetilde{\Gamma}} = \left(\sum_{i=1}^{p}\int_{\mathbb{R}^n} (|\omega|^2+|\xi|^2)^s |\mathcal{F}\left\{(\alpha_i u)\circ\phi_i^{-1}\right\}(\xi)|^2 d\xi\right)^{\frac{1}{2}}\ .$$

The norms for different $\omega \in \mathbb{C} \setminus \{0\}$ are equivalent, and $\mathcal{F}$ denotes the Fourier transform. They induce norms on $H^s(\Gamma)$, $||u||_{s,\omega,\Gamma} = \inf_{v \in \widetilde{H}^s(\widetilde{\Gamma} \setminus \overline{\Gamma})} ||u+v||_{s,\omega,\widetilde{\Gamma}}$, and on $\widetilde{H}^s(\Gamma)$, $||u||_{s,\omega,\Gamma,*} = ||e_+ u||_{s,\omega,\widetilde{\Gamma}}$. $e_+$ extends the distribution $u$ by 0 from $\Gamma$ to $\widetilde{\Gamma}$. It is stronger than $||u||_{s,\omega,\Gamma}$ whenever $s \in \frac{1}{2} + \mathbb{Z}$.

We now define a class of space-time anisotropic Sobolev spaces:

**Definition 1.** *For $r, s \in \mathbb{R}$ and $\sigma > 0$ define*

$$H^r_\sigma(\mathbb{R}^+, H^s(\Gamma)) = \{u \in \mathcal{D}'_+(H^s(\Gamma)) : e^{-\sigma t} u \in \mathcal{S}'_+(H^s(\Gamma)) \text{ and } ||u||_{r,s,\Gamma} < \infty\} ,$$
$$H^r_\sigma(\mathbb{R}^+, \widetilde{H}^s(\Gamma)) = \{u \in \mathcal{D}'_+(\widetilde{H}^s(\Gamma)) : e^{-\sigma t} u \in \mathcal{S}'_+(\widetilde{H}^s(\Gamma)) \text{ and } ||u||_{r,s,\Gamma,*} < \infty\} .$$

*$\mathcal{D}'_+(E)$ resp. $\mathcal{S}'_+(E)$ denote the spaces of distributions, resp. tempered distributions, on $\mathbb{R}$ with support in $[0,\infty)$, taking values in $E = H^s(\Gamma), \widetilde{H}^s(\Gamma)$. The relevant norms are given by*

$$\|u\|_{r,s,\Gamma} = \left( \int_{-\infty+i\sigma}^{+\infty+i\sigma} |\omega|^{2r} \ \|\hat{u}(\omega)\|^2_{s,\omega,\Gamma} \ d\omega \right)^{\frac{1}{2}} ,$$
$$\|u\|_{r,s,\Gamma,*} = \left( \int_{-\infty+i\sigma}^{+\infty+i\sigma} |\omega|^{2r} \ \|\hat{u}(\omega)\|^2_{s,\omega,\Gamma,*} \ d\omega \right)^{\frac{1}{2}} .$$

For $|s| \leq 1$ the spaces are independent of the choice of $\alpha_i$ and $\phi_i$.

A useful technical result localizes estimates for fractional Sobolev norms, extending [124, Lemma 3.2] to space-time:

**Lemma 2.** *Let $\Gamma$, $\Gamma_j$ $(j = 1, \ldots, N)$ be Lipschitz domains with $\overline{\Gamma} = \bigcup_{j=1}^N \overline{\Gamma}_j$, $\tilde{u} \in H^r_\sigma(\mathbb{R}^+, \widetilde{H}^s(\Gamma))$, $u \in H^r_\sigma(\mathbb{R}^+, H^s(\Gamma))$, $s \in \mathbb{R}$. Then for all $s \in [-1,1]$, $r \in \mathbb{R}$ and $\sigma > 0$*

$$\sum_{j=1}^N \|u\|^2_{r,s,\Gamma_j} \leq \|u\|^2_{r,s,\Gamma} , \tag{3.4}$$

$$\|\tilde{u}\|^2_{r,s,\Gamma,*} \leq \sum_{j=1}^N \|\tilde{u}\|^2_{r,s,\Gamma_j,*} . \tag{3.5}$$

The proof is an immediate extension of the time-independent case.

The boundary integral operators obey the following mapping properties between the space-time Sobolev spaces:

**Theorem 3** ([56]). *The following operators are continuous for $r \in \mathbb{R}$, $\sigma > 0$:*

$$V : H^{r+1}_\sigma(\mathbb{R}^+, \tilde{H}^{-\frac{1}{2}}(\Gamma)) \to H^r_\sigma(\mathbb{R}^+, H^{\frac{1}{2}}(\Gamma)) \ ,$$
$$K' : H^{r+1}_\sigma(\mathbb{R}^+, \tilde{H}^{-\frac{1}{2}}(\Gamma)) \to H^r_\sigma(\mathbb{R}^+, H^{-\frac{1}{2}}(\Gamma)) \ ,$$
$$K : H^{r+1}_\sigma(\mathbb{R}^+, \tilde{H}^{\frac{1}{2}}(\Gamma)) \to H^r_\sigma(\mathbb{R}^+, H^{\frac{1}{2}}(\Gamma)) \ ,$$
$$W : H^{r+1}_\sigma(\mathbb{R}^+, \tilde{H}^{\frac{1}{2}}(\Gamma))) \to H^r_\sigma(\mathbb{R}^+, H^{-\frac{1}{2}}(\Gamma)) \ .$$

When $\Gamma = \mathbb{R}^{n-1}_+$, Fourier methods yield improved estimates for $V$ and $W$:

**Theorem 4** ([73], pp. 503-506). *The following operators are continuous for $r, s \in \mathbb{R}$, $\sigma > 0$:*

$$V : H^{r+\frac{1}{2}}_\sigma(\mathbb{R}^+, \tilde{H}^s(\Gamma)) \to H^r_\sigma(\mathbb{R}^+, H^{s+1}(\Gamma)) \ ,$$
$$W : H^r_\sigma(\mathbb{R}^+, \tilde{H}^s(\Gamma)) \to H^r_\sigma(\mathbb{R}^+, H^{s-1}(\Gamma)) \ .$$

The space-time Sobolev spaces allow a precise statement and analysis of the weak formulation for the Dirichlet problem (3.2): Find $\psi \in H^1_\sigma(\mathbb{R}^+, \widetilde{H}^{-\frac{1}{2}}(\Gamma))$ such that for all $\Psi \in H^1_\sigma(\mathbb{R}^+, \widetilde{H}^{-\frac{1}{2}}(\Gamma))$

$$\int_0^\infty \int_\Gamma (V\psi(t,\mathbf{x}))\partial_t \Psi(t,\mathbf{x}) \ ds_x \ d_\sigma t = \int_0^\infty \int_\Gamma f(t,\mathbf{x})\partial_t \Psi(t,\mathbf{x}) \ ds_x \ d_\sigma t \ , \tag{3.6}$$

where $d_\sigma t = e^{-2\sigma t} dt$.

To obtain an analogous weak formulation for the Neumann problem, one starts from a double layer potential ansatz for $u$:

$$u(t,x) = \int_{\mathbb{R}^+ \times \Gamma} \frac{\partial G}{\partial n_y}(t-\tau, x, y) \ \phi(\tau, y) \ d\tau \ ds_y \tag{3.7}$$

with $\phi(s,y) = 0$ for $s \leq 0$. The corresponding integral formulation is the hypersingular equation

$$W\phi = \frac{\partial u}{\partial n}\Big|_\Gamma = g \ . \tag{3.8}$$

Find $\phi \in H^1_\sigma(\mathbb{R}^+, \widetilde{H}^{\frac{1}{2}}(\Gamma))$ such that for all $\Phi \in H^1_\sigma(\mathbb{R}^+, \widetilde{H}^{\frac{1}{2}}(\Gamma))$ there holds:

$$\int_{\mathbb{R}^+\times\Gamma} (W\phi(t,\mathbf{x}))\ \partial_t\Phi(t,\mathbf{x})\, d_\sigma t\, ds_x \ = \int_{\mathbb{R}^+\times\Gamma} g(t,\mathbf{x})\ \partial_t\Phi(t,\mathbf{x})\, dt\, ds_x \ . \tag{3.9}$$

The weak formulations (3.6), respectively (3.9), for the Dirichlet and Neumann problems are well-posed [56, 22]:

**Theorem 5.** *Let $\sigma > 0$.*

*a) Assume that $f \in H^2_\sigma(\mathbb{R}^+, H^{\frac{1}{2}}(\Gamma))$. Then there exists a unique solution $\psi \in H^1_\sigma(\mathbb{R}^+, \widetilde{H}^{-\frac{1}{2}}(\Gamma))$ of* (3.6) *and*

$$\|\psi\|_{1,-\frac{1}{2},\Gamma,*} \lesssim_\sigma \|f\|_{2,\frac{1}{2},\Gamma} \ . \tag{3.10}$$

*b) Assume that $g \in H^2_\sigma(\mathbb{R}^+, H^{-\frac{1}{2}}(\Gamma))$. Then there exists a unique solution $\phi \in H^1_\sigma(\mathbb{R}^+, \widetilde{H}^{\frac{1}{2}}(\Gamma))$ of* (3.9) *and*

$$\|\phi\|_{1,\frac{1}{2},\Gamma,*} \leq C\|g\|_{2,-\frac{1}{2},\Gamma} \ . \tag{3.11}$$

While a theoretical analysis requires $\sigma > 0$, practical computations use $\sigma = 0$ [16, 54].

With a view towards contact problems [113], we also consider an equation for the Dirichlet-to-Neumann operator $\mathcal{S}_\sigma$. For $\sigma > 0$ and given boundary data $u_\sigma$, we consider

$$\begin{cases} \left(\frac{\partial}{\partial t} + \sigma\right)^2 w_\sigma - \Delta w_\sigma = 0 \ , & \text{for } (t,x) \in \mathbb{R}\times\Omega \ , \\ w_\sigma = u_\sigma \ , & \text{for } (t,x) \in \mathbb{R}\times\Gamma \ , \\ w_\sigma = 0, & \text{for } (t,x) \in (-\infty,0)\times\Omega \ . \end{cases} \tag{3.12}$$

The Dirichlet-to-Neumann operator is defined as

$$\mathcal{S}_\sigma u_\sigma|_\Gamma := \left.\frac{\partial w_\sigma}{\partial n}\right|_\Gamma \ , \tag{3.13}$$

We recall from [107], p. 48:

**Theorem 6.** *Let $h \in H^{\frac{3}{2}}_\sigma(\mathbb{R}^+, H^{-\frac{1}{2}}(\Gamma))$. Then there exists a unique $u_\sigma \in H^{\frac{1}{2}}_\sigma(\mathbb{R}^+, \tilde{H}^{\frac{1}{2}}(\Gamma))$*

*such that for all* $v \in H_\sigma^{-\frac{1}{2}}(\mathbb{R}^+, \tilde{H}^{\frac{1}{2}}(\Gamma))$*:*

$$\langle \mathcal{S}_\sigma u_\sigma, v \rangle = \langle h, v \rangle \ . \tag{3.14}$$

# Chapter 4

# Algebraically-Graded Meshes

This chapter is based on joint work [61] with H. Gimperlein, F. Meyer, C. Ozdemir, and E.P. Stephan.

## 4.1 Introduction

The realistic scattering and diffraction of waves in $\mathbb{R}^3$ is crucially affected by geometric singularities of the scatterer, with significant new challenges for both pure and numerical analysis. In this chapter, we study the solution of the wave equation in the most singular case, outside a screen $\Gamma$ in $\mathbb{R}^3$ or, equivalently, for an opening crack. From the singular expansion we obtain optimal convergence rates for piecewise polynomial approximations on graded meshes. Numerical experiments using a time domain boundary element method confirm the theoretical predictions and show their use for a real-world application in traffic noise.

To be specific, for a polyhedral screen $\Gamma \subset \mathbb{R}^3$ with connected complement $\Omega = \mathbb{R}^3 \setminus \overline{\Gamma}$ we consider the wave equation

$$c^{-2}\partial_t^2 u(t,x) - \Delta u(t,x) = 0 \quad \text{in } \mathbb{R}^+_t \times \Omega_x \tag{4.1a}$$

$$Bu = g \quad \text{on } \Gamma = \partial\Omega \tag{4.1b}$$

$$u(0,x) = \partial_t u(0,x) = 0 \quad \text{in } \Omega \tag{4.1c}$$

where either inhomogeneous Dirichlet boundary conditions $Bu = u|_\Gamma$ or Neumann bound-

ary conditions $Bu = \partial_n u|_\Gamma$ are considered on $\Gamma$. Here, $c$ denotes the speed of sound and for simplicity, we mostly choose units such that $c = 1$. However, for computations on the tyre domain we use $c = 343$ ms$^{-1}$.

Based on the above-mentioned results of Plamenevskii and coauthors, we obtain a precise description of the singularities of the solution near edges and corners. The solution $u$ and its normal derivative on $\Gamma$ admit an asymptotic expansion with the same singular exponents as in the elliptic case.

As in the elliptic case, the precise asymptotic description of the solution has implications for the approximation by time domain boundary elements.

We approximate the solution on $\beta$-graded meshes. For example, on the circular screen of radius 1, for $\beta = 1$ we take a uniform mesh with nodes on concentric circles of radius $r_k = 1 - \frac{k}{N_l}$ for $k = 0, \ldots, N_l - 1$. For the $\beta$-graded mesh, the radii are moved to $r_k = 1 - (\frac{k}{N_l})^\beta$ for $k = 0, \ldots, N_l - 1$. A more complete definition is given in Section 4.2. We formulate (1.1) as a time dependent integral equation on $\Gamma$, with either the single layer, the hypersingular or the Dirichlet-to-Neumann operator. The Dirichlet trace $u|_\Gamma$ is approximated by tensor products of piecewise polynomial functions $\widetilde{V}^{p,q}_{\Delta t,h}$ on a $\beta$-graded mesh in space and a uniform mesh in time of step size $\Delta t$. $\tilde{V}^{p,q}_{\Delta t,h}$ is defined in (4.3), and its analogue $V^{p,q}_{\Delta t,h}$ for the approximation of the Neumann trace $\partial_n u|_\Gamma$ in (4.2). See the bottom of page 8 for the definition of the $\beta$-graded meshes. Our main result for the approximation of the solutions to the boundary integral equations in space-time anisotropic Sobolev spaces (Definition 1) is a consequence of:

**Theorem A.** *Let $\varepsilon > 0$.*

*a) Let $u$ be a strong solution to the homogeneous wave equation with inhomogeneous Neumann boundary conditions $\partial_n u|_\Gamma = g$, with $g$ smooth. Further, let $\phi^\beta_{h,\Delta t}$ be the best approximation in the norm of $H^r_\sigma(\mathbb{R}^+, \widetilde{H}^{\frac{1}{2}-s}(\Gamma))$ to the Dirichlet trace $u|_\Gamma$ in $\widetilde{V}^{p,1}_{\Delta t,h}$ on a $\beta$-graded spatial mesh with $\Delta t \lesssim h^\beta$. Then $\|u - \phi^\beta_{h,\Delta t}\|_{r,\frac{1}{2}-s,\Gamma,*} \leq C_{\beta,\varepsilon} h^{\min\{\beta(\frac{1}{2}+s),\frac{3}{2}+s\}-\varepsilon}$, where $s \in [0, \frac{1}{2}]$ and $r \in [0, p)$.*

*b) Let $u$ be a strong solution to the homogeneous wave equation with inhomogeneous*

*Dirichlet boundary conditions $u|_\Gamma = g$, with $g$ smooth. Further, let $\psi^\beta_{h,\Delta t}$ be the best approximation in the norm of $H^r_\sigma(\mathbb{R}^+, \widetilde{H}^{-\frac{1}{2}}(\Gamma))$ to the Neumann trace $\partial_n u|_\Gamma$ in $V^{p,0}_{\Delta t,h}$ on a $\beta$-graded spatial mesh with $\Delta t \lesssim h^\beta$. Then $\|\partial_n u - \psi^\beta_{h,\Delta t}\|_{r,-\frac{1}{2},\Gamma,*} \leq C_{\beta,\varepsilon} h^{\min\{\frac{\beta}{2},\frac{3}{2}\}-\varepsilon}$, where $r \in [0, p+1)$.*

For the circular screen this result may be found in Theorem 10, while for the polygonal screen it is Theorem 15 (assuming $\beta$ is sufficiently large). It implies an approximation result for the solution to the boundary integral formulations, see Corollary 11 for the circular screen, respectively Corollary 16 for the polygonal screen:

**Corollary B.** *Let $\varepsilon > 0$.*

*a) Let $\phi$ be the solution to the hypersingular integral equation $W\phi = g$ and $\phi^\beta_{h,\Delta t}$ the best approximation in the norm of $H^r_\sigma(\mathbb{R}^+, \widetilde{H}^{\frac{1}{2}-s}(\Gamma))$ to $\phi$ in $\widetilde{V}^{p,1}_{\Delta t,h}$ on a $\beta$-graded spatial mesh with $\Delta t \lesssim h^\beta$. Then $\|\phi - \phi^\beta_{h,\Delta t}\|_{r,\frac{1}{2}-s,\Gamma,*} \leq C_{\beta,\varepsilon} h^{\min\{\beta(\frac{1}{2}+s),\frac{3}{2}+s\}-\varepsilon}$, where $s \in [0, \frac{1}{2}]$ and $r \in [0, p)$.*

*b) Let $\psi$ be the solution to the single layer integral equation $V\psi = f$ and $\psi^\beta_{h,\Delta t}$ the best approximation in the norm of $H^r_\sigma(\mathbb{R}^+, \widetilde{H}^{-\frac{1}{2}}(\Gamma))$ to $\psi$ in $V^{p,0}_{\Delta t,h}$ on a $\beta$-graded spatial mesh with $\Delta t \lesssim h^\beta$. Then $\|\psi - \psi^\beta_{h,\Delta t}\|_{r,-\frac{1}{2},\Gamma,*} \leq C_{\beta,\varepsilon} h^{\min\{\frac{\beta}{2},\frac{3}{2}\}-\varepsilon}$, where $r \in [0, p+1)$.*

Indeed, on the flat screen the solutions to the integral equations are given by $\phi = [u]\,|_\Gamma$ in terms of the solution $u$ which satisfies Neumann conditions $Bu = \partial_n u|_\Gamma = g$, respectively $\psi = [\partial_n u]\,|_\Gamma$ in terms of the solution $u$ which satisfies Dirichlet conditions $Bu = u|_\Gamma = f$.

Note that the energy norm associated to the weak form of the single layer integral equation (3.6) is weaker than the norm of $H^1_\sigma(\mathbb{R}^+, H^{-\frac{1}{2}}(\Gamma))$ and stronger than the norm of $H^0_\sigma(\mathbb{R}^+, H^{-\frac{1}{2}}(\Gamma))$, according to the coercivity and continuity properties of $V$ on screens [56]. Similarly, for the weak form of the hypersingular integral equation (3.9), the energy norm is weaker than the norm of $H^1_\sigma(\mathbb{R}^+, H^{\frac{1}{2}}(\Gamma))$ and stronger than the norm of $H^0_\sigma(\mathbb{R}^+, H^{\frac{1}{2}}(\Gamma))$ [22].

**Remark C.** *Together with the a priori estimates for the time domain boundary element methods on screens [56, 22], Corollary B implies convergence rates for the Galerkin approximations, which recover those for smooth solutions (up to an arbitrarily small $\varepsilon > 0$) provided the grading parameter $\beta$ is chosen sufficiently large.*

We prove the approximation properties in detail on the circular screen, without corners, and discuss the approximation of the corner singularity on polygonal screens. On the square, the convergence rate is determined by the singularities at the edges, in spite of the smaller singular exponents in a corner. In all cases, we show that *time independent* algebraically graded meshes adapted to the singularities recover the optimal approximation rates expected for smooth solutions.

Numerical experiments confirm the theoretical results for the singular exponents and achieve the predicted convergence rates. Furthermore, they indicate the efficiency of our approach. For the Dirichlet problem on a circular or square screen, reduced to an equation for the single layer operator, the convergence rate in the energy norm is doubled when the uniform mesh is replaced by a 2-graded one. Similar results are obtained for the sound pressure, which is often the crucial quantity in applications. Even the singular exponents of the numerical solution near the edges and corners agree with those of the exact solution. The results generalize to the formulation of the Neumann problem as a hypersingular integral equation, where the predicted convergence rates and singular exponents at the edges are obtained. The main difference to the Dirichlet problem is that the numerically computed singular exponents in the corner are in qualitative, though no longer quantitative agreement. Beyond these model problems, we study the Dirichlet-to-Neumann operator on screens, as relevant for dynamic interface and contact problems. The results reflect those for the hypersingular integral equation, and the errors due to the numerical approximation of the operator are seen to be negligible.

Finally, we show the relevance of graded meshes for a real-world question from traffic noise, where graded meshes allow to accurately resolve the sound amplification around

resonance frequencies.

Graded meshes thus lead to optimal algorithms to resolve geometric singularities of the computational domain. They provide a key example for efficient approximations of the solution of transient wave equations by time-independent, adapted meshes. Such meshes also arise in adaptive algorithms based on time-integrated a posteriori error estimates [58].

## 4.2 Discretisation

For the time discretisation we consider a uniform decomposition of the time interval $[0, \infty)$ into subintervals $[t_{n-1}, t_n)$ with time step $\Delta t$, such that $t_n = n\Delta t$ $(n = 0, 1, \dots)$.

In $\mathbb{R}^3$, we assume that $\Gamma$ consists of closed triangular faces $\Gamma_i$ such that $\Gamma = \cup_i \Gamma_i$. In $\mathbb{R}^2$, $\Gamma = \cup_i \Gamma_i$ is partitioned into line segments $\Gamma_i$.

We choose a basis $\{\xi_h^1, \cdots, \xi_h^{N_s}\}$ of the space $V_h^q(\Gamma)$ of piecewise polynomial functions of degree $q$ in space. Moreover we define $\widetilde{V}_h^q(\Gamma)$ as the space $V_h^q(\Gamma)$, where the polynomials vanish on $\partial\Gamma$ for $q \geq 1$ (which is relevant for the hypersingular and Dirichlet-Neumann operators). For the time discretisation we choose a basis $\{\beta_{\Delta t}^1, \cdots, \beta_{\Delta t}^{N_t}\}$ of the space $V_t^p$ of piecewise polynomial functions of degree of $p$ in time (continuous and vanishing at $t = 0$ if $p \geq 1$).
Let $\mathcal{T}_S = \{\Delta_1, \cdots, \Delta_N\}$ be a quasi-uniform triangulation of $\Gamma$ and $\mathcal{T}_T = \{[0, t_1), [t_1, t_2), \cdots, [t_{M-1}, T)\}$ the time mesh for a finite subinterval $[0, T)$.

We consider the tensor product of the approximation spaces in space and time, $V_h^q$ and $V_{\Delta t}^p$, associated to the space-time mesh $\mathcal{T}_{S,T} = \mathcal{T}_S \times \mathcal{T}_T$, and we write

$$V_{\Delta t,h}^{p,q} := V_{\Delta t}^p \otimes V_h^q \ . \tag{4.2}$$

We analogously define

$$\tilde{V}_{\Delta t,h}^{p,q} := V_{\Delta t}^{p} \otimes \tilde{V}_{h}^{q} \ . \tag{4.3}$$

For $u_{\Delta t,h} \in V_{\Delta t,h}^{p,q}$ we thus may write

$$u_{\Delta t,h}(t,x) = \sum_{i=0}^{N_t} \sum_{j=0}^{N_s} c_j^i \beta_{\Delta t}^i(t) \xi_h^j(x) \ .$$

In the following we use the notation

- $\gamma_{\Delta t}^n(t)$ for the basis of piecewise constant functions in time,
- $\beta_{\Delta t}^n(t)$ for the basis of piecewise linear functions in time,
- $\psi_h^i(x)$ for the basis of piecewise constant functions in space,
- $\xi_h^i(x)$ for the basis of piecewise linear functions in space.

The Galerkin discretisation of the Dirichlet problem (3.6) is then given by:

Find $\psi_{\Delta t,h} \in V_{\Delta t,h}^{p,q}$ such that for all $\Psi_{\Delta t,h} \in V_{\Delta t,h}^{p,q}$

$$\int_0^\infty \int_\Gamma (V\psi_{\Delta t,h}(t,\mathbf{x})) \partial_t \Psi_{\Delta t,h}(t,\mathbf{x}) \ ds_x \ d_\sigma t = \int_0^\infty \int_\Gamma f(t,\mathbf{x}) \partial_t \Psi_{\Delta t,h}(t,\mathbf{x}) \ ds_x \ d_\sigma t \ . \tag{4.4}$$

For the Neumann problem (3.9), we have:

Find $\phi_{\Delta t,h} \in \widetilde{V}_{t,h}^{p,q}$ such that for all $\Phi_{\Delta t,h} \in \widetilde{V}_{t,h}^{p,q}$

$$\int_0^\infty \int_\Gamma (W\phi_{\Delta t,h}(t,\mathbf{x})) \partial_t \Phi_{\Delta t,h}(t,\mathbf{x}) \ ds_x \ d_\sigma t = \int_0^\infty \int_\Gamma g(t,\mathbf{x}) \partial_t \Phi_{\Delta t,h}(t,\mathbf{x}) \ ds_x \ d_\sigma t \ . \tag{4.5}$$

From the weak coercivity of $V$, respectively $W$, the discretized problems (4.4) and (4.5) admit unique solutions.

Our computations are mainly conducted on graded meshes on the square $[-1,1]^2$, respectively on the circular screen $\{(x,y,0) : \sqrt{x^2+y^2} \leq 1\}$. To define $\beta$-graded meshes

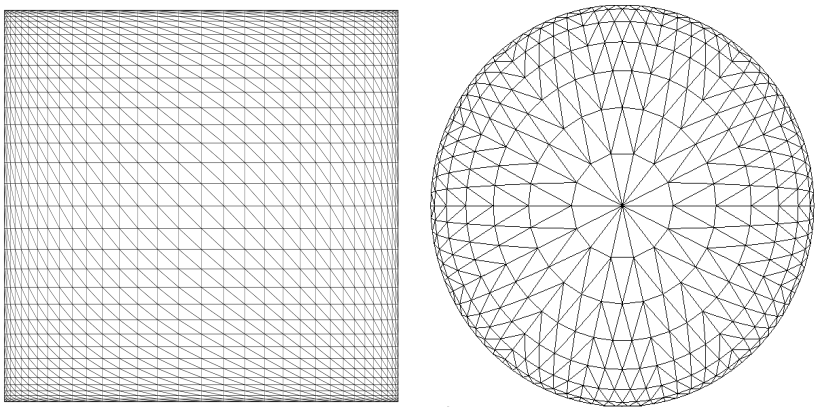

(a) (b)

Figure 4.1: $\beta$-graded meshes for (a) square and (b) circular screens, with $\beta = 2$

on the square, due to symmetry, it suffices to consider a $\beta$-graded mesh on $[-1, 0]$. We define $y_k = x_k = -1 + (\frac{k}{N_l})^\beta$ for $k = 1, \ldots, N_l$ and for a constant $\beta \geq 0$. The nodes of the $\beta$-graded mesh on the square are therefore $(x_k, y_l),\ k, l = 1, \ldots, N_l$. We note that for $\beta = 1$ we would have a uniform mesh.

In a general convex, polyhedral geometry graded meshes are locally modeled on this example. In particular, on the circular screen of radius 1, for $\beta = 1$ we take a uniform mesh with nodes on concentric circles of radius $r_k = 1 - \frac{k}{N_l}$ for $k = 0, \ldots, N_l - 1$. For the $\beta$-graded mesh, the radii are moved to $r_k = 1 - (\frac{k}{N_l})^\beta$ for $k = 0, \ldots, N_l - 1$. While the triangles become increasingly flat near the boundary, their total number remains proportional to $N_l^2$.

Examples of the resulting 2-graded meshes on the square and the circular screens are depicted in Figure 4.1.

While we use triangular meshes in our computations, for the ease of presentation we first discuss the approximation properties of graded meshes with rectangular elements. Reference [124] shows how to deduce approximation results on triangular meshes from the rectangular case.

Key ingredients in our analysis are projections from $L^2(\Gamma)$ onto $V_h^p$ on the graded mesh. We collect some key approximation properties used below:

The proofs of the following results are given in [124, Satz 3.7, Satz 3.10].

**Lemma 7.** *For $a > 0$ and $s \in [-1, -a + \frac{1}{2})$ there holds with the piecewise constant interpolant $\Pi_y^0 y^{-a}$ of $y^{-a}$ on the $\beta$-graded mesh*

$$\|y^{-a} - \Pi_y^0 y^{-a}\|_{\widetilde{H}^s([0,1])} \lesssim h^{\min\{\beta(-a-s+\frac{1}{2}),1-s\}-\varepsilon}.$$

**Lemma 8.** *For $a > 0$ and $s \in [0, a + \frac{1}{2})$ there holds with the linear interpolant $\Pi_y^1 y^a$ of $y^a$ on the $\beta$-graded mesh*

$$\|y^{a} - \Pi_y^1 y^a\|_{\widetilde{H}^s([0,1])} \lesssim h^{\min\{\beta(a-s+\frac{1}{2}),2-s\}-\varepsilon}.$$

## 4.3 Asymptotic Expansions and Numerical Approximation

### 4.3.1 Asymptotic Expansion of Solutions to the Wave Equation in a Wedge

Solutions of the Laplace and Helmholtz equations exhibit well-known singularities at non-smooth boundary points of the domain. In this section we describe a similar decomposition of the solution to the wave equation with Dirichlet or Neumann boundary conditions near an edge or a corner, into a leading part given by explicit singular functions plus less singular terms. The strategy of translating the results from the Helmholtz equation to the time-dependent wave or Lamé equations has been studied in a series of papers by Plamenevskii and coauthors [84, 86, 93, 105]. We here recall their key result for a wedge.

To be specific, for a problem in $\mathbb{R}^n$, let $0 \le d \le n-2$ and $K \subset \mathbb{R}^{n-d}$ an open cone with vertex at 0, smooth outside the vertex. We denote by $\mathcal{K} = K \times \mathbb{R}^d$ the wedge over $K$ and consider the wave equation in $\mathcal{K}$:

$$\partial_t^2 u(t,x) - \Delta u(t,x) = 0 \quad \text{in } \mathbb{R}^+ \times \mathcal{K}\ , \tag{4.6a}$$

$$Bu = g \quad \text{on } \Gamma = \partial\mathcal{K}\ , \tag{4.6b}$$

$$u(0,x) = \partial_t u(0,x) = 0 \quad \text{in } \mathcal{K}, \tag{4.6c}$$

where either inhomogeneous Dirichlet boundary conditions $Bu = u|_\Gamma$ or Neumann boundary conditions $Bu = \partial_n|_\Gamma$ are considered on $\Gamma$. We will describe the asymptotic behavior of a solution to the wave equation with Dirichlet or Neumann boundary conditions in $\mathcal{K}$ near $\{0\} \times \mathbb{R}^d$. Locally, the edge of a screen in $\mathbb{R}^3$ corresponds to $d = 1$, a cone point to $d = 0$.

The analysis uses the Fourier-Laplace transformation in time to reduce the time dependent problem to the Helmholtz equation with frequency $\omega$. Then a Fourier transform is applied changing $z \in \mathbb{R}^d$ into $\zeta \in \mathbb{R}^d$. Using polar coordinates, the conical variable $y \in K$ is transformed into the radius $r$ and the spherical variable $\theta$. A series expansion is applied, where the eigenfunctions are determined by separation of variables.

More concretely, the Fourier-Laplace transform leads to the Helmholtz equation:

$$\begin{aligned} \omega^2 \hat{u}(\omega, x) + \Delta \hat{u}(\omega, x) = 0, \ x \in \mathcal{K} \ , \\ B\hat{u} = \hat{g} \quad \text{on } \Gamma \ . \end{aligned} \tag{4.7}$$

In this case a singular decomposition of the solution is known for every complex frequency $\omega$.

Doing a separation of variables near the edge of $\mathcal{K}$, we consider the operator $\mathfrak{A}_B(\lambda) = (i\lambda)^2 + i(n-d-2)\lambda - \Delta_S$ with $B = D$ for Dirichlet and $B = N$ for Neumann boundary conditions in the subset $\Xi = K \cap S^{n-d-1}$ of the sphere. Here $\Delta_S$ denotes the Laplace operator on $S^{n-d-1}$. Denoting the eigenvalues of $\Delta_S$ in $\Xi$ by $\{\mu_{k,B}\}_{k=0}^\infty$, the eigenvalues of $\mathfrak{A}_B(\lambda)$ are given by $\lambda_{\pm k,B} = \frac{i(n-d-2)}{2} \mp i\nu_{k,B}$ with $\nu_{k,B} = \frac{((n-d-2)^2+4\mu_{k,B})^{1/2}}{2}$. The associated orthogonal eigenfunctions $\Phi_{k,B}$ of the angular variables $\theta$ are normalized as $\|\Phi_{k,B}\|^2_{L^2(\Xi)} = \nu_{k,B}^{-1}$.

For $d = 1$, $n = 3$, the nonzero eigenvalues $\lambda_{\pm k,B} = \mp\frac{k\pi}{\alpha}$ are simple if $\frac{k\pi}{\alpha} \notin \mathbb{N}$, and have multiplicity 2 otherwise. For $k > 0$ $\Phi_{k,N}(\theta) = (k\pi)^{-\frac{1}{2}} \cos(k\pi\theta/\alpha)$, $\Phi_{k,D}(\theta) = (k\pi)^{-\frac{1}{2}} \sin(k\pi\theta/\alpha)$. For Neumann boundary conditions, the eigenvalue $\lambda_{0,N} = 0$ has multiplicity 2. Here, $\alpha$ denotes the opening angle of $K \subset \mathbb{R}^2$.

We recover a screen with flat boundary as $\alpha$ tends to $2\pi^-$, and the discussion can be adapted to circular edges as in [127]. In this case $\lambda_{\pm k,B} = \mp\frac{k\pi}{\alpha}$.

The asymptotic expansion involves special solutions of the Dirichlet or Neumann prob-

lem in $K$, see [85, (3.5)], respectively [84, (4.4)]:

$$w_{-k,B}(y,\omega,\zeta) = \frac{2^{1-\nu_{k,B}}}{\Gamma(\nu_{k,B})}(i|y|\sqrt{-|\zeta|^2+\omega^2})^{\nu_{k,B}} K_{\nu_{k,B}}(i|y|\sqrt{-|\zeta|^2+\omega^2})|y|^{i\lambda_{-k,B}}\Phi_{k,B}(y/|y|) \ .$$

Here $K_\nu$ is the modified Bessel function of the third kind. These $\omega$ are the singular waves emitted from the edge.

One then transforms back into the time domain. Explicit formulas for the inverse Fourier transform $\mathcal{F}^{-1}_{(\omega,\zeta)\to(t,z)} w_{-k,B}(y,\overline{\omega},\zeta)$ can be found in Lemma 8.1 of [84].

The main theorem for the inhomogeneous wave equation involves an expansion in terms of singular functions. We refer to [84, Theorem 7.4 and Remark 7.5] for the details in the case of the Neumann problem in a wedge, respectively [85, Theorem 4.1] for the Dirichlet problem in a cone.

**Theorem 9.** *Let $\beta \leq 1$ and assume that the line $\mathrm{Im}\ \lambda = \beta - 1 + \frac{n-d-2}{2}$ does not intersect the spectrum of $\mathfrak{A}_B$. Further, define*

$$J_{\beta,B} = \left\{ j : \frac{n-d-2}{2} > \mathrm{Im}\ \lambda_{j,B} > \beta - 1 + \frac{n-d-2}{2} \right\} \ ,$$

*if $n-d>2$, and*

$$J_{\beta,B} = \{ j : 0 > \mathrm{Im}\ \lambda_{j,B} > \beta - 1 \} \cup A \ ,$$

*with $A = \{0\}$ for $\beta \leq 0$ and $A = \emptyset$ otherwise.*
*If $u$ is a strong solution to the inhomogeneous wave equation with right hand side $f$ and homogeneous Dirichlet or Neumann boundary conditions ($B = D$, resp. $N$) in $\mathcal{K}$ near $\{0\}\times\mathbb{R}^d$, then $u$ is of the form*

$$\sum_{j\in J_{\beta,B}} \Gamma(1+\nu_{j,B})|y|^{i\lambda_{j,B}}\Phi_{j,B}(\theta) \sum_{m=0}^{N_j} \frac{(\partial_t^2 - \Delta_z)^m (i|y|)^{2m}}{2^{2m} m! \Gamma(m+\nu_{j,B}+1)} \mathcal{F}^{-1}_{(\omega,\zeta)\to(t,z)} c_{j,B} + \check{v}(y,t,z) \ ,$$

*assuming that $i\lambda_{j,B} \notin \mathbb{N}$. Here $N_j$ is sufficiently large, and*

$$c_{j,B}(\omega,\zeta) = \langle \hat{f}(\cdot,\omega,\zeta), w_{-j,B}(\cdot,\overline{\omega},\zeta)\rangle_{L^2(K)};$$

*its regularity is determined by the right hand side. The remainder $\check{v}$ is less singular, in*

*the sense that* $\|\check{v}\|_{DV_{\beta,q}(K\times\mathbb{R};\gamma)} \lesssim \|f\|_{RH_{\beta,q}(K\times\mathbb{R},\gamma)}$, $\gamma > 0$, $q \in \mathbb{N}_0$. *We refer to [84] for the definition of the weighted spaces* $DV_\beta(K\times\mathbb{R},\gamma), RH_{\beta,q}(K\times\mathbb{R},\gamma)$, $\gamma > 0$, $q \in \mathbb{N}_0$.
*If* $i\lambda_{j,B} \in \mathbb{N}$ *additional terms* $|y|^{i\lambda_{j,B}}\log(|y|)$ *appear.*

Further information can be obtained from the singular functions $W_{-j,B}(y,t,z) = \mathcal{F}^{-1}_{(\zeta,\omega)\to(t,z)} w_{-j,B}$, using the convolution representation

$$\mathcal{F}^{-1}_{(\omega,\zeta)\to(t,z)} c_{j,B} = \int_{\mathbb{R}^d} dz_1 \int_{\mathbb{R}} dt_1 \int_K dy f(y,z_1,t_1) W_{-j,B}(y,t-t_1,z-z_1)$$

of the asymptotic expansion in Theorem 9. Because the singular support of $W_{-j,B}$ lies on the lightcone $\{(y,t,z) \in \mathbb{R}^{n+1} : t = \sqrt{|y|^2+|z|^2}\}$ emanating from the edge, we note that $\mathcal{F}^{-1}_{(\omega,\zeta)\to(t,z)} c_{j,B}$ is smooth in

$$\{(t,z) \in \mathbb{R}^{d+1} : t > \sup\{t_1 + \sqrt{|y|^2+|z-z_1|^2} : (y,z_1,t_1) \in \text{singsupp } f\}\} .$$

In particular, if $f$ is smooth, singsupp $f = \emptyset$ and $\mathcal{F}^{-1}_{(\omega,\zeta)\to(t,z)} c_{j,B}$ is smooth everywhere.

Theorem 9 can be translated into a result for inhomogeneous boundary conditions, as for elliptic problems [126, Section 5]. If $Bu = g$ on $\mathbb{R}^+_t \times \partial\mathcal{K}$, choose a function $\widetilde{g}$ in $\mathbb{R}^+_t \times \mathcal{K}$ such that $B\widetilde{g} = g$ on $\mathbb{R}^+_t \times \partial\mathcal{K}$. The function $U = u - \widetilde{g}$ satisfies homogeneous boundary conditions $BU = 0$, and $\partial_t^2 U - \Delta U = f - \partial_t^2\widetilde{g} + \Delta\widetilde{g}$. According to Theorem 9, $U$ admits an asymptotic expansion, and therefore so does $u = U + \widetilde{g}$.

For the analysis of the solutions to the boundary integral formulations of the wave equation, the resulting asymptotic expansions of the boundary values $u|_\Gamma$ and $\partial_n u|_\Gamma$ will be crucial. They are directly obtained from the expansion in the interior. In particular, for $i\lambda_{j,B} \notin \mathbb{N}$ the singularities of $u|_\Gamma$ are proportional to $|y|^{i\lambda_{j,B}+2m}$, and the singularities of $\partial_n u|_\Gamma$ are proportional to $|y|^{i\lambda_{j,B}+2m-1}$. When $i\lambda_{j,B} \in \mathbb{N}$, additional terms $|y|^{i\lambda_{j,B}+2m}\log(|y|)$, respectively $|y|^{i\lambda_{j,B}+2m-1}\log(|y|)$ appear.

### 4.3.2 Singularities for Circular Screens and Approximation

We first illustrate the above results for the exterior of a circular wedge with exterior opening angle $\alpha$. For $\alpha \to 2\pi^-$, the wedge degenerates into the circular screen $\{(x_1,x_2,0) \in \mathbb{R}^3 : x_1^2 + x_2^2 \le 1\}$. Near the edge $\{(x_1,x_2,0) \in \mathbb{R}^3 : x_1^2 + x_2^2 = 1\}$ we use the coordinates

$(y, z, \theta)$, where in polar coordinates in the $x_1 - x_2$-plane $y = r - 1$, $z = \theta$. Using [127], an analogous expansion to Theorem 9 also holds in this curved geometry, with the same leading singular term $|y|^{i\lambda}$, where $\lambda \to -\frac{i}{2}$ as $\alpha \to 2\pi^-$:

$$u(y,t,z)|_\Gamma = a(t,z)|y|^{1/2} + \check{v}(y,t,z) \ , \tag{4.8}$$

$$\partial_n u(y,t,z)|_\Gamma = b(t,z)|y|^{-\frac{1}{2}} + \tilde{v}(y,z,t) \ . \tag{4.9}$$

Here $a$ and $b$ are smooth for smooth data.

From these decompositions we obtain optimal approximation properties on the graded mesh. Here we show how the analysis performed by T. von Petersdorff in [124] may be extended to the hyperbolic case. The results are derived for the h-version on graded meshes and contain automatically the case of a quasi-uniform mesh by setting the grading parameter $\beta = 1$.

**Theorem 10.** *Let $\varepsilon > 0$. a) Let $u$ be a strong solution to the homogeneous wave equation with inhomogeneous Neumann boundary conditions $\partial_n u|_\Gamma = g$, with $g$ smooth. Further, let $\phi^\beta_{h,\Delta t}$ be the best approximation in the norm of $H^r_\sigma(\mathbb{R}^+, \widetilde{H}^{\frac{1}{2}-s}(\Gamma))$ to the Dirichlet trace $u|_\Gamma$ in $\widetilde{V}^{p,1}_{\Delta t,h}$ on a $\beta$-graded spatial mesh with $\Delta t \lesssim h^\beta$. Then $\|u - \phi^\beta_{h,\Delta t}\|_{r,\frac{1}{2}-s,\Gamma,*} \leq C_{\beta,\varepsilon} h^{\min\{\beta(\frac{1}{2}+s),\frac{3}{2}+s\}-\varepsilon}$, where $s \in [0, \frac{1}{2}]$ and $r \in [0, p)$.*

*b) Let $u$ be a strong solution to the homogeneous wave equation with inhomogeneous Dirichlet boundary conditions $u|_\Gamma = g$, with $g$ smooth. Further, let $\psi^\beta_{h,\Delta t}$ be the best approximation in the norm of $H^r_\sigma(\mathbb{R}^+, \widetilde{H}^{-\frac{1}{2}}(\Gamma))$ to the Neumann trace $\partial_n u|_\Gamma$ in $V^{p,0}_{\Delta t,h}$ on a $\beta$-graded spatial mesh with $\Delta t \lesssim h^\beta$. Then $\|\partial_n u - \psi^\beta_{h,\Delta t}\|_{r,-\frac{1}{2},\Gamma,*} \leq C_{\beta,\varepsilon} h^{\min\{\frac{\beta}{2},\frac{3}{2}\}-\varepsilon}$, where $r \in [0, p+1)$.*

Theorem 10 implies a corresponding result for the solutions of the single layer and hypersingular integral equations on the screen:

**Corollary 11.** *Let $\varepsilon > 0$. a) Let $\phi$ be the solution to the hypersingular integral equation (3.8) and $\phi^\beta_{h,\Delta t}$ the best approximation in the norm of $H^r_\sigma(\mathbb{R}^+, \widetilde{H}^{\frac{1}{2}-s}(\Gamma))$ to $\phi$ in $\widetilde{V}^{p,1}_{\Delta t,h}$ on a $\beta$-graded spatial mesh with $\Delta t \lesssim h^\beta$. Then $\|\phi - \phi^\beta_{h,\Delta t}\|_{r,\frac{1}{2}-s,\Gamma,*} \leq C_{\beta,\varepsilon} h^{\min\{\beta(\frac{1}{2}+s),\frac{3}{2}+s\}-\varepsilon}$, where $s \in [0, \frac{1}{2}]$ and $r \in [0, p)$.*

*b) Let $\psi$ be the solution to the single layer integral equation* (3.2) *and $\psi^{\beta}_{h,\Delta t}$ the best approximation in the norm of $H^r_\sigma(\mathbb{R}^+, \widetilde{H}^{-\frac{1}{2}}(\Gamma))$ to $\psi$ in $V^{p,0}_{\Delta t,h}$ on a $\beta$-graded spatial mesh with $\Delta t \lesssim h^\beta$. Then $\|\psi - \psi^{\beta}_{h,\Delta t}\|_{r,-\frac{1}{2},\Gamma,*} \leq C_{\beta,\varepsilon} h^{\min\{\frac{\beta}{2},\frac{3}{2}\}-\varepsilon}$, where $r \in [0, p+1)$.*

Indeed, on the flat screen the solutions to the integral equations are given by $\phi = [u]\,|_\Gamma$ in terms of the solution $u$ which satisfies Neumann conditions $Bu = \partial_n u|_\Gamma = g$, respectively $\psi = [\partial_n u]\,|_\Gamma$ in terms of the solution $u$ which satisfies Dirichlet conditions $Bu = u|_\Gamma = f$.

The proof of Theorem 10 relies on the auxiliary results in Section 4.2. We first consider the approximation of the Neumann trace.

**Theorem 12.** *Under the assumptions of Theorem 10, there holds* $\|\partial_n u - \Pi^0_x \Pi^p_t \partial_n u\|_{r,-\frac{1}{2},\Gamma,*} \lesssim h^{\min\{\beta/2,\frac{3}{2}\}-\varepsilon}$.

**Theorem 13.** *For $r \in [0, p)$ and $s \in [0, \frac{1}{2}]$ there holds* $\|u - \Pi^1_x \Pi^p_t u\|_{r,\frac{1}{2}-s,\Gamma,*} \lesssim h^{\min\{\beta(\frac{1}{2}+s),\frac{3}{2}+s\}-\varepsilon}$.

As before, our results extend from rectangular to triangular elements as in reference [124].

### 4.3.3 Singularities for Polygonal Screens and Approximation

We consider the singular expansion of the solution to the wave equation (4.6) with Dirichlet or Neumann boundary conditions on a polygonal screen $\Gamma$. Additional singularities now arise from the corners of the screen. For simplicity, we restrict ourselves to the model case of a square screen $\Gamma = (0,1) \times (0,1) \times \{0\} \in \mathbb{R}^3$. In this geometry, for elliptic problems asymptotic expansions and their implications for the numerical approximation are discussed in [90, 125].

The following result gives a decomposition of the solution to the Helmholtz equation and its normal derivative on $\Gamma$ near the vertex $(0,0)$, in terms of polar coordinates $(r, \theta)$ centered at this point. Note that we have two boundary values, $\hat{u}_\pm$, from the upper and lower sides of the screen.

**Theorem 14.** *For fixed $\omega \neq 0$ with $\mathrm{Im}\ \omega \geq 0$, let $\hat{u}_\omega$ be the solution to the Helmholtz equation*

$$\begin{aligned} \omega^2 \hat{u}(\omega, x) - \Delta \hat{u}(\omega, x) = 0,\ x \in \mathbb{R}^n \setminus \Gamma\ , \\ B\hat{u}(\omega, x) = \hat{g}(\omega, x),\ x \in \Gamma\ , \end{aligned} \tag{4.10}$$

*where $\hat{g}$ is sufficiently smooth. a) Assume $Bu = \partial_n u|_\Gamma$. If $\hat{g} \in H^1(\Gamma)$, then in polar coordinates (r,θ)*

$$\begin{aligned} \hat{u}(\omega, x)|_+ = \chi(r) r^\gamma \alpha_\omega(\theta) + \tilde{\chi}(\theta) b_{1,\omega}(r) (\sin(\theta))^{\frac{1}{2}} \\ + \tilde{\chi}(\frac{\pi}{2} - \theta) b_{2,\omega}(r) (\cos(\theta))^{\frac{1}{2}} + \hat{u}_{0,\omega}(r, \theta)\ , \end{aligned} \tag{4.11}$$

*where for all $\epsilon > 0$ we have $\hat{u}_{0,\omega} \in \widetilde{H}^{2-\epsilon}(\Gamma)$, $\alpha_\omega \in H^{2-\epsilon}[0, \frac{\pi}{2}]$, $b_{i,\omega} = c_{i,\omega,1} r^{\gamma - \frac{1}{2}} + c_{i,\omega,2} r^{\lambda - \frac{1}{2}} + d_{i,\omega}(r)$, $d_{i,\omega}(r) \in H^{\frac{3}{2}-\varepsilon}(\mathbb{R}^+)$ with $r^{\frac{3}{2}-\varepsilon} d_{i,\omega}(r) \in L^2(\mathbb{R}^+)$, $c_{i,\omega,j} \in \mathbb{R}$. Here $\chi, \tilde{\chi} \in C_c^\infty$ are cut-off functions, $\chi, \tilde{\chi} = 1$ in a neighborhood of $0$.*
*b) Assume $Bu = u|_\Gamma$. If $\hat{g} \in H^2(\Gamma)$, then*

$$\begin{aligned} \partial_n u \hat{u}(\omega, x)|_+ = \chi(r) r^{\gamma - 1} \alpha_\omega(\theta) + \tilde{\chi}(\theta) b_{1,\omega}(r) r^{-1} (\sin(\theta))^{-\frac{1}{2}} \\ + \tilde{\chi}(\frac{\pi}{2} - \theta) b_{2,\omega}(r) r^{-1} (\cos(\theta))^{-\frac{1}{2}} + \hat{\psi}_{0,\omega}(r, \theta)\ , \end{aligned}$$

*where for all $\epsilon > 0$ we have $\hat{\psi}_{0,\omega} \in H^{1-\epsilon}(\Gamma)$, $\alpha_\omega \in H^{1-\epsilon}[0, \frac{\pi}{2}]$, $b_{i,\omega} = c_{i,\omega} r^\gamma + d_{i,\omega}(r)$, $r^{-\frac{1}{2}} d_{i,\omega}(r) \in H^1(\mathbb{R}^+)$, $r^{-\frac{3}{2}} d_{i,\omega}(r) \in L_2(\mathbb{R}^+)$, $c_{i,\omega} \in \mathbb{R}$. Here $\chi$, $\tilde{\chi} \in C_c^\infty$ are cut-off functions, $\chi, \tilde{\chi} = 1$ in a neighborhood of $0$.*

In fact, if $\hat{g}$ is a Schwartz function of $\omega$, the decomposition depends smoothly on this variable. For the square screen $\gamma \approx 0.2966$ and $\lambda \approx 1.426$ are determined by the lowest eigenvalues of the operator $\mathfrak{A}_B$ on $S^2 \setminus (\mathbb{R}^2_+ \times \{0\})$. For the proof of Theorem 14, see [80], p. 108-109.

As above, in analogy with the work of Plamenevskii and coauthors, the asymptotic

expansion translates into the time domain:

$$u(t,x)|_+ = v_0(t,r,\theta) + \chi(r) r^{\gamma} \alpha(t,\theta) + \tilde{\chi}(\theta) b_1(t,r) (\sin(\theta))^{\frac{1}{2}} + \tilde{\chi}(\tfrac{\pi}{2} - \theta) b_2(t,r) (\cos(\theta))^{\frac{1}{2}} \ , \tag{4.12}$$

$$\partial_n u(t,x)|_+ = \psi_0(t,r,\theta) + \chi(r) r^{\gamma-1} \alpha(t,\theta) + \tilde{\chi}(\theta) b_1(t,r) r^{-1} (\sin(\theta))^{-\frac{1}{2}} + \tilde{\chi}(\tfrac{\pi}{2} - \theta) b_2(t,r) r^{-1} (\cos(\theta))^{-\frac{1}{2}} \ . \tag{4.13}$$

To control the remainder terms in these formal computations requires elliptic a priori weighted estimates near the singularities, as discussed in [93].

From the decomposition, similar to Theorem 10 we obtain optimal approximation properties on the graded mesh, where the error is dominated by the edge singularities, not the corners. The beta needs to be chosen large enough, depending on the singular exponent $\gamma$ in (4.12), (4.13). See [124, 125] for similar results in the time-independent case.

**Theorem 15.** *Let $\varepsilon > 0$. a) Let $u$ be a strong solution to the homogeneous wave equation with inhomogeneous Neumann boundary conditions $\partial_n u|_\Gamma = g$, with $g$ smooth. Further, let $\phi^\beta_{h,\Delta t}$ be the best approximation in the norm of $H^r_\sigma(\mathbb{R}^+, \widetilde{H}^{\frac{1}{2}-s}(\Gamma))$ to the Dirichlet trace $u|_\Gamma$ in $\widetilde{V}^{p,1}_{\Delta t,h}$ on a $\beta$-graded spatial mesh with $\Delta t \lesssim h^\beta$ and $\beta \geq \frac{3}{2(\gamma+\frac{1}{2})}$. Then $\|u - \phi^\beta_{h,\Delta t}\|_{r,\frac{1}{2}-s,\Gamma,*} \leq C_{\beta,\varepsilon} h^{\min\{\frac{\beta}{2},\frac{3}{2}\}+s-\varepsilon}$, where $s \in [0,\frac{1}{2}]$ and $r \in [0,p)$.*

*b) Let $u$ be a strong solution to the homogeneous wave equation with inhomogeneous Dirichlet boundary conditions $u|_\Gamma = g$, with $g$ smooth. Further, let $\psi^\beta_{h,\Delta t}$ be the best approximation in the norm of $H^r_\sigma(\mathbb{R}^+, \widetilde{H}^{-\frac{1}{2}}(\Gamma))$ to the Neumann trace $\partial_n u|_\Gamma$ in $V^{p,0}_{\Delta t,h}$ on a $\beta$-graded spatial mesh with $\Delta t \lesssim h^\beta$ and $\beta \geq \frac{3}{2(\gamma+\frac{1}{2})}$. Then $\|\partial_n u - \psi^\beta_{h,\Delta t}\|_{r,-\frac{1}{2},\Gamma,*} \leq C_{\beta,\varepsilon} h^{\min\{\frac{\beta}{2},\frac{3}{2}\}-\varepsilon}$, where $r \in [0,p+1)$.*

The theorem again implies a corresponding result for the solutions of the single layer and hypersingular integral equations on the screen:

**Corollary 16.** *Let $\varepsilon > 0$. a) Let $\phi$ be the solution to the hypersingular integral equation (3.8) and $\phi^\beta_{h,\Delta t}$ the best approximation in the norm of $H^r_\sigma(\mathbb{R}^+, \widetilde{H}^{\frac{1}{2}-s}(\Gamma))$ to $\phi$ in $\widetilde{V}^{p,1}_{\Delta t,h}$ on a $\beta$-graded spatial mesh with $\Delta t \lesssim h^\beta$ and and $\beta \geq \frac{3}{2(\gamma+\frac{1}{2})}$. Then $\|\phi - \phi^\beta_{h,\Delta t}\|_{r,\frac{1}{2}-s,\Gamma,*} \leq C_{\beta,\varepsilon} h^{\min\{\beta(\frac{1}{2}+s),\frac{3}{2}+s\}-\varepsilon}$, where $s \in [0,\frac{1}{2}]$ and $r \in [0,p)$.*

*b) Let $\psi$ be the solution to the single layer integral equation (3.2) and $\psi^{\beta}_{h,\Delta t}$ the best approximation in the norm of $H^r_\sigma(\mathbb{R}^+, \widetilde{H}^{-\frac{1}{2}}(\Gamma))$ to $\psi$ in $V^{p,0}_{\Delta t,h}$ on a $\beta$-graded spatial mesh with $\Delta t \lesssim h^\beta$ and and $\beta \geq \frac{3}{2(\gamma+\frac{1}{2})}$. Then $\|\psi - \psi^{\beta}_{h,\Delta t}\|_{r,-\frac{1}{2},\Gamma,*} \leq C_{\beta,\varepsilon} h^{\min\{\frac{\beta}{2},\frac{3}{2}\}-\varepsilon}$, where $r \in [0, p+1)$.*

The proof of Theorem 15 and Corollary 16 relies on arguments by von Petersdorff [124]. We refer to this reference for a detailed analysis in the time-independent case.

## 4.4 Algorithmic Considerations

On the left hand side of (4.4), we use ansatz functions

$$\psi_{\Delta t,h}(t,x) = \sum_{m,i} c_i^m \gamma^m_{\Delta t}(t)\psi^i_h(x) \in V^{0,0}_{h,\Delta t}$$

and test functions $\Psi^{n,l}(t,x) = \gamma_{\Delta t}(t)\psi^l_h(x) \in V^{0,0}_{h,\Delta t}$ to obtain for the single layer potential:

$$\begin{aligned}
\int_0^\infty \langle V\psi_{\Delta t,h}, \dot\gamma^n_{\Delta t}\psi^l_h\rangle dt &= \sum_{m,i} c_i^m \frac{1}{4\pi}\int_0^\infty \int_{\Gamma\times\Gamma} \frac{1}{|x-y|}\gamma^m_{\Delta t}(t-|x-y|)\psi^i_h(y)\dot\gamma^n_{\Delta t}(t)\psi^l_h(x) ds_x ds_y dt \\
&= \sum_{m,i} c_i^m \frac{1}{4\pi}\int_{\Gamma\times\Gamma} \frac{\psi^i_h(y)\psi^l_h(x)}{|x-y|}\int_0^\infty \gamma^m_{\Delta t}(t-|x-y|)\dot\gamma^n_{\Delta t}(t)dt\ ds_x ds_y \\
&= \sum_{m,i} c_i^m \frac{1}{4\pi}\int_{\Gamma\times\Gamma} \frac{\psi^i_h(y)\psi^l_h(x)}{|x-y|}\left(\chi_{E_{n-m-1}}(x,y) - \chi_{E_{n-m}}(x,y)\right) ds_x ds_y \\
&= \sum_{m,i} c_i^m \frac{1}{4\pi}\Big[\int_{E_{n-m-1}} \frac{\psi^i_h(y)\psi^l_h(x)}{|x-y|}\ ds_x ds_y - \int_{E_{n-m}} \frac{\psi^i_h(y)\psi^l_h(x)}{|x-y|}\ ds_x ds_y\Big]
\end{aligned}$$

for all $n = 1, ..., N_t$ and $l = 1, ..., N_s$. Here the light cone $E_l$ is defined as

$$E_l := \{(x,y) \in \Gamma\times\Gamma :\ t_l \leq |x-y| \leq t_{l+1}\}\ ,$$

and its indicator function is defined as $\chi_{E_l}(x,y) = 1$ if $(x,y) \in E_l$, and $\chi_{E_l}(x,y) = 0$ otherwise. The integrals are evaluated using a composite *hp*-graded quadrature [54].

For piecewise constant test functions in time, the Galerkin discretisation leads to a block–lower–triangular system of equations, which can be solved by blockwise forward

substitution. For the Dirichlet problem (4.4) we obtain an algebraic system of the form

$$\sum_{m=1}^{n} V^{n-m} c^m = f^{n-1} - f^n \ ,$$

where $c^m$ is the vector with components $c_i^m$ of the the ansatz function $\psi_{\Delta t,h}(t,x)$ and $f^n = \int_\Gamma f(t_n,x)\, ds_x$. Forward substitution gives rise to the *marching-in-on-time* (MOT) scheme

$$V^0 c^n = f^{n-1} - f^n - \sum_{m=1}^{n-1} V^{n-m} c^m \,. \tag{4.14}$$

The resulting algorithm is given as Algorithm 1.

**Algorithm 1** Marching-on-in-time algorithm.

**for** $n = 1, 2, \ldots$ **do**
  **if** $n - 1 > \left[\frac{\operatorname{diam}\Gamma}{\Delta t}\right]$ **then**
    $V^{n-1} = 0$
  **else**
    Compute and store

$$(V^{n-1})_{il} = \frac{1}{4\pi} \int_{E_{n-1}} \frac{\psi_h^i(y)\psi_h^l(x)}{|x-y|}\, ds_x ds_y, \quad i,l = 1,\ldots,N_s$$

  **end if**
  Compute right hand side $f^{n-1} - f^n - \sum_{m=1}^{n-1} V^{n-m} c^m$
  Solve system of linear equations (4.14)
  Store solution $\psi^n$
**end for**

We remark that for a bounded surface $\Gamma$ the matrices $V^{n-m}$ vanish whenever the time difference $l = n-m$ satisfies $l > \left[\frac{\operatorname{diam}\Gamma}{\Delta t}\right]$, i.e. the light cone has passed the entire surface $\Gamma$.

The implementation of $W$ is based on the weak form (4.5) and the formula

$$\begin{aligned}\int_{\mathbb{R}^+\times\Gamma} (W\phi)\ \partial_t\Phi\ dt\, ds_x \ &= \frac{1}{2\pi} \int_0^\infty \int_{\Gamma\times\Gamma} \Big\{ \frac{-n_x \cdot n_y}{|x-y|} \dot\phi(\tau,y) \ddot\Phi(t,x) \\ &\qquad + \frac{(\nabla_\Gamma \phi)(\tau,y) \cdot (\nabla_\Gamma \dot\Phi)(t,x)}{|x-y|} \Big\} ds_y\ ds_x\ dt \ ,\end{aligned}$$

see [22] for details. We use ansatz functions in $\widetilde{V}_{h,\Delta t}^{1,1}$. To obtain an MOT scheme the test functions $\dot\Phi_{h,\Delta t}(t,x) \in \widetilde{V}_{h,\Delta t}^{0,1}$ are piecewise constant in time and piecewise linear in space.

Similar formulas hold for the operators $K, K'$, and variants of the discretisations for $V$, $W$. The resulting MOT schemes are described in [22]. They can be combined into a stable scheme for the Dirichlet-to-Neumann operator $\mathcal{S}$ from (3.13), with $\sigma = 0$, using the representation $\mathcal{S} = W - (K' - \frac{1}{2}I)V^{-1}(K - \frac{1}{2}I)$ in terms of layer potentials. As in [113], the Dirichlet-to-Neumann equation (3.14), $\mathcal{S}u = h$, is equivalently reformulated as follows:

For given $h \in H^{\frac{3}{2}}_{\sigma}(\mathbb{R}^+, H^{-\frac{1}{2}}(\Gamma))$, find $\phi \in H^{\frac{1}{2}}_{\sigma}(\mathbb{R}^+, \tilde{H}^{\frac{1}{2}}(\Gamma)), \psi \in H^{\frac{1}{2}}_{\sigma}(\mathbb{R}^+, \tilde{H}^{-\frac{1}{2}}(\Gamma))$ such that

$$\int_0^\infty \langle W\phi - (K' - \tfrac{1}{2})\psi, \Phi\rangle_\Gamma \,\mathrm{dt} = \int_0^\infty \langle h, \Phi\rangle_\Gamma \,\mathrm{dt}\ , \tag{4.15}$$

$$\int_0^\infty [\langle V\psi, \partial_t\Psi\rangle_\Gamma - \langle (K - \tfrac{1}{2})\phi, \partial_t\Psi\rangle_\Gamma] \,\mathrm{dt} = 0, \tag{4.16}$$

holds for all $\Phi \in H^{\frac{1}{2}}_{\sigma}(\mathbb{R}^+, \tilde{H}^{\frac{1}{2}}(\Gamma))$,$\Psi \in H^{\frac{1}{2}}_{\sigma}(\mathbb{R}^+, \tilde{H}^{-\frac{1}{2}}(\Gamma))$.

For the discretisation, we look for $\phi_{\Delta t,h} \in \tilde{V}^{1,1}_{\Delta t,h}$, $\psi_{\Delta t,h} \in V^{1,1}_{\Delta t,h}$ linear in space and time. To obtain a marching-on-in-time scheme we test the first equation against constant test functions in time and the second equation against the time derivative of constant test functions.

## 4.5 Numerical Experiments

### 4.5.1 Single Layer Potential

**Example 1.** *Using the discretisation from Section 4.2, we compute the solution to the integral equation $V\psi = f$ on $\mathbb{R}^+_t \times \Gamma$ with the circular screen $\Gamma = \{(x, y, 0) : 0 \leq \sqrt{x^2 + y^2} \leq 1\}$ depicted in Figure 4.1. We use the weak form (4.4) with constant test and ansatz functions in space and time. The right hand side is given by $f(t, x) = \cos(|k|t - k \cdot x)\exp(-1/(10t^2))$, where $k = (0.2, 0.2, 0.2)$. The time discretisation errors are negligibly small in this numerical experiment, when the time step is chosen to be $\Delta t = 0.005$. We compute the solution up to $T = 1$. The finest graded mesh consists of 2662 triangles, and we use the solution on this mesh as reference solution using the same*

$\Delta t = 0.005$.

Figure 4.2 shows the density along a cross-section on a $\beta$-graded mesh with $\beta$=2 and 2662 triangles at time $T = 0.5$. The figure exhibits the edge singularities predicted by the decomposition in equation (4.9) and illustrates the qualitative behavior of the solution.

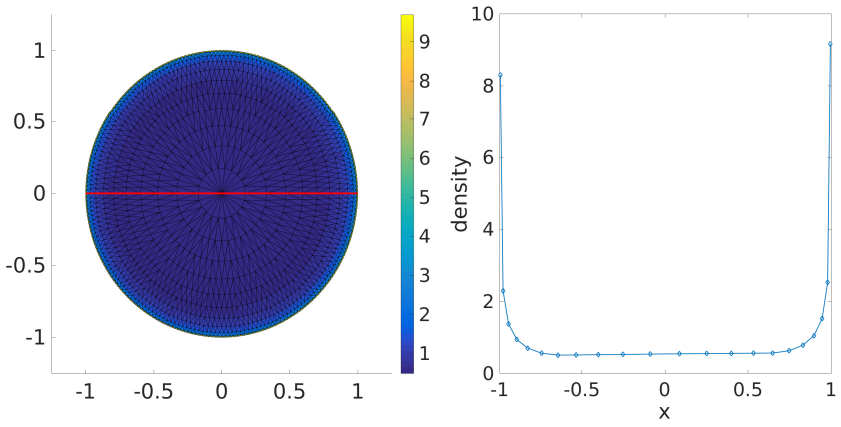


Figure 4.2: Solution of the single layer equation at $T = 0.5$ along $y = 0$ on the circular screen, Example 1

Figure 4.3 examines the detailed singular behavior near the outer edge at $(1, 0)$. It plots the numerical density at times $T = 0.5,\ 0.75,\ 1.0$ against the distance to the edge along $x$-axis. In the log-log plot the slope of the curve near 0 corresponds to the edge exponent in decomposition (4.9).

The numerical solution exhibits edge singularities in close agreement with (4.9). Numerically, the singular exponents are within 8% of the theoretical value of $-\frac{1}{2}$ for the edge at these times. Note that the convergence of our boundary element method in the energy norm does not a priori imply convergence for the numerically computed singular exponents.

For Example 1, we finally consider the error compared to the benchmark solution on the 2-graded mesh. Because of the low spatial regularity of the solution, the numerical solutions cannot be expected to converge in $L^2([0, T] \times \Gamma)$. As a weaker measure, we consider the energy, which is computed from the stiffness matrix $V$ and the solution vector $c$ as $E(\psi) = \frac{1}{2}c^\top Vc - c^\top f$. It is comparable or weaker than the norm of $H^0_\sigma(\mathbb{R}^+, H^{-\frac{1}{2}}(\Gamma))$.

For the error as a function of the degrees of freedom, Figure 4.4 shows convergence in the energy norm with a rate $-0.52$ on the 2-graded mesh, respectively $-0.26$ on the uniform mesh. The error therefore behaves in agreement with the approximation properties proportional to $\sim h$ (equivalently, $\sim DOF^{-\frac{1}{2}}$) on the 2-graded mesh, while the convergence is $\sim h^{1/2}$ ($\sim DOF^{-1/4}$) on a uniform mesh.

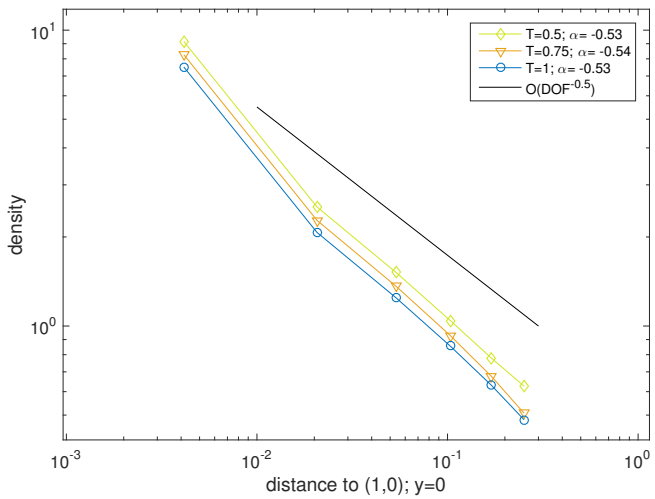


Figure 4.3: Asymptotic behavior of the solution to the single layer equation near edge along $y = 0$, Example 1

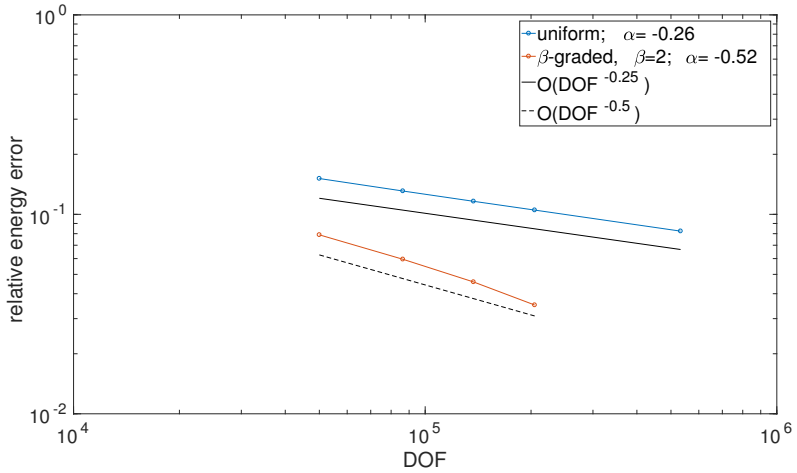


Figure 4.4: Energy error for single layer equation on circular screen, Example 1

The slope $\alpha$ is computed from the linear part of the plot - using points 2 to 4.

**Example 2.** *Using the discretisation from Section 4.2, we compute the solution to the integral equation* $V\psi = f$ *on* $\mathbb{R}^+_t \times \Gamma$ *with the square screen* $\Gamma = [-1,1]^2 \times \{0\}$ *using the weak form* (4.4)*, with constant test and ansatz functions in space and time. The right hand side is given by* $f(t,x) = \cos(|k|t - k \cdot x)\exp(-1/(10t^2))$*, where* $k = (0.2, 0.2, 0.2)$*. The time discretisation errors are negligibly small in this numerical experiment, when the time step is chosen to be* $\Delta t = 0.005$*. We compute the solution up to* $T = 1$*. The finest graded mesh consists of* 2312 *triangles, and we use the solution on this mesh as reference solution using the same* $\Delta t = 0.005$*.*

Figures 4.5 and 4.6 show the density along a cross-section and along a longitudinal section on a $\beta$-graded mesh with $\beta$=2 and 2312 triangles at time $T = 0.5$. Both figures exhibit the corner and edge singularities predicted by the decomposition (4.13) and illustrate the qualitative behavior of the solution. Figure 4.7 compares the solution along the cross-section on a 2-graded mesh against the solution on two uniform meshes. We see that the 2-graded mesh yields a higher resolution of the corner singularities compared to the uniform meshes. The asymmetry on the cross-section plots come from the plane wave RHS, which is not symmetric.

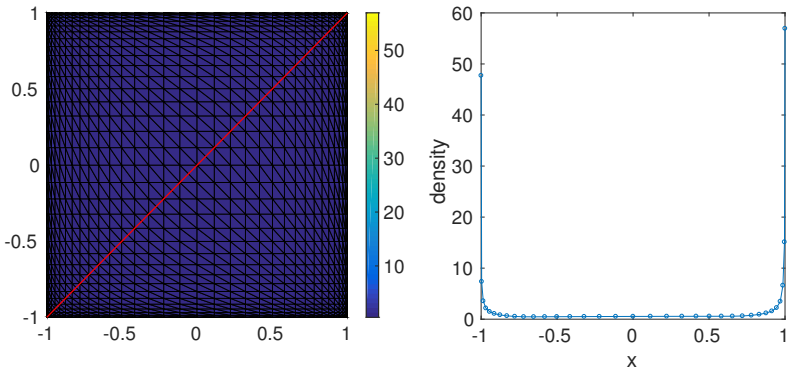


Figure 4.5: Solution of the single layer equation at $T = 0.5$ along $y = x$ on the square screen, Example 2

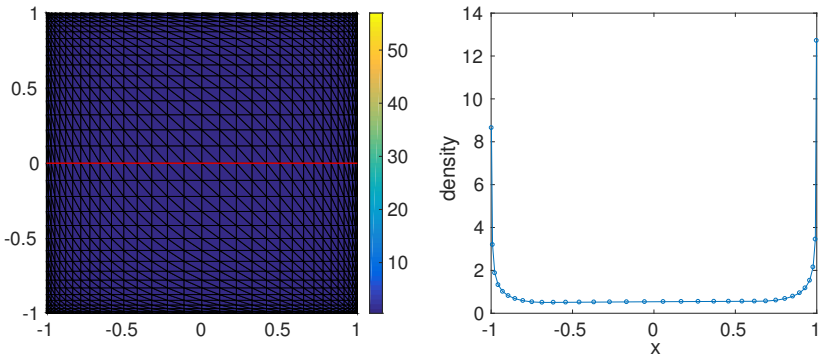


Figure 4.6: Solution of the single layer equation at $T = 0.5$ along $y = 0$ on the square screen, Example 2

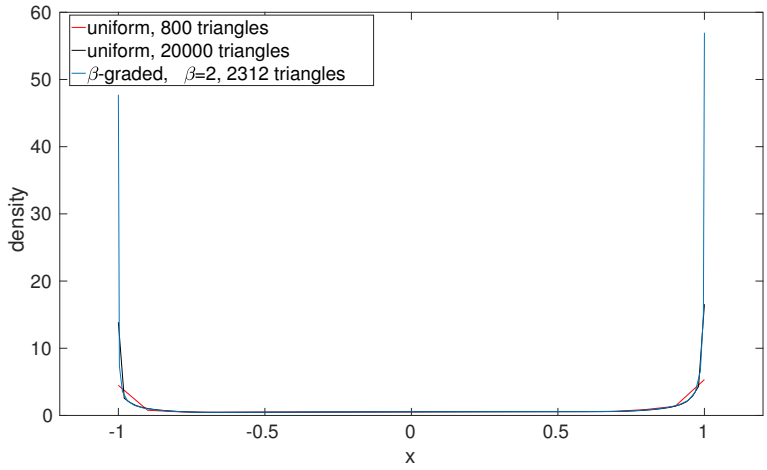


Figure 4.7: Numerical computation of the corner singularity along diagonal from $(-1, -1)$ to $(1, 1)$ at time $T = 0.5$, Example 2

Figure 4.8 examines the detailed singular behavior near the corner $(1, 1)$. It plots the numerical density at times $T = 0.5,\ 0.75,\ 1.0$ against the distance to the corner along the diagonal of the screen. In the log-log plot the slope of the curve near 0 corresponds to the corner exponent in decomposition (4.13). Similarly, Figure 4.9 shows the density as a function of $x$ for $y = 0$, perpendicular to the edge, at the same times.

After a short computational time, the numerical solution exhibits edge and corner singularities corresponding to (4.13). Numerically, the singular exponents at large enough times $T = 0.5,\ 0.75,\ 1$ are within 2% of the theoretical value of $-\frac{1}{2}$ for the edge, while they

are around $-0.78$ for the corner, approximately 10% higher than the theoretical exponent $\gamma - 1$. Note that the convergence of our boundary element method in the energy norm does not a priori imply convergence for the numerically computed singular exponents.

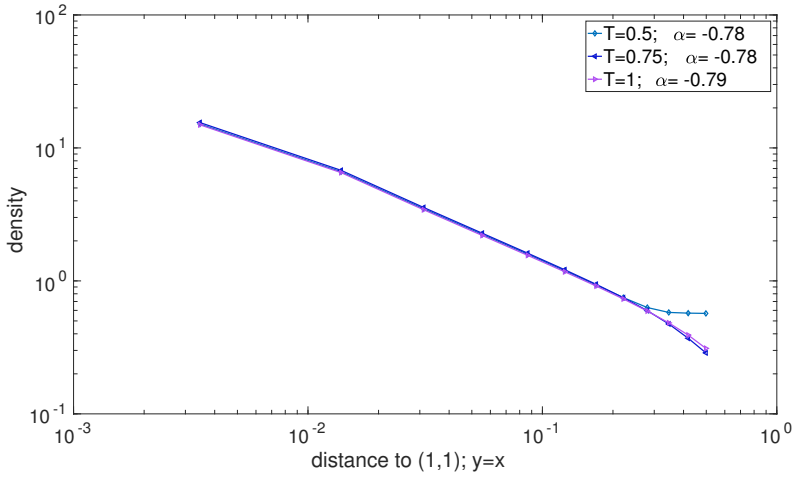


Figure 4.8: Asymptotic behavior of the solution to the single layer equation near corner along $y = x$, Example 2

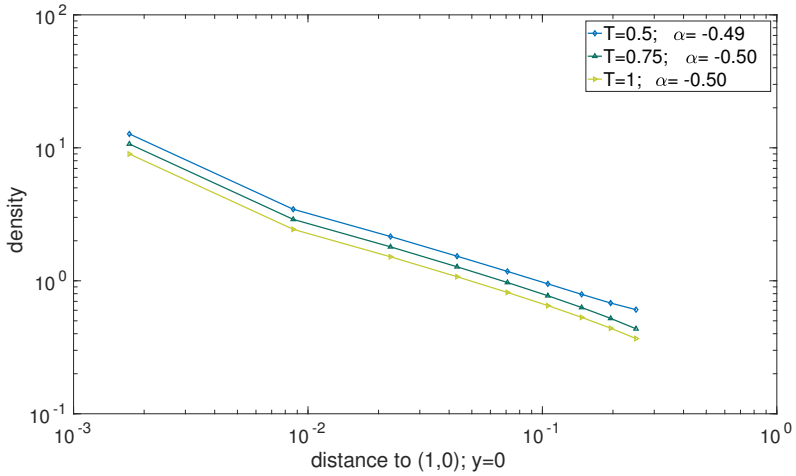


Figure 4.9: Asymptotic behavior of the solution to the single layer equation near edge along $y = 0$, Example 2

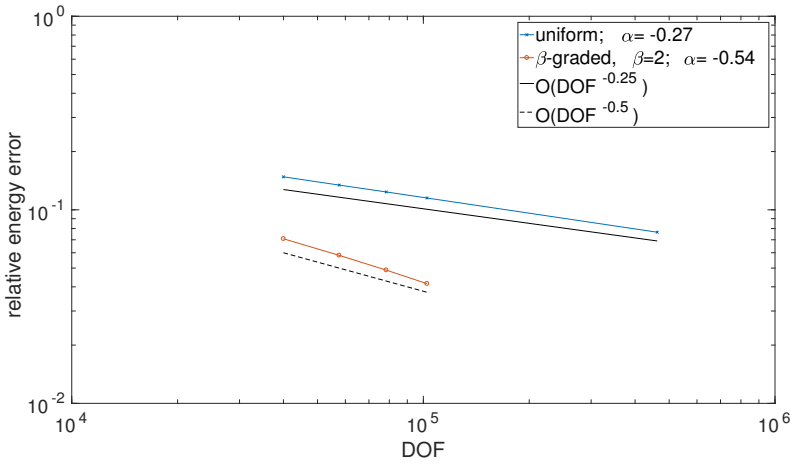


Figure 4.10: Energy error norm for single layer equation on square screen, Example 2

For Example 2, we finally consider the error compared to the benchmark solution on the 2-graded mesh. Like in Example 1, we consider the energy norm defined by the single layer operator. Figure 11 shows convergence of the norm with rates $-0.54$ on the 2-graded mesh, respectively $-0.27$ on the uniform mesh in terms of degrees of freedom. These closely mirror the approximation results, which predict an approximation error proportional to $\sim h$ (equivalently, $\sim DOF^{-\frac{1}{2}}$) on the 2-graded mesh, while the approximation error is $\sim h^{\frac{1}{2}}$ ($\sim DOF^{-\frac{1}{4}}$) on a uniform mesh. In particular, compared to Example 1, the corner singularities of the square screen do not affect the convergence rate.

To further probe the effect of the corners we also consider the $L_2$ norm in time of the sound pressure evaluated in a point. For applications the approximation of the sound pressure away from the screen is often the most relevant measure. We evaluate the sound pressure by substituting the density $\psi_{\Delta t,h}$ into the single layer potential, $p_{\Delta t,h} = S\psi_{\Delta t,h}$, and use a tensor product Gaussian quadrature with 400 nodes per triangle to evaluate the integral. Figure 4.11 shows the $L_2$ error in time of the sound pressure evaluated in three points outside of the screen, $(1, 1, 0.004)$, $(0.75, 0.75, 1)$ and $(1, 1.25, 0.25)$. In each of the points, the convergence is proportional to $\sim h^2$, resp. $\sim h$, as for the energy norm. However, while the convergence rate is in agreement with the energy norm, the error in the sound pressure strongly depends on the location of the point. In $(1, 1, 0.004)$, at

distance 0.004 from the corner of the screen, the error is an order of magnitude higher than in the points $(0.75, 0.75, 1)$ and $(1, 1.25, 0.25)$, which are at a distance of order 1.

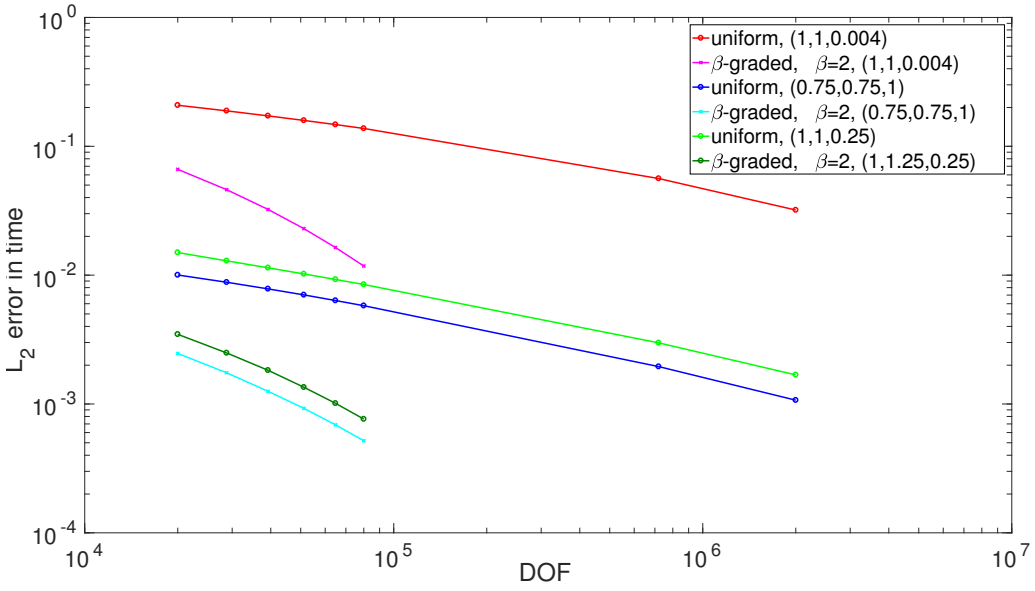


Figure 4.11: $L_2([0,T])$ error for the sound pressure in three points outside square screen, computed from single layer equation, Example 2

### 4.5.2 Hypersingular Operator

**Example 3.** *Using the discretisation from Section 4.2, we compute the solution to the integral equation* $W\phi = g$ *on* $\mathbb{R}^+_t \times \Gamma$ *with the circular screen* $\Gamma = \{(x, y, 0) : 0 \leq \sqrt{x^2 + y^2} \leq 1\}$ *depicted in Figure 4.1. We use the weak form* (4.5) *with linear ansatz and test functions in space, linear ansatz and constant test functions in time. Here,*

$$g(t,x) = (-\tfrac{3}{4} + \cos(\tfrac{\pi}{2}(4-t)) + \tfrac{\pi}{2}\sin(\tfrac{\pi}{2}(4-t)) - \tfrac{1}{4}(\cos(\pi(4-t)) + \pi\sin(\pi(4-t))))$$
$$\times [H(4-t) - H(-t)],$$

*where* $H$ *is the Heaviside function. The time discretisation errors are negligibly small in this numerical experiment, when the time step is chosen to be* $\Delta t = 0.01$*. We compute the solution up to* $T = 4$*. The finest graded mesh consists of 2662 triangles, and we use the solution on this mesh as reference solution using the same* $\Delta t = 0.01$*.*

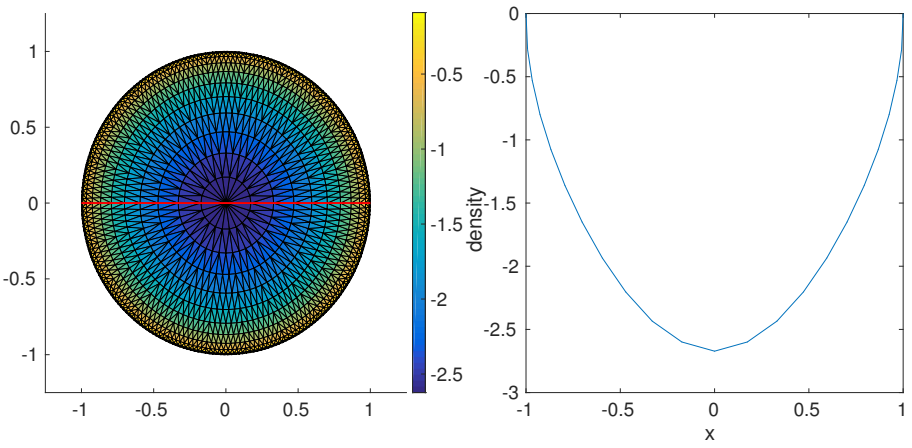


Figure 4.12: Solution of the hypersingular equation at $T = 2$ along $y = 0$ on the circular screen, Example 3

Figure 4.12 shows the density along a cross-section on a $\beta$-graded mesh with $\beta$=2 and 2662 triangles at time $T = 2$. The figure exhibits the edge singularities predicted by the decomposition (4.8) and illustrates the qualitative behavior of the solution.

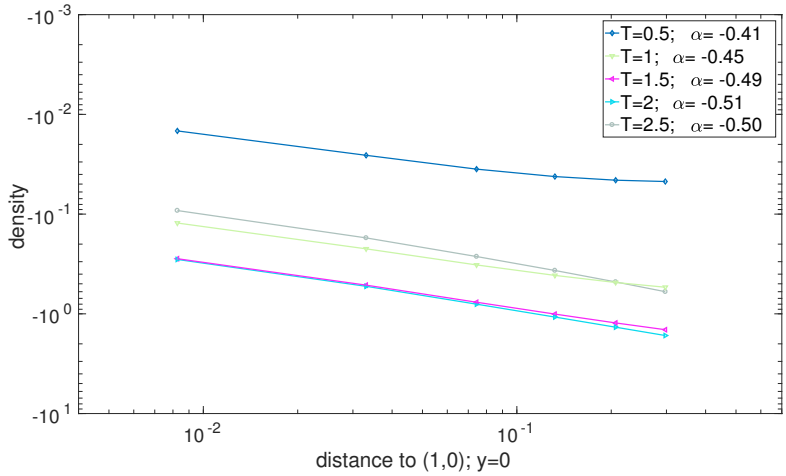


Figure 4.13: Asymptotic behavior of the solution to the hypersingular equation near edge along $y = 0$, Example 3

Figure 4.13 examines the detailed singular behavior at the circular edge along the $x$-axis near the point $(1, 0)$. It plots the numerical density at times up to $T = 2.5$ against the distance to the edge. For the singular exponents, we numerically obtain values within

5% of the theoretical value of $\frac{1}{2}$, except at the earliest time $T = 0.5$, when compute an exponent 0.41.

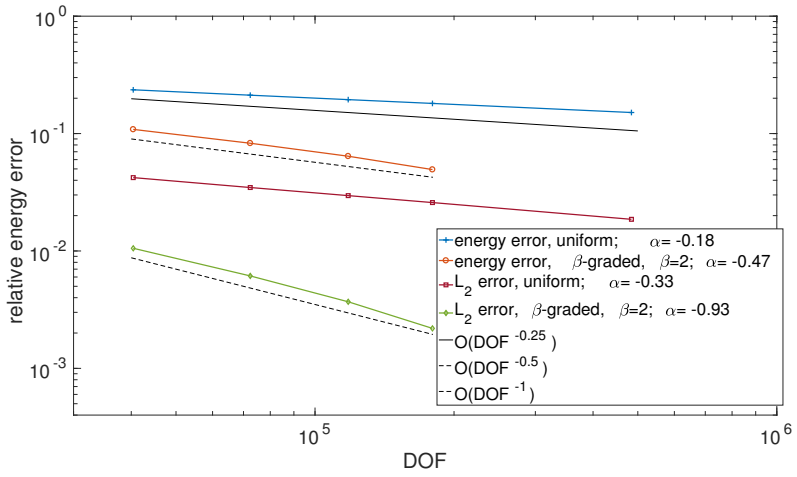


Figure 4.14: $L_2([0,T], L_2(\Gamma))$ and energy error for hypersingular equation on circular screen, Example 3

Finally, Figure 4.14 shows the error in both the energy and $L_2([0,T], L_2(\Gamma))$ norms with respect to the benchmark solution. The convergence rate in terms of the degrees of freedom on the 2-graded mesh is $-0.47$ in energy and $-0.93$ in $L_2$. It is in close agreement with a convergence proportional to $\sim h$ (equivalently, $\sim DOF^{-1/2}$) predicted by the approximation properties in the energy norm, and $\sim h^2$ (equivalently, $\sim DOF^{-1}$) in $L_2$. On the uniform mesh the rate is $-0.18$ in energy and $-0.33$ in $L_2$.

**Example 4.** *Using the discretisation from Section 4.2, with test and ansatz functions as in Example 3, we compute the solution to the integral equation $W\phi = g$ on $\mathbb{R}^+_t \times \Gamma$ with the square screen $\Gamma = [-1,1]^2 \times \{0\}$. We prescribe the right hand side*

$$g(t,x) = (-\frac{3}{4} + \cos(\frac{\pi}{2}(4-t)) + \frac{\pi}{2}\sin(\frac{\pi}{2}(4-t)) - \frac{1}{4}(\cos(\pi(4-t)) + \pi\sin(\pi(4-t))))$$
$$\times [H(4-t) - H(-t)],$$

*where $H$ is the Heaviside function, and set $\Delta t = 0.01$, $T = 4$. The finest graded mesh consists of* 2312 *triangles, and we use the solution on this mesh as reference solution using the same $\Delta t = 0.01$.*

The density along the diagonal $x = y$, respectively along $y = 0$, exhibit the corner and edge singularities predicted by the decomposition (4.12). The qualitative behavior of the solution at $T = 2$ along the diagonal $y = x$ of the square screen is shown in Figure 4.15, illustrating the singularity in the corners. Figure 4.16 shows the behaviour along $y = 0$, with the edge singularity at the boundary of the screen. As the solution to the hypersingular equation lies in $H^{\frac{1}{2}}_{\sigma}(\mathbb{R}^+, \tilde{H}^{\frac{1}{2}}(\Gamma))$, its conforming numerical approximation tends to zero at both edges and corners.

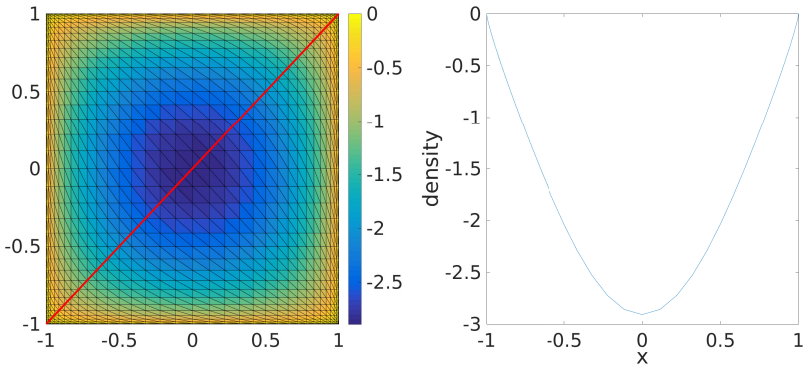


Figure 4.15: Solution of the hypersingular equation at $T = 2$ along $y = x$ on the square screen, Example 4

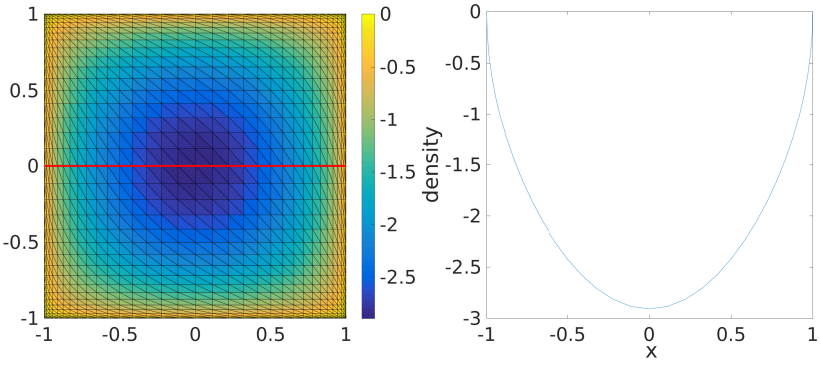


Figure 4.16: Solution of the hypersingular equation at $T = 2$ along $y = 0$ on the square screen, Example 4

Figure 4.17 examines the detailed singular behavior near the corner $(1, 1)$. It plots the numerical density at times up to $T = 2.5$ against the distance to the corner along the diagonal of the screen. The numerically computed singular exponents in the corner of

around 0.67 do not show good agreement with the exact corner exponent $\gamma$. The density as a function of $x$ for $y = 0$, perpendicular to the edge, is shown in Figure 4.18 at the same times. Unlike for the corner exponent, the numerically computed singular exponent at the edge, around 0.48, is witin 8% of the exact value $\frac{1}{2}$ for early times, and within 4% for $T \geq 1.5$.

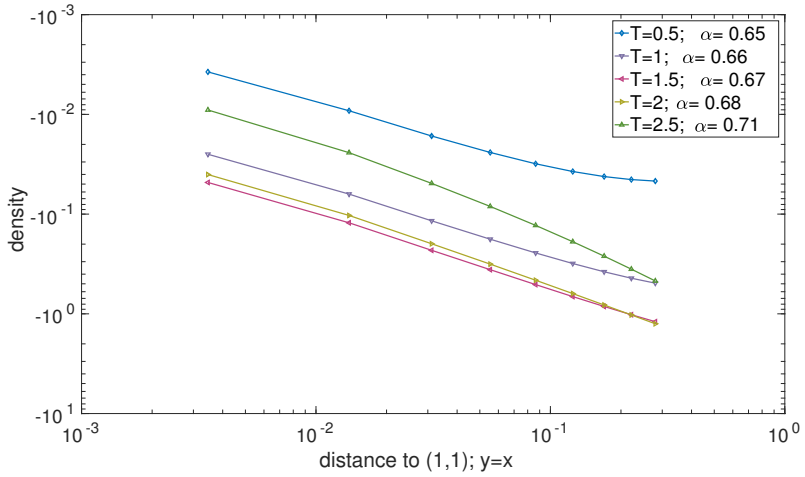


Figure 4.17: Asymptotic behavior of the solution to the hypersingular equation near corner along $y = x$, Example 3

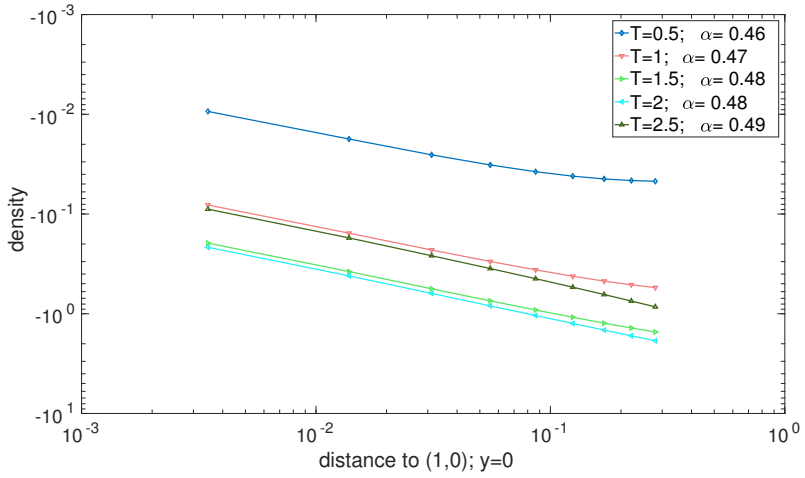


Figure 4.18: Asymptotic behavior of the solution to the hypersingular equation near edge along $y = 0$, Example 3

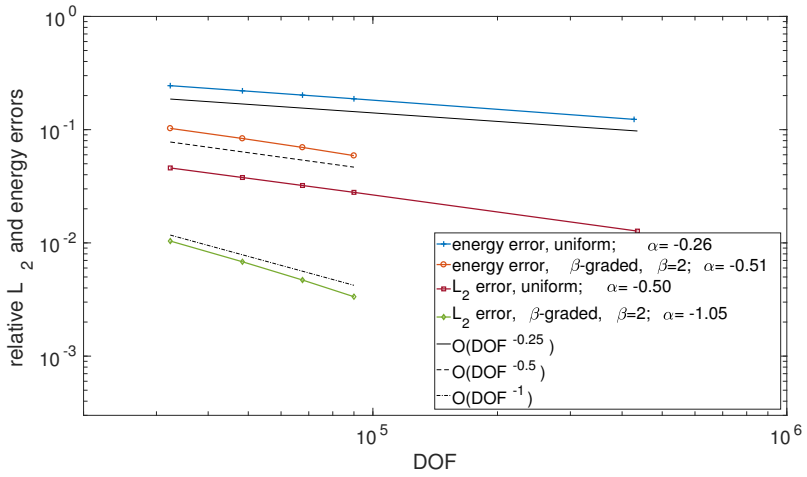


Figure 4.19: $L_2([0,T],L_2(\Gamma))$ and energy error for hypersingular equation on square screen, Example 4

Finally, Figure 4.19 shows the error in both the energy and $L_2([0,T],L_2(\Gamma))$ norms with respect to the benchmark solution. The convergence rate in terms of the degrees of freedom on the 2-graded mesh is $-0.51$ in energy and $-1.05$ in $L_2$. On the uniform mesh the rate is $-0.26$ in energy and $-0.50$ in $L_2$. The rates on the 2-graded meshes are in close agreement with a convergence proportional to $\sim h$ (equivalently, $\sim DOF^{-1/2}$) predicted by the approximation properties in the energy norm, and $\sim h^{1/2}$ ($\sim DOF^{-1/4}$) on uniform meshes. Also in $L_2$ norm, the convergence corresponds to the expected rates: Approximately $\sim h^2$ (equivalently, $\sim DOF^{-1}$) on 2-graded meshes, $\sim h$ (equivalently, $\sim DOF^{-1/2}$) on uniform meshes. In all cases the convergence is twice as fast on the 2-graded compared to the uniform meshes.

### 4.5.3 Dirichlet-to-Neumann Operator

In addition to the single layer and hypersingular operators in the previous subsections, we also consider the Dirichlet-to-Neumann operator on the screen. Compared to the hypersingular operator, the Dirichlet-to-Neumann operator is not available in closed form and requires approximation. It is of interest to see the influence of the approximation of the operator on the numerical solution.

**Example 5.** *Using the discretisation from Section 4.2, we compute the solution to the*

*integral equation* $\mathcal{S}u = h$ *on* $\mathbb{R}_t^+ \times \Gamma$ *with* $\Gamma = [-1,1]^2 \times \{0\}$. *We prescribe the right hand side*

$$h(t,x) = (-\tfrac{3}{4} + \cos(\tfrac{\pi}{2}(4-t)) + \tfrac{\pi}{2}\sin(\tfrac{\pi}{2}(4-t)) - \tfrac{1}{4}(\cos(\pi(4-t)) + \pi\sin(\pi(4-t))))$$
$$\times [H(4-t) - H(-t)],$$

*where* $H$ *is the Heaviside function, and set* $\Delta t = 0.01$, $T = 0.65$. *The finest graded mesh consists of* 2312 *triangles, and we use the solution on this mesh as reference solution using the same* $\Delta t = 0.01$.

Figures 4.20 and 4.21 show the density along a cross-section and along a longitudinal section on a $\beta$-graded mesh with $\beta$=2 and 2312 triangles at time $T = 0.5$. Both figures exhibit the corner and edge singularities predicted by the decomposition 4.12 and illustrate the qualitative behavior of the solution. As the solution to the Dirichlet-to-Neumann equation lies in $H_\sigma^{\frac{1}{2}}(\mathbb{R}^+, \tilde{H}^{\frac{1}{2}}(\Gamma))$, its conforming numerical approximation is zero at the boundary of the screen.

Figure 4.22 examines the detailed singular behavior near the corner $(1,1)$. It plots the numerical density at times $T = 0.25,\ 0.5,\ 0.6,\ 0.65$ against the distance to the corner along the diagonal of the screen. In the log-log plot the slope of the curve near 0 corresponds to the corner exponent in the singular expansion. Similarly, Figure 4.23 shows the density as a function of $y$ for $x = -0.8754$, perpendicular to the edge, at the same times. The numerically computed singular exponents of the edge, around 0.4, are in qualitative agreement with the exact value $\frac{1}{2}$. For the corner, the computed value above 0.6 differs significantly from the exact value $\gamma$. A similar difference was observed in the previous section for the hypersingular operator, so that the approximation involved in computing the Dirichlet-to-Neumann operator is not the source of this discrepancy.

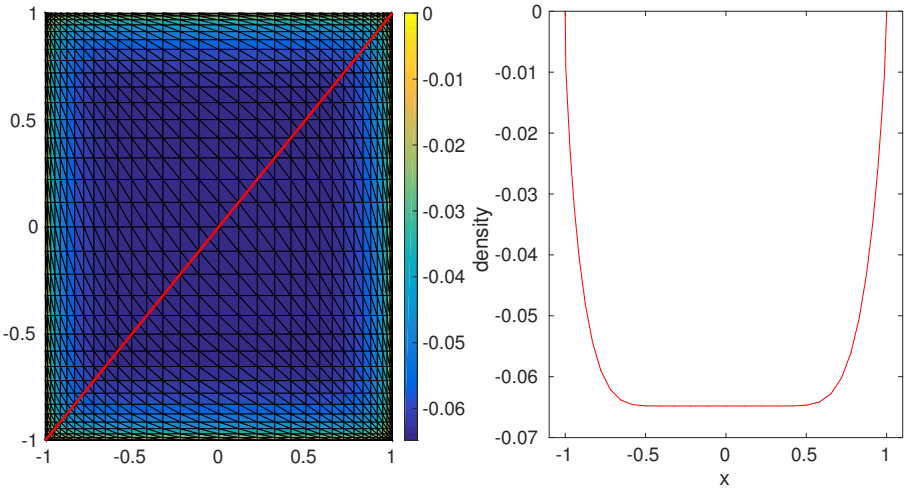


Figure 4.20: Solution of the Dirichlet-to-Neumann equation at $T = 0.65$ along $y = x$ on the square screen, Example 5

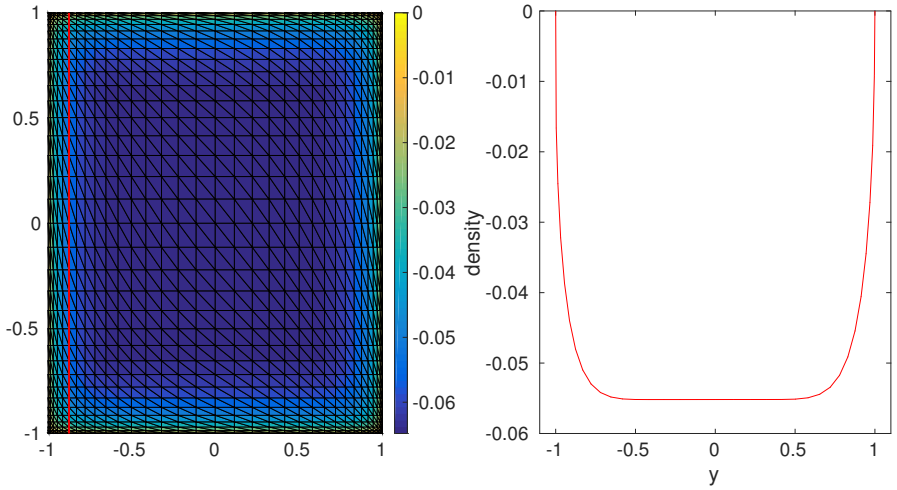


Figure 4.21: Solution of the Dirichlet-to-Neumann equation at $T = 0.65$ along $x = -0.8754$ on the square screen, Example 5

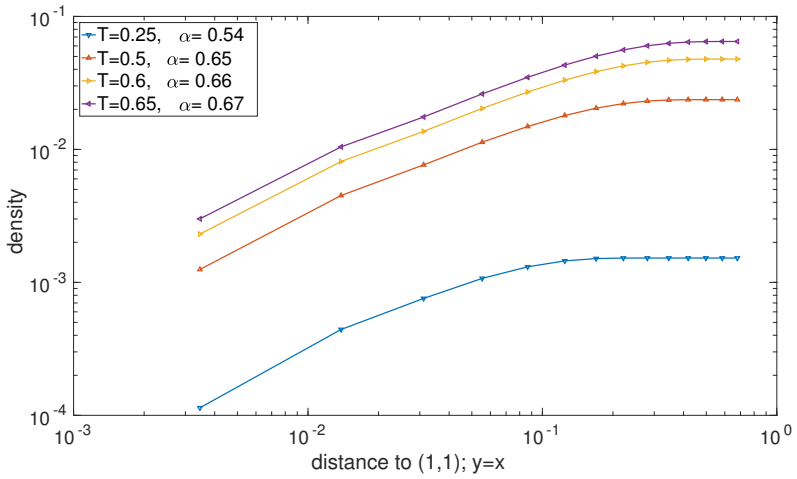


Figure 4.22: Asymptotic behavior of the solution to the Dirichlet-to-Neumann equation near corner along $y = x$, Example 5

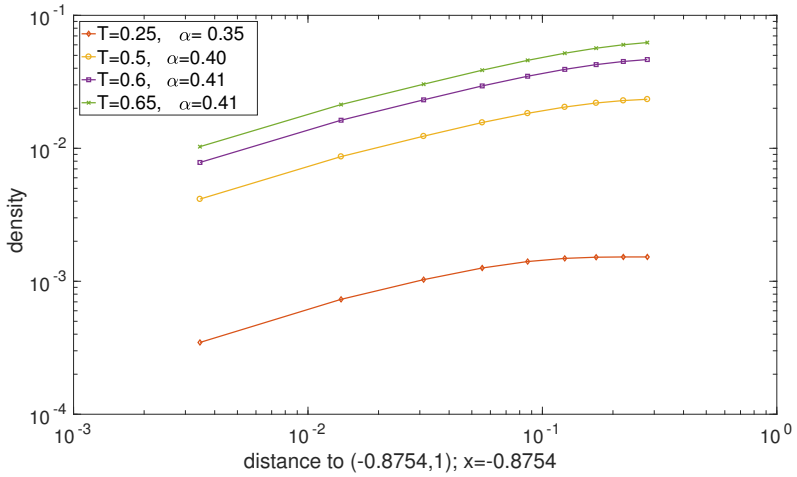


Figure 4.23: Asymptotic behavior of the solution to the Dirichlet-to-Neumann equation near edge along $x = -0.8754$, Example 5

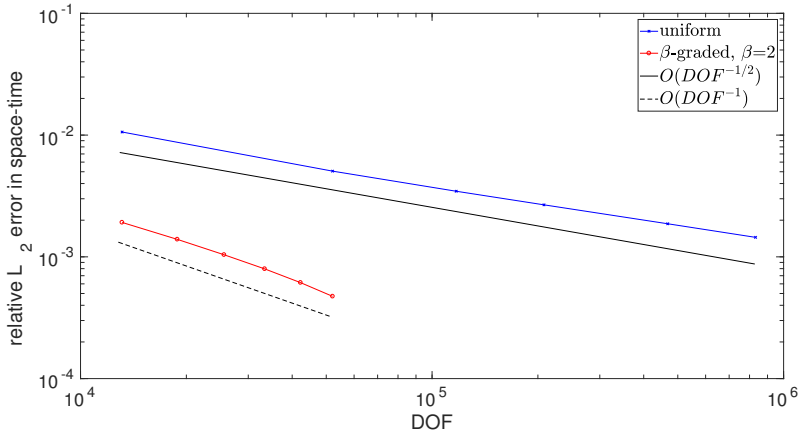


Figure 4.24: Error in $L_2([0,T], L_2(\Gamma))$ norm for Dirichlet-to-Neumann equation on square screen, Example 5

Figure 4.24 shows the error in $L^2([0,T]\times\Gamma)$ compared to the benchmark solution. The convergence in this norm is proportional to $\sim h^2$ (equivalently, $\sim DOF^{-1}$) on the 2-graded mesh, while the convergence is $\sim h^1$ ($\sim DOF^{-\frac{1}{2}}$) on a uniform mesh. This coincides with the rates expected from the approximation property of the graded, respectively uniform meshes, and it is also in agreement with the rates obtained for the hypersingular operator on the square screen in the previous section.

## 4.6 Applications to Traffic Noise: Horn Effect

For applications in traffic noise, the natural (simplified) geometry is that of a half-space $\mathbb{R}^3_+$ with a tyre, as displayed in Figure 4.25. The horn like geometry between the tyre and the street amplifies sound sources close to the contact patch, and it is of interest to compute the amplification for a broad band of frequencies. See also [22, 87]. See [74, 77] for the complementary problem of the tyre dynamics in contact with the road.

We consider the wave equation for the sound pressure scattered by the tyre, with homogeneous Neumann conditions on the street $\Gamma_\infty = \mathbb{R}^2 \times \{0\}$ and inhomogeneous Neumann conditions on the tyre. Note that the boundary conditions jump in the cuspidal geometry between the tyre and the road surface. The relevant Green's function in $\mathbb{R}^3_+$ is

given by

$$G(t,x,y) = \frac{\delta(t-|x-y|)}{4\pi|x-y|} + \frac{\delta(t-|x-y'|)}{4\pi|x-y'|} \ , \tag{4.17}$$

where $y'$ is the reflection of $y$ on $\Gamma_\infty$. We use it in a single layer potential ansatz for a sound pressure scattered by the tyre,

$$p(t,x) = \frac{1}{4\pi}\int_\Gamma \frac{\phi(t-|x-y|,y)}{|x-y|}\,ds_y + \frac{1}{4\pi}\int_\Gamma \frac{\phi(t-|x-y'|,y)}{|x-y'|}\,ds_y \ , \tag{4.18}$$

with $\phi(s,y) = 0$ for $s \le 0$. The Neumann problem for the scattered sound translates into an integral equation for $\phi$:

$$(-I+K')\,\phi(t,x) = 2\frac{\partial p}{\partial n}(t,x) = -2\frac{\partial p^I}{\partial n}(t,x) \ , \tag{4.19}$$

with $p^I$ the incoming wave and the adjoint double layer operator $K'$ from (3.3),

$$\begin{aligned} K'\phi(t,x) =& \frac{1}{2\pi}\int_\Gamma \frac{n_x^\top(y-x)}{|x-y|}\left(\frac{\phi(t-|x-y|,y)}{|x-y|^2} + \frac{\dot\phi(t-|x-y|,y)}{|x-y|}\right) ds_y \\ &+ \frac{1}{2\pi}\int_\Gamma \frac{n_x^\top(y'-x)}{|x-y'|}\left(\frac{\phi(t-|x-y'|,y)}{|x-y'|^2} + \frac{\dot\phi(t-|x-y'|,y)}{|x-y'|}\right) ds_y. \end{aligned}$$

The weak formulation reads:
Find $\phi \in H_\sigma^{\frac{1}{2}}(\mathbb{R}^+, \widetilde{H}^{-\frac{1}{2}}(\Gamma))$ such that for all test functions $\psi \in H_\sigma^{\frac{1}{2}}(\mathbb{R}^+, H^{-\frac{1}{2}}(\Gamma))$

$$\int_0^\infty \int_\Gamma (-I+K')\,\phi\ \psi\ \ ds_x\, d_\sigma t = -2\int_0^\infty \int_\Gamma \frac{\partial p^I}{\partial n}\ \psi\, ds_x\, d_\sigma t \ . \tag{4.20}$$

It is discretized with piecewise constant ansatz and test functions $\psi_i^h(x)\gamma_{\Delta t}^n(t) \in V_{t,h}^{0,0}$ in space and time.

To obtain the sound amplification for the entire frequency spectrum in one time domain computation, we consider the sound emitted by a Dirac point source. It is located in the

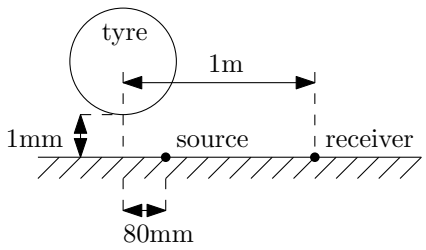


Figure 4.25: Cross section of geometrical setup for horn effect.

point $y_{src} = (0.08, 0, 0)$ near the horn,

$$p^I = \frac{\delta(t - |x - y_{\text{src}}|)}{4\pi|x - y_{\text{src}}|} + \frac{\delta(t - |x - y'_{\text{src}}|)}{4\pi|x - y'_{\text{src}}|} \ . \tag{4.21}$$

The right hand side of the discretisation of the integral equation (4.20) is calculated to be [22]

$$-2\int_0^\infty \int_\Gamma \frac{\partial p^I}{\partial n}\psi_i^h \gamma_{\Delta t}^n \, ds_x \, dt = -\int_{T_i \cap E(y_{\text{src}})} \frac{n_x^\top (y_{\text{src}} - x)}{\pi |x - y_{\text{src}}|^3} \, ds_x + n_x^\top (y_{\text{src}} - x) \left\{ \frac{\zeta(t_{n-1})}{\pi t_{n-1}^2} - \frac{\zeta(t_n)}{\pi t_n^2} \right\} \ .$$

The first term is an integral over the domain of influence $E(y_{\text{src}}) = \{x \in \Gamma : t_{n-1} \leq |x - y_{\text{src}}| \leq t_n\}$ of $y_{\text{src}}$, intersected with $T_i = \text{supp } \psi_i^h$, and it is computed in the same way as the entries of the Galerkin matrix. In the second term, $\zeta(t)$ denotes the length of the curve segment $T_i \cap \{|x - y_{src}| = t\}$ inside the triangle $T_i$.

After solving the discretisation of (4.20) for the density $\phi$, we obtain the sound pressure $p$ in the receiver point $x_{fp} = (1, 0, 0)$ from (4.18). From [87, Eq. 7], the amplification factor is given by:

$$\Delta L_H(\omega) = 20 \log_{10} \left( \frac{|\hat{p}(\omega, x_{fp}) + \hat{p}^I(\omega, x_{fp})|}{|\hat{p}^I(\omega, x_{fp})|} \right) \ .$$

Here, $\hat{p}$ and $\hat{p}^I$ denote the Fourier transformed incident and scattered sound pressure fields. The Fourier transformation is calculated using a discrete FFT, where the time step size is the same as for the computation of the density.

In the geometry given by Figure 4.25, we compute the sound amplification in standard units for a grown slick 205/55R16 tyre at 2 bar pressure. It is subject to 3415N axle load at 50 km/h on a street with an ISO 10844 surface, and a mesh with 6027 nodes is depicted in Figure 4.26. We use this and a refined graded mesh and consider the sound amplification for frequencies between 200 and 2000 Hz. The total time interval is $T = 24$ and the

time step sizes $\Delta t = 0.005,\ 0.01,\ 0.04$. For smaller time step sizes more reflections in the horn can be resolved, and these are responsible for the sound amplification.

We compare the results for the uniform mesh with a refined, graded-like mesh with grading parameter $\beta = 2$, see Figure 4.26. Figure 4.27 shows approximations of the amplification factor in the horn geometry, discretized using the graded mesh, across the frequency range for the time step sizes $\Delta t = 0.005,\ 0.01,\ 0.04$. We also show the approximation given by the uniform tyre mesh for $\Delta t = 0.005$. The figure, in particular, exhibits several resonances between 1000 and 2000 Hz, at which the different approximations lead to significant differences in the computed amplification factors.

The differences between the computed amplification factors are depicted in Figure 4.28. The first subfigure considers the differences between the graded and uniform meshes for a given time step size, $\Delta t = 0.005,\ 0.01,\ 0.04$. Outside the resonance frequencies the differences are negligible. Especially in the strong resonances around 1300 and 1900 Hz, however, the difference between graded and uniform meshes becomes more and more relevant for smaller $\Delta t$, as the small time step allows to resolve the reflections in the horn geometry more accurately. The second subfigure of Figure 4.28 compares the computed amplification for graded meshes for different $\Delta t$. As before, the differences are mostly relevant near resonance frequencies, and the discretisation error for a fixed mesh decreases with $\Delta t$. For $\Delta t = 0.005$ the differences between the spatial, resp. temporal discretisations in Figure 4.28 are both around 6 dB near 1300 Hz. Such differences in sound pressure are significant to the human perception. They indicate the relevance of graded meshes for computations of traffic noise.

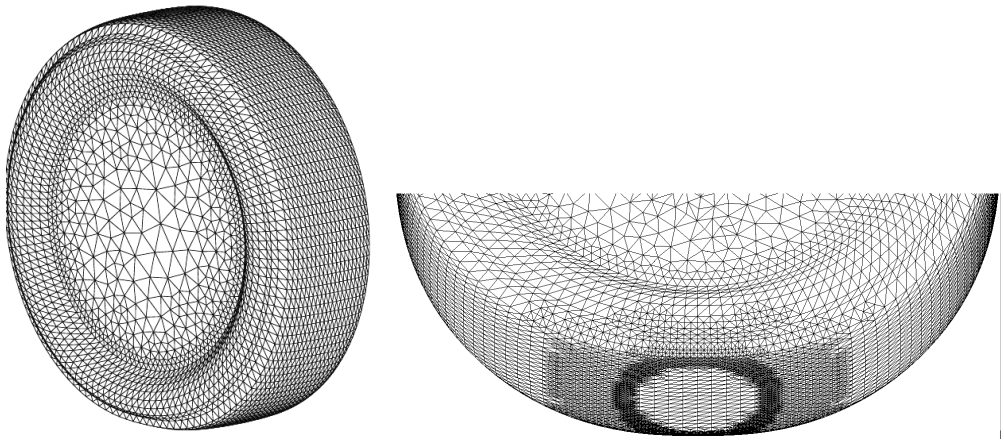

(a) (b)

Figure 4.26: Mesh of (a) slick 205/55R16 tyre and (b) graded refinement.

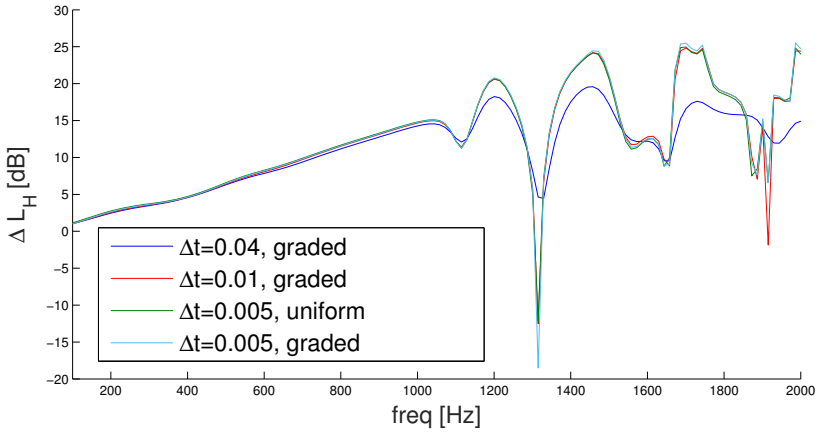


Figure 4.27: Amplification due to horn effect: Graded mesh approximations for different $\Delta t$, compared to a uniform mesh approximation.

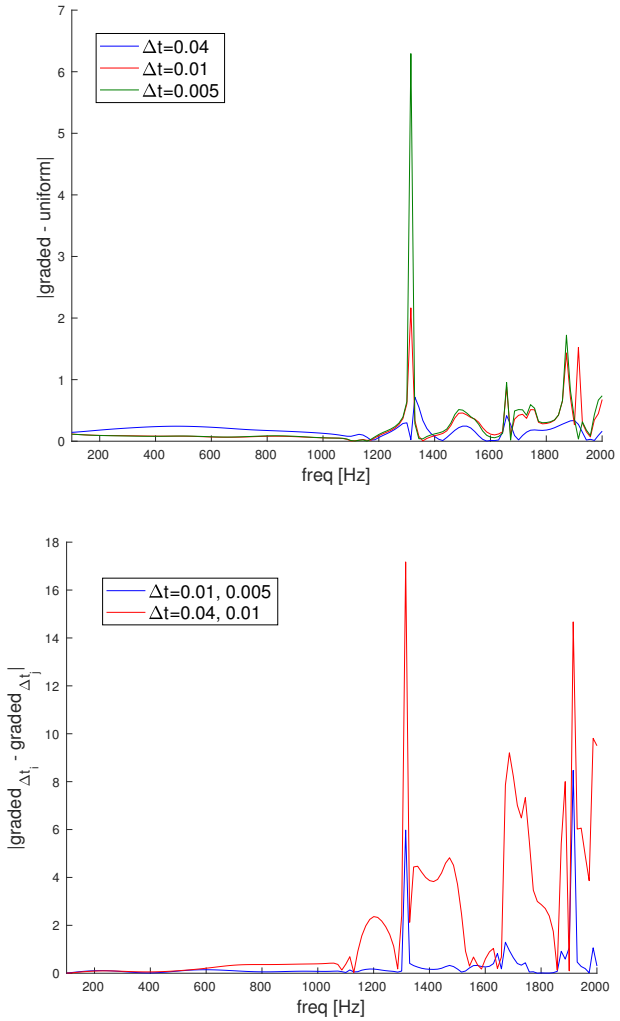


Figure 4.28: Differences of amplification factors in $dB$ between graded and uniform meshes for fixed $\Delta t$, resp. between graded meshes for different $\Delta t$.

# Chapter 5

# Adaptive Methods

This chapter is based on joint work [58] with H. Gimperlein, C. Ozdemir, and E.P. Stephan.

## 5.1 Introduction

The efficient numerical treatment of boundary integral equations using adaptive mesh refinement procedures has been extensively investigated for the numerical solution of homogeneous elliptic problems in unbounded domains [27, 29]. See [69] for a recent exposition.

In this chapter we investigate the extension of the a posteriori error analysis and adaptive mesh refinement procedures to initial-boundary value problems for the wave equation. We prove a reliable a posteriori error estimate of residual type for a large class of conforming discretisations. It is efficient for a time-domain boundary element method on a quasi-uniform mesh. The error estimate defines an adaptive mesh refinement procedure, which recovers the convergence rates known for time-independent screen problems.

There has been recent interest in the solution of such problems on adapted meshes. Similar to the elliptic case, singularities of the solution may appear at singular points of the boundary, as discussed in [84, 85, 105], and in trapping regions. Time-independent graded meshes have been shown to recover quasi-optimal convergence rates for edge and corner singularities [61]. First steps towards time-adaptivity are due to Sauter and Veit [109] in 2 dimensions, and also convolution quadrature methods with graded, non-adaptively

chosen time steps have been studied, for example in [111]. Gläfke [66] showed first results towards space-time refinements in 2 dimensions, and in unpublished work Abboud investigates ZZ error indicators for screen problems.

To describe the main results, we consider the wave equation

$$\partial_t^2 u - \Delta u = 0 \ , \quad u = 0 \ \text{ for } \ t \leq 0 \ ,$$

in the complement of a polyhedral domain $\Omega \subset \mathbb{R}^d$, with an emphasis on the challenging case $d = 3$. On the boundary $\Gamma = \partial\Omega$ both Dirichlet and acoustic boundary conditions,

$$u = f \ , \qquad \partial_n u = f \ , \qquad \text{resp.} \qquad \partial_n u - \alpha \partial_t u = f \ ,$$

are considered. Here $f$ is given, $\nu$ is the outer unit normal vector to $\Gamma$, and $0 < \alpha, \alpha^{-1} \in L^\infty(\Gamma)$.

Following Bamberger and Ha Duong [16], we recast the boundary problem as a time dependent boundary integral equation. The Dirichlet problem is equivalent to a hyperbolic variant of Symm's integral equation:

$$Vp(t,x) = \int_{\mathbb{R}^+ \times \Gamma} G(t-\tau, x, y) p(\tau, y) \ d\tau \ ds_y = f(t,x) \ , \tag{5.1}$$

Here $G$ is a fundamental solution of the wave equation

$$G(t-s,x,y) = \frac{H(t-s-|x-y|)}{2\pi\sqrt{(t-s)^2 + |x-y|^2}} \qquad \text{(2d)} \tag{5.2}$$

$$G(t-s,x,y) = \frac{\delta(t-s-|x-y|)}{4\pi|x-y|} \qquad \text{(3d)} \tag{5.3}$$

where H is the Heaviside function

$$H(x) := \begin{cases} 0, x < 0 \\ 1, x \geq 0. \end{cases}$$

Our results apply, in particular, to a Galerkin discretisation of the weak form of (5.1),

$$\int_{\mathbb{R}^+}\int_{\Gamma} V\partial_t\phi(t,x)\ \psi(t,x)\ ds_x\, d_\sigma t = \int_{\mathbb{R}^+}\int_{\Gamma} \partial_t f(t,x)\ \psi(t,x)\ ds_x\, d_\sigma t\ , \tag{5.4}$$

$d_\sigma t = e^{-2\sigma t}dt$ with $\sigma > 0$, in space-time anisotropic Sobolev spaces. We write (5.4) in the form $B_D(\phi,\psi) = \langle f, \phi\rangle$. We show:

**Theorem D:** Let $\phi \in H^0_\sigma(\mathbb{R}^+, H^{-\frac{1}{2}}(\Gamma))$ be the solution to (5.4), and let $\phi_{h,\Delta t} \in H^0_\sigma(\mathbb{R}^+, H^{-\frac{1}{2}}(\Gamma))$ such that $\mathcal{R} = \partial_t f - \mathcal{V}\partial_t\phi_{h,\Delta t} \in H^0_\sigma(\mathbb{R}^+, H^1(\Gamma))$. Then

$$\|\phi - \phi_{h,\Delta t}\|^2_{0,-\frac{1}{2}} \lesssim \sum_{i,\Delta} \max\{\Delta t, h_\Delta\}\ \|\mathcal{R}\|^2_{0,1,[t_i,t_{i+1})\times\Delta}\ .$$

If $\phi_{h,\Delta t}$ is a Galerkin solution of (5.4) on a quasi-uniform mesh, then

$$\max\{\Delta t, h\}\|\mathcal{R}\|^2_{0,1-\epsilon} \lesssim \|\phi - \phi_{h,\Delta t}\|^2_{2,-\frac{1}{2}}\ .$$

Note the loss of time derivatives between the upper and lower bound of the error, in the first Sobolev index. The loss is well-known for error estimates for hyperbolic problems [71]. Our arguments generalize to give reliable a posteriori estimates for the acoustic boundary problem, see Section **??**.

The residual error estimate from Theorem D is used to define adaptive mesh refinements in space, based on the 4 steps Solve, Estimate, Mark, Refine. Numerical experiments confirm the efficiency and reliability of the estimate in examples. For screen problems they recover the convergence rates known for elliptic problems.

This work builds on the numerical analysis of adaptive boundary element methods for the Laplace equation, both for Symm's integral equation and the hypersingular equation [27, 29, 30, 31]. Work on different types of error indicators in the time-independent case includes ZZ [28] and Faermann indicators [49, 50]. We also mention [128] for an earlier approach. A comparison of different indicators in the time-domain will be the subject of future research.

*Structure of this chapter:* Section 5.2 recalls the boundary integral operators associated to the wave equation as well as their mapping properties between suitable space-time anisotropic Sobolev spaces. The Sobolev spaces are discretized using tensor products of piecewise polynomials in space and time. Section 5.3 presents a corresponding space-time discretisation for the formulation of the Dirichlet problem in terms of the single layer operator and derives a reliable a posteriori error estimate for quasi-uniform meshes, using a canonical approach which will readily adapt to other settings. A second subsection analyzes an acoustic boundary problem, a system of equations involving in addition the double layer, adjoint double layer and hypersingular operators. Section 5.4 then localizes the space-time Sobolev norm to derive the general upper estimate for the Dirichlet problem in Theorem D. The upper estimates are complemented by a lower bound for the error of a Galerkin approximation on quasi-uniform meshes in Section 5.5. Section 5.7 discusses some algorithmic properties of the implementation, before numerical experiments are used to confirm the theoretical results in Section 5.8.

## 5.2 Discretisation

For the time discretisation we consider a uniform decomposition of the time interval $\mathbb{R}^+$ into subintervals $I_n = [t_{n-1}, t_n)$ with time step $|I_n| = \Delta t$, such that $t_n = n\Delta t$, $n = 0, 1, \ldots$.
We choose a basis $\{\varphi_j^p\}$ of the space $V_h^p$ of piecewise polynomial functions of degree $p$ in space (continuous if $p \geq 1$) and a basis $\{\beta^{j,q}\}$ of the space $V_{\Delta t}^q$ of piecewise polynomial functions of degree of $q$ in time (continuous and vanishing at $t = 0$ if $q \geq 1$).
We denote the spatial mesh $\{T_1, \cdots, T_{N_s}\}$ for $\Gamma$ by $\mathcal{T}_S$, the finite temporal mesh $\{[0, t_1), [t_1, t_2), \cdots, [t_{N_t-}$ by $\mathcal{T}_T$.
We consider the tensor product of the approximation spaces in space and time, $V_h^p$ and $V_{\Delta t}^q$, associated to the space–time mesh $\mathcal{T}_{S,T} = \mathcal{T}_S \times \mathcal{T}_T$, and we write

$$V_{h,\Delta t}^{p,q} = V_h^p \otimes V_{\Delta t}^q \,.$$

We consider the orthogonal projections $\Pi_{\Delta t}$ from $L^2(\mathbb{R}_+)$ to $V_{\Delta t}^q$, resp. $\Pi_h$ from $L^2(\Gamma)$ to $V_h^p$. See [61] for a discussion of their properties and those of their composition $\widetilde{\Pi}_{h,\Delta t}$.

## 5.3 A Posteriori Error Estimates – Reliability

### 5.3.1 Dirichlet Problem

We recall the basic properties of the bilinear form $B_D$ of the Dirichlet Problem, defined in (5.4).

As shown in [71], the bilinear form $B_D$ is continuous, and also weakly coercive:

**Proposition 17.** *For every $\phi, \psi \in H^1_\sigma(\mathbb{R}^+, H^{-\frac{1}{2}}(\Gamma))$ there holds:*

$$|B_D(\phi, \psi)| \leq C\|\phi\|_{1,-\frac{1}{2},\Gamma}\|\psi\|_{1,-\frac{1}{2},\Gamma}$$

*and*

$$\|\phi\|^2_{0,-\frac{1}{2},\Gamma} \leq CB_D(\phi, \phi).$$

We consider a conforming Galerkin discretisation of the Dirichlet problem (5.4) in a subspace $V \subset H^1_\sigma(\mathbb{R}^+, H^{-\frac{1}{2}}(\Gamma))$, which reads as follows: Find $\phi_{h,\Delta t} \in V$ such that

$$B_D(\phi_{h,\Delta t}, \psi_{h,\Delta t}) = \langle \partial_t f, \psi_{h,\Delta t} \rangle \ , \tag{5.5}$$

for all $\psi_{h,\Delta t} \in V$.

In our applications we consider the subspace $V = V^{p,q}_{h,\Delta t}$, but also time discretisations based on smooth functions are of interest [109].

The well-posedness of the continuous and discretized problems is a basic consequence of Proposition 17:

**Corollary 18.** *Let $f \in H^2_\sigma(\mathbb{R}^+, H^{\frac{1}{2}}(\Gamma))$. Then the Dirichlet problem* (5.4) *and its discretisation* (5.5) *admit unique solutions $\phi, \phi_{h,\Delta t} \in H^1_\sigma(\mathbb{R}^+, H^{-\frac{1}{2}}(\Gamma))$, respectively $\|\phi\|_{1,-\frac{1}{2},\Gamma}, \|\phi_{h,\Delta t}\|_{1,-\frac{1}{2},\Gamma} \lesssim \|f\|_{2,\frac{1}{2},\Gamma}$.*

We also note the Galerkin orthogonality:

$$B_D(\phi - \phi_{h,\Delta t}, \psi_{h,\Delta t}) = 0 \qquad \forall \psi_{h,\Delta t} \in V \, .$$

Using ideas going back to Carstensen [27] and Carstensen and Stephan [29] for the boundary element method for elliptic problems, we obtain an a posteriori error estimate for the Galerkin solution to the Dirichlet problem.

**Theorem 19.** *Let* $V = V_{h,\Delta t}^{p,q}$ *and* $\phi, \phi_{h,\Delta t} \in H_\sigma^1(\mathbb{R}^+, H^{-\frac{1}{2}}(\Gamma))$ *the solutions to* (5.4) *resp.* (5.5).
*Assume that* $R = \partial_t f - V \partial_t \phi_{h,\Delta t} \in H_\sigma^0(\mathbb{R}^+, H^1(\Gamma))$. *Then*

$$\begin{aligned} \|\phi - \phi_{h,\Delta t}\|_{0,-\frac{1}{2},\Gamma}^2 &\lesssim \|R\|_{0,1,\Gamma} \big( \Delta t \|\partial_t R\|_{0,0,\Gamma} + \|h \cdot \nabla R\|_{0,0,\Gamma} \big) \\ &\lesssim \max\{\Delta t, h\} (\|\partial_t R\|_{0,0,\Gamma} + \|\nabla R\|_{0,0,\Gamma})^2 \end{aligned}$$

*Proof of Theorem 19.* We first note that for all $\psi_{h,\Delta t} \in V_{h,\Delta t}^{p,q}$

$$\begin{aligned} &\|\phi - \phi_{h,\Delta t}\|_{0,-\frac{1}{2},\Gamma}^2 \lesssim B_D(\phi - \phi_{h,\Delta t}, \phi - \phi_{h,\Delta t}) \\ &= \int_{\mathbb{R}^+} \int_\Gamma \partial_t f (\phi - \phi_{h,\Delta t}) \, ds_x \, d_\sigma t - B_D(\phi_{h,\Delta t}, \phi - \phi_{h,\Delta t}) \\ &= \int_{\mathbb{R}^+} \int_\Gamma \partial_t f (\phi - \psi_{h,\Delta t}) \, ds_x \, d_\sigma t - B_D(\phi_{h,\Delta t}, \phi - \psi_{h,\Delta t}) \\ &= \int_{\mathbb{R}^+} \int_\Gamma (\partial_t f - V \partial_t \phi_{h,\Delta t})(\phi - \psi_{h,\Delta t}) \, ds_x \, d_\sigma t \, . \end{aligned}$$

The last term may be estimated by:

$$\begin{aligned} &\int_{\mathbb{R}^+} \int_\Gamma (\partial_t f - V \dot{\phi}_{h,\Delta t})(\phi - \psi_{h,\Delta t}) \, ds_x \, d_\sigma t \\ &\leq \|R\|_{0,\frac{1}{2},\Gamma} \|\phi - \psi_{h,\Delta t}\|_{0,-\frac{1}{2},\Gamma} \, . \end{aligned}$$

We use $\psi_{h,\Delta t} = \phi_{h,\Delta t}$ together with the interpolation inequality

$$\|R\|_{0,\frac{1}{2},\Gamma}^2 \leq \|R\|_{0,0,\Gamma} \|R\|_{0,1,\Gamma} \, .$$

As the residual is perpendicular to $V_{h,\Delta t}^{p,q}$,

$$\begin{aligned}\|R\|_{0,0,\Gamma}^2 = \langle R, R\rangle &= \langle R, R - \widetilde{\psi}_{h,\Delta t}\rangle \\ &\leq \|R\|_{0,0,\Gamma}\|R - \widetilde{\psi}_{h,\Delta t}\|_{0,0,\Gamma}\end{aligned}$$

for all $\widetilde{\psi}_{h,\Delta t} \in V_{h,\Delta t}^{p,q}$, we obtain

$$\|R\|_{0,0,\Gamma} \leq \inf\{\|R - \widetilde{\psi}_{h,\Delta t}\|_{0,0,\Gamma} : \widetilde{\psi}_{h,\Delta t} \in V_{h,\Delta t}^{p,q}\} \ .$$

Choosing $\widetilde{\psi}_{h,\Delta t} = \widetilde{\Pi}_{h,\Delta t} R$, based on the interpolation operator defined earlier, we obtain

$$\|R\|_{0,0,\Gamma} \lesssim \Delta t \|\partial_t R\|_{0,0,\Gamma} + \|h \cdot \nabla R\|_{0,0,\Gamma} \ .$$

The theorem follows. □

## 5.4 Error Estimates for Arbitrary Discretisations

This section generalizes the results for the single layer potential without any assumptions on the underlying meshes.

**Lemma 20.** *Let $f_1, \ldots, f_n \in H^r(\mathbb{R}^+, H^s(\partial\Omega))$, $0 \leq s \leq 1$, $r \geq 0$, such that $f_j f_k = 0$ for $j \neq k$. Let $\omega_j$ be the interior of the support of $f_j$ with $\overline{\omega_j} = \text{supp } f_j$. Then*

$$\Big\| \sum_{j=1}^n f_j \Big\|_{r,s,\Gamma}^2 \leq \sum_{j=1}^n \|f_j\|_{r,s,\omega_j}^2 \ .$$

**Definition 21.** *We define $K(\Phi) = \max_j \text{card}\{k : \phi_k \phi_j \neq 0\}$.*

**Lemma 22.** *Let $\Phi$ be a finite partition of unity of $[0,T] \times \partial\Omega$ with overlap $K(\Phi)$. Then there exists a partition of $\{1, \ldots, M\}$ into $K \leq K(\Phi)$ non-empty subsets $M_1, \ldots, M_K$, such that $\bigcup_{j=1}^K M_j = \{M_1, \ldots, M\}$, $M_j \cap M_k = \emptyset$ if $j \neq k$ and for all $l \in \{1, \ldots, K\}$ and $j, k \in M_l$ with $j \neq k$, $\phi_j \phi_k = 0$ on $[0,T] \times \partial\Omega$.*

**Theorem 23.** *Let $\Gamma \subset \partial\Omega$ be connected. and let $\Phi$ be a finite partition of unity with*

*overlap* $K(\Phi)$. *Then for any* $f \in H^r(\mathbb{R}^+, H^s(\partial\Omega))$ *and any* $0 \le s \le 1$, *we have*

$$\|f\|^2_{r,s,\Gamma} \le K(\Phi) \sum_{j=1}^{M} \|f\phi_j\|^{2(1-s)}_{r,0,\Gamma} \|f\phi_j\|^{2s}_{r,1,\Gamma} \ .$$

*Proof.* We show

$$\|f\|^2_{r,s,\Gamma} \le K(\Phi) \sum_{j=1}^{M} \|f\phi_j\|^2_{r,s,\Gamma} \ . \tag{5.6}$$

The assertion then follows from the interpolation estimate

$$\|f\phi_j\|_{r,s,\Gamma} \lesssim \|f\phi_j\|^{1-s}_{r,0,\Gamma} \|f\phi_j\|^{s}_{r,1,\Gamma} \ .$$

To show (5.6), we consider a partition $M_1, \dots, M_K$ as in Lemma 22. Then $f = \sum_{j=1}^{M} \phi_j f$, so that

$$\|f\|^2_{r,s,\Gamma} \le \|f\|^2_{r,s,\partial\Omega} = \| \sum_{k=1}^{K} \sum_{j \in M_k} \phi_j f\|^2_{r,s,\partial\Omega} \le K \sum_{k=1}^{K} \| \sum_{j \in M_k} \phi_j f\|^2_{r,s,\partial\Omega} \ .$$

With Lemma 20,

$$\| \sum_{j \in M_k} \phi_j f\|^2_{r,s,\partial\Omega} \le \sum_{j \in M_k} \|\phi_j f\|^2_{r,s,\omega_j} \ ,$$

so that

$$\|f\|^2_{r,s,\Gamma} \le K \sum_{k=1}^{K} \sum_{j \in M_k} \|\phi_j f\|^2_{r,s,\omega_j} = K \sum_{j=1}^{M} \|\phi_j f\|^2_{r,s,\omega_j} \ ,$$

which shows (5.6). □

Together with Friedrichs inequality

$$\|f\phi_j\|_{r,1,\Gamma} \lesssim_\sigma \|\nabla(f\phi_j)\|_{r,0,\Gamma} + \|\partial_t(f\phi_j)\|_{r,0,\Gamma}$$

one obtains

$$\|f\phi_j\|^{1-s}_{r,0,\Gamma} \|f\phi_j\|^{s}_{r,1,\Gamma} \lesssim_\sigma d_j^{2(1-s)} (1 + d_j^2)^s (\|\nabla(f\phi_j)\|^2_{r,0,\Gamma} + \|\partial_t(f\phi_j)\|^2_{r,0,\Gamma}) \ .$$

Here $d_j$, the width of the support $\phi_j$, is defined as the smallest number such that the following is true: There exists a direction $n \in \mathbb{R}^3$, $|n| = 1$, such that for all $x \in \mathbb{R}^3$ and for

each plane $H$ perpendicular to $n$ with $x \in H$, the intersection $\operatorname{supp} \phi_j \cap H$ is a Lipschitz curve of length $\leq d_j$.

Our a posteriori error estimate therefore implies:

**Corollary 24.**

$$\|\psi - \psi_{h,\Delta t}\|^2 \lesssim C \sum_{j=1}^{N} \left( \|\nabla \mathcal{R}_{h,\Delta t}\|^2_{0,0,\Gamma_j} + \|\partial_t \mathcal{R}_{h,\Delta t}\|^2_{0,0,\Gamma_j} \right) .$$

## 5.5 Lower Bounds

Because of the different norms in the upper and lower bounds for $B_D$ in Proposition 17, the a posteriori estimate only satisfies a weak variant of efficiency: For $\varepsilon \in (0,1)$:

$$\max\{\Delta t, h\}^{-\frac{1-\varepsilon}{2}} \|\phi - \phi_{h,\Delta t}\|_{0,-\frac{1}{2},\Gamma} \lesssim$$
$$\|R\|_{0,1-\varepsilon,\Gamma} = \|\mathcal{V}(\dot{\phi} - \dot{\phi}_{h,\Delta t})\|_{0,1-\varepsilon,\Gamma} \lesssim \|\phi - \phi_{h,\Delta t}\|_{2,-\varepsilon,\Gamma} \leq \|\phi - \phi_{h,\Delta t}\|_{2,0,\Gamma} .$$

A proof of the sharp estimate, $\varepsilon = 0$, would require sharp mapping properties of the layer potentials outside the energy spaces and will be pursued elsewhere.

As in the elliptic case, we aim to use the mapping properties of $V$ together with approximation properties of the finite element spaces to recover the same spatial Sobolev index $-\frac{1}{2}$ in the upper and lower estimates.

**Theorem 25.** *Assume that the $R \in H^0([0,T], H^1(\Gamma))$ and that the ansatz functions $V^{p,q}_{h,\Delta t} \subseteq H^2([0,T], H^0(\Gamma))$ satisfy*

$$(\star) \qquad \inf_{\psi_{h\Delta t} \in V^{p,q}_{h,\Delta t}} \|\phi - \psi_{h\Delta t}\|_{2,0,\Gamma} \simeq \max\{h, \Delta t\}^{\beta}$$

*for some $\beta > 0$. Then for all $\varepsilon \in (0,1)$*

$$\|R\|_{0,1-\varepsilon,\Gamma} \lesssim \max\{h^{-\frac{1}{2}}, (\Delta t)^{-\frac{1}{2}}\} \|\phi - \phi_{h\Delta t}\|_{2,-1/2,\Gamma}.$$

Note that $V_{h,\Delta t}^{p,q} \subseteq H^2([0,T], H^0(\Gamma))$ is e.g. satisfied for cubic splines in time.

In Theorem 26 below, the hypothesis $(\star)$ is verified using the singular expansion of the solution $\phi$ at the edges and corners.

## 5.6 Best Approximation and Lower Bounds

In this section verify the hypothesis $(\star)$ in Theorem 25 for polyhedral domains, by proving upper and lower bounds for the best approximation of the solution to the wave equation with Dirichlet boundary conditions.

Let $\Omega$ be a polyhedral domain and $u$ a solution to the wave equation in $\Omega$:

$$\partial_t^2 u(t,x) - \Delta u(t,x) = 0 \qquad \text{in } \mathbb{R}_t^+ \times \Omega_x \ , \tag{5.7}$$

$$u(t,x) = g(t,x) \qquad \text{on } \Gamma = \partial\Omega \ , \tag{5.8}$$

$$u(0,x) = \partial_t u(0,x) = 0 \qquad \text{in } \Omega. \tag{5.9}$$

The function $u$ exhibits well-known singularities at non-smooth boundary points of the domain. Locally near an edge or a corner, $\Omega$ is of the form $\mathbb{R}_+ \times \mathcal{K}$, where the base $\mathcal{K} \subset S^2$ is a smooth or polygonal subset of the sphere. The solution may be decomposed into a leading part given by explicit singular functions plus less singular terms [61, 84, 85, 105]. We refer to [84, Theorem 7.4 and Remark 7.5] for details in the case of the Neumann problem in a wedge, respectively [85, Theorem 4.1] for the Dirichlet problem in a cone and state the decomposition in terms of polar coordinates $(r,\theta)$ centered at the vertex $(0,0,0)$:

$$\begin{aligned} u(t,x) = u_0(t,r,\theta) + \chi(r) r^\lambda a(t,\theta) + \tilde{\chi}(\theta) b_1(t,r) (\sin(\theta))^\nu \\ + \tilde{\chi}(\tfrac{\pi}{2} - \theta) b_2(t,r) (\cos(\theta))^\nu \ , \end{aligned} \tag{5.10}$$

$$\begin{aligned} \partial_n u(t,x) = \psi_0(t,r,\theta) + \chi(r) r^{\lambda-1} a(t,\theta) + \tilde{\chi}(\theta) b_1(t,r) r^{-1} (\sin(\theta))^{-\nu} \\ + \tilde{\chi}(\tfrac{\pi}{2} - \theta) b_2(t,r) r^{-1} (\cos(\theta))^{-\nu} \ . \end{aligned} \tag{5.11}$$

Here, $\nu = \frac{\pi}{\alpha}$, where $\alpha$ is the opening angle of the wedge, and $\lambda = -\frac{1}{2} + \sqrt{\frac{1}{4} + \mu}$, where $\mu$ is the smallest eigenvalue of the Laplace Beltrami operator with Dirichlet boundary

conditions in the subdomain $\mathcal{K}$ of the sphere. $\chi$, $\tilde{\chi}$ are cut-off functions and $a, b_j$ sufficiently regular. The functions $a, b_1, b_2$ are not identically 0 provided the corner is not in a trapped region and $T$ is sufficiently large.

From the representation formula, the wave equation translates into the boundary integral equation $V\phi = f$, with $f = (1 - K)g$ and solution $\phi = \partial_n u|_\Gamma$.

The main theorem concerning the approximation of $\phi$ is:

**Theorem 26.** *Assume that the coefficient functions $a, b_1, b_2$ are not identically 0. Then $E(\phi, h, \Delta t) \simeq \max\{h, \Delta t\}^{\max\{\nu-\frac{1}{2},\lambda\}}$.*

In particular, hypothesis $(\star)$ is satisfied. A similar result in the elliptic case was known if $\Gamma$ is a curve, i.e. in dimension 2 [27].

## 5.7 Algorithmic Details

The a posteriori error estimate from Theorem D leads to an adaptive mesh refinement procedure, based on the four steps:

$$\textbf{SOLVE} \longrightarrow \textbf{ESTIMATE} \longrightarrow \textbf{MARK} \longrightarrow \textbf{REFINE}.$$

The precise algorithm is given as follows:

**Adaptive Algorithm:**

Input: Spatial mesh $\mathcal{T} = \mathcal{T}_0$, refinement parameter $\theta \in (0, 1)$, tolerance $\epsilon > 0$, data $f$.

1. Solve $V\dot{\varphi}_{h,\Delta t} = \dot{f}$ on $\mathcal{T}$.
2. Compute the error indicators $\eta(\triangle)$ in each triangle $\triangle \in \mathcal{T}$.
3. Find $\eta_{\max} = \max_{\triangle} \eta(\triangle)$.
4. Stop if $\sum_i \eta^2(\triangle_i) < \epsilon^2$.
5. Mark all $\triangle \in \mathcal{T}$ with $\eta(\triangle_i) > \theta\eta_{\max}$.

6. Refine each marked triangle into 4 new triangles to obtain a new mesh $\mathcal{T}$ (and project the new nodes onto the sphere). Choose $\Delta t$ such that $\frac{\Delta t}{\Delta x} \leq 1$ for all triangles.

7. Go to 1.

Output: Approximation of $\dot{\varphi}$.

In the first step, we solve $V\dot{\varphi} = \dot{f}$ using the Galerkin discretisation (5.5) in $V_{h,\Delta t}^{1,1}$. The Galerkin solution has the form

$$\dot{\varphi}_{h,\Delta t}(x,t) = \sum_{m=1}^{N_t} \sum_{i=1}^{N_s} \varphi_i^m \beta^m(t) \xi_i(x) \ ,$$

where $\beta^m$ is the piecewise linear hat function in time associated to time $t_m$,

$$\beta^m(t) = (\Delta t)^{-1}((t - t_m)\chi_{[t_{m-1},t_m]}(t) - (t - t_{m+1})\chi_{[t_m,t_{m+1}]}(t)),$$

and $\xi_i$ is the piecewise linear hat function in space associated to node $i$.

As a step towards adaptive mesh refinements in space-time, we here focus on time-integrated error indicators as they are relevant for geometric singularities. As shown in Chapter 4 and [61], for polyhedral meshes and screens time-independent graded meshes lead to quasi-optimal convergence rates in spite of singularities of the solutions. The time-integrated error indicator for triangle $\triangle$ is computed as

$$\eta^2(\triangle) = \textstyle\sum_n \eta_{\triangle,\nabla_\Gamma}(I_n)^2 + \eta_{\triangle,\partial_t}(I_n)^2 \ .$$

Here, for every triangle $\triangle$ and every time interval $I_n = [t_{n-1}, t_n]$ we define the partial error indicators

$$\eta_{\triangle,\nabla_\Gamma}(I_n)^2 = h_\triangle \int_{t_{n-1}}^{t_n} \int_\triangle [\nabla_\Gamma(\dot{f} - V\dot{\varphi}_{h,\Delta t})]^2 ds_x dt \,,$$
$$\eta_{\triangle,\partial_t}(I_n)^2 = \Delta t \int_{t_{n-1}}^{t_n} \int_\triangle [\partial_t(\dot{f} - V\dot{\varphi}_{h,\Delta t})]^2 ds_x dt \,.$$

The time integral is approximated by the trapezoidal rule, and the tangential gradient of

a function $F$ is computed as

$$\nabla_\Gamma F(t,x) = P_\Gamma \nabla F = \nabla F(t,x) - \nu(\nu \cdot \nabla F(t,x))$$

with the outer unit normal vector $\nu$ to $\Gamma$, resp. the projection $P_\Gamma$ onto the tangent bundle of $\Gamma$.

To compute $\eta_{\triangle,\nabla_\Gamma}$ from $\dot{\varphi}_{h,\Delta t}$, we consider the gradient of $V\dot{\varphi}_{h,\Delta t}$ as a singular integral:

$$\begin{aligned}
&\nabla_\Gamma V\dot{\varphi}_{h,\Delta t}(t,x) \\
&= \frac{-1}{4\pi} P_\Gamma \int_\Gamma (x-y) \left( \frac{\dot{\varphi}_{h,\Delta t}(t-|x-y|,y)}{|x-y|^3} + \frac{\ddot{\varphi}_{h,\Delta t}(t-|x-y|,y)}{|x-y|^2} \right) ds_y \\
&= \frac{-1}{4\pi} \sum_{m=1}^{N_t} \sum_{i=1}^{N_s} \varphi_i^m P_\Gamma \int_\Gamma \varphi_i(y) \left[ \beta^m(t-|x-y|) \frac{x-y}{|x-y|^3} + \dot{\beta}^m(t-|x-y|) \frac{x-y}{|x-y|^2} \right] ds_y.
\end{aligned}$$

Using the explicit form of $\beta^m$, we obtain

$$\begin{aligned}
\nabla_\Gamma V\dot{\varphi}_{h,\Delta t}(t,x) = \frac{-1}{4\pi} \sum_{m=1}^{N_t} \sum_{i=1}^{N_s} \varphi_i^m \Bigg[ &\frac{t-t_{m-1}}{\triangle t} P_\Gamma \int_{t-t_m \le |x-y| \le t-t_{m-1}} \xi_i(y) \frac{x-y}{|x-y|^3} ds_y \\
&- \frac{t-t_{m+1}}{\triangle t} P_\Gamma \int_{t-t_{m+1} \le |x-y| \le t-t_m} \xi_i(y) \frac{x-y}{|x-y|^3} ds_y \Bigg].
\end{aligned}$$

The integrals are evaluated with a composite hp-graded quadrature, like the entries of the BEM matrix in (5.5). See [54] for details.

## 5.8 Numerical Experiments

**Example 1:** We consider the Dirichlet problem $V\phi = f$ on $\Gamma = S^2$ with the right hand side $f(t,x,y,z) = \sin(t)^5 x^2$ and $[0,T] = [0,2.5]$. We use a discretisation by linear ansatz and test functions in space and time. $\Gamma$ is approximated by uniform meshes of 320,1280, and 5120 triangles, with time step $\Delta t$ is 0.2, 0.1, resp. 0.05 for the respective meshes to keep $\frac{\Delta t}{h}$ fixed. The numerical results are compared to the exact solution, which can be found using the methods from [121].

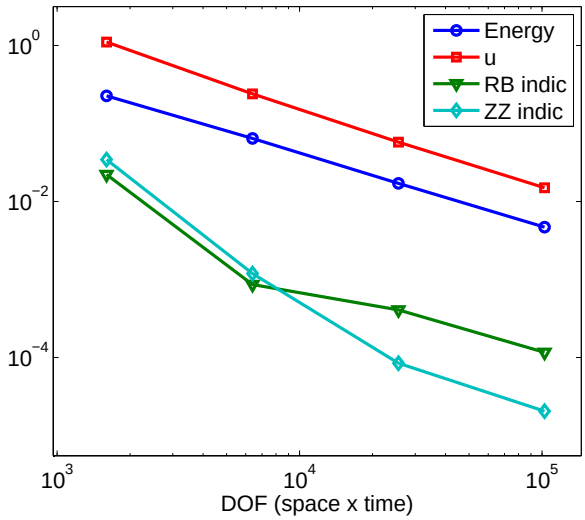


Figure 5.1: Energy error, residual and ZZ error indicators for Dirichlet problem on $\Gamma = S^2$, Example 1.

Figure 5.1 shows the convergence of the error $\phi - \phi_{h,\Delta t}$ in energy ($E = \frac{1}{2}c^T Vc - Fc$) as well as the $L^2$ error in the sound pressure and compares them to the residual and ZZ error indicators. The convergence rates are all comparable: We obtain a convergence rate of 0.93 in energy, 0.97 in sound pressure, 0.9 in the residual error indicator, and 1.02 in the ZZ indicator. This illustrates the reliability and efficiency of both error indicators with respect to energy and related quatities such as the sound pressure in an example with a known exact solution.

The similar slopes of the energy norm and the residual error indicator corroborate the efficiency of the residual a posteriori error estimate. More precisely, the quotient of the error estimate and the energy error, the efficiency index, remains approximately constant at 0.025 as the number of degrees of freedom increases.

**Example 2:** We consider the Dirichlet problem $V\phi = f$ on the square screen $\Gamma = [-0.5, 0.5]^2 \times \{0\}$ with the right hand side $f(t, x, y, z) = \sin(t)^5 x^2$ for times $[0, 2.5]$. Using a discretisation by linear ansatz and test functions in space and time, we compare the error of a uniform discetization to the error of an adaptive series of meshes, steered by the residual error estimate. The time step is fixed at $\Delta t = 0.1$, and the uniform meshes consist of 18, 288, 648, 1352, and 6050 triangles, while the adaptive refinements correspond

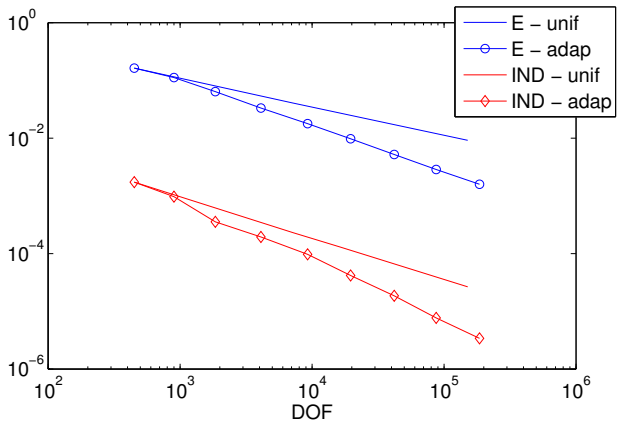


Figure 5.2: Energy error and residual error indicators for Dirichlet problem on $\Gamma = [-0.5, 0.5]^2 \times \{0\}$, Example 2.

to 36, 74, 164, 370, 784, 1676, 3485, and 7432 triangles.

Figure 5.2 shows the convergence of the error indicator and the error in energy, for both the uniform and adaptive series of meshes. The convergence rate is approximately 0.48 for uniform refinements, compared to 0.77 for adaptive refinements. The convergence rate in the uniform case agrees with the theoretical prediction of 0.5 from Chapter 4 (Corollary B, where $\beta = 1$ for a uniform mesh) and [61]. The adaptive convergence rate of 0.77 recovers the results for time-independent screen problems [30].

As in the elliptic case, the convergence rate of the adaptive refinements does not reach the optimal rate of 1.5 achieved with algebraically graded meshes, as demonstrated in [61]. The anisotropic graded meshes cannot be obtained by mesh refinements: While adaptive meshes are locally quasi-uniform, graded meshes involve arbitrarily thin triangles with shallow angles near the edge of the screen. A heuristic explanation for the substantially higher rates of (anisotropic) graded meshes is contained in [31].

Figure 5.3 shows representative adaptive meshes, where the colour scale highlights the residual-based indicator values for each element. Mesh refinements concentrate at the left and right edges, where the right hand side is steep, and to a lesser extent also at the top and bottom edges.

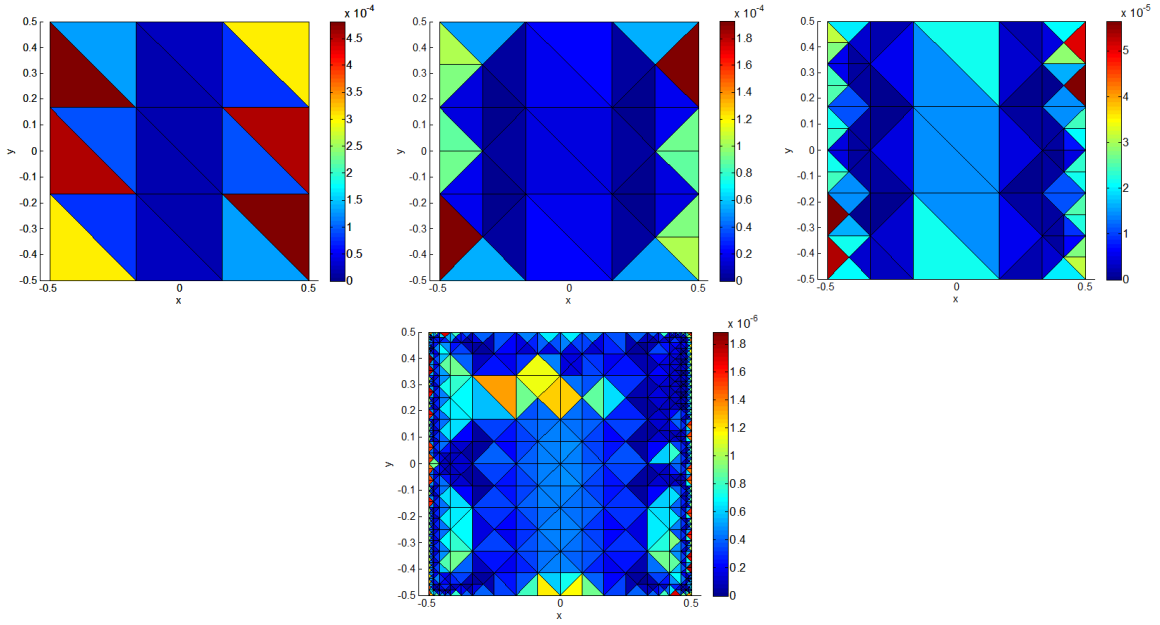

Figure 5.3: Meshes 1, 2, 3 and 6 generated by adaptive refinements, Example 2.

**Example 3:** We consider the Dirichlet problem $V\phi = f$ on an isosceles, right-angled triangle $\Gamma$ depicted in Figure 5.5. The right hand side is given by $f(t, x, y, z) = \sin(t)^5$, and we consider times $[0, 2.5]$. Using the discretisation from Example 2, we compare the error on uniform meshes to the error of an adaptive series of meshes, steered by the residual error estimate. The time step is fixed at $\Delta t = 0.1$.

Figure 5.4 shows the convergence of the error indicator and the error in the energy norm, for both the uniform and adaptive series of meshes. The convergence rate is approximately 0.49 for uniform refinements, compared to 0.78 for adaptive refinements, almost identical to the square screen in Example 2.

Figure 5.5 shows representative adaptive meshes, where the colour scale highlights the residual-based indicator values for each element. As expected, mesh refinements concentrate in the two sharper corners of the triangle.

**Example 4:** We consider the Dirichlet problem $V\phi = f$ on the triangle $\Gamma$ with angles of 30, 60 and 90 degrees, as depicted in Figure 5.7. The right hand side is given by $f(t, x, y, z) = \sin(t)^5$, and we consider times $[0, 2.5]$. Using the discretisation from Example 2, we compare the error on uniform meshes to the error of an adaptive series of

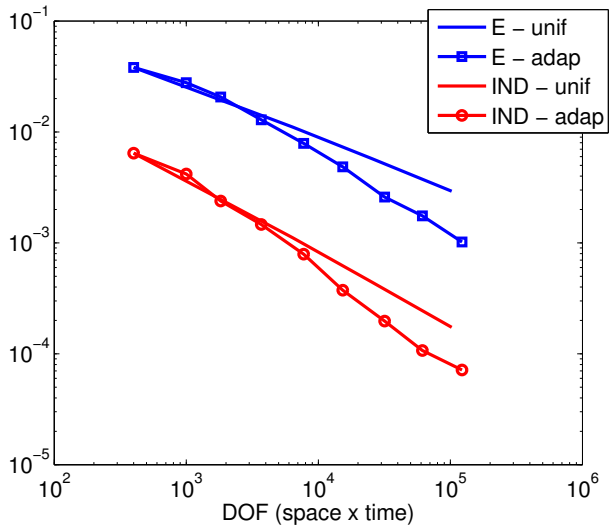


Figure 5.4: Energy error and residual error indicators for Dirichlet problem isosceles triangle, Example 3.

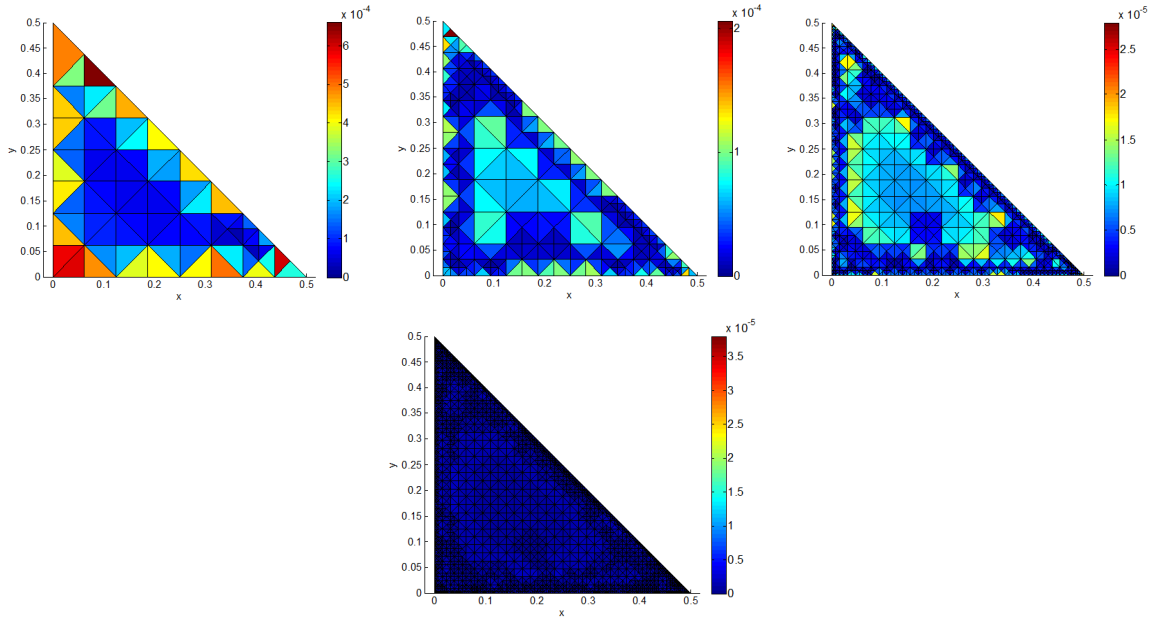

Figure 5.5: Meshes 3, 5, 7 and 8 generated by adaptive refinements, Example 3.

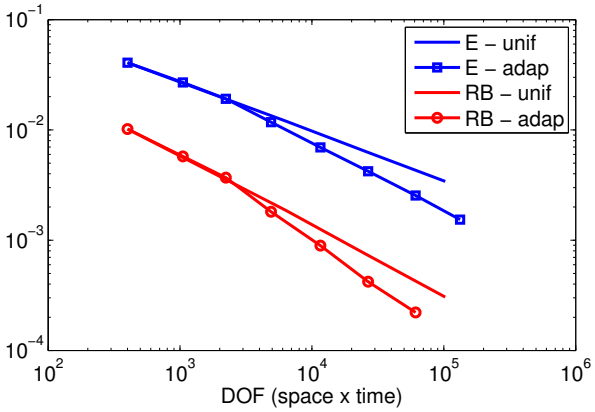


Figure 5.6: Energy error and residual error indicators for Dirichlet problem on 30-60-90 triangle, Example 4.

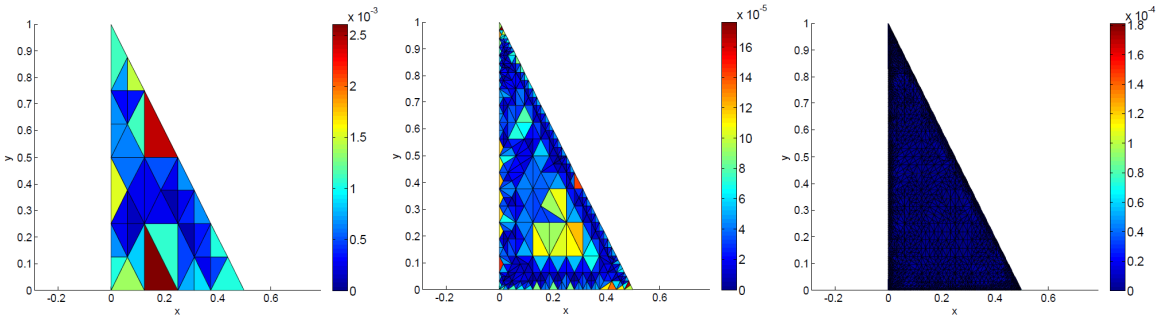

Figure 5.7: Meshes 2, 5, 8 generated by adaptive refinements, Example 4.

meshes, steered by the residual error estimate. The time step is fixed at $\Delta t = 0.1$.

Figure 5.6 shows the convergence of the error indicator and the error in the energy norm, for both the uniform and adaptive series of meshes. The convergence rate is approximately 0.448 for uniform refinements, compared to 0.65 for adaptive refinements. The rates are slightly reduced compared to Examples 2 and 3, possibly because the asymptotic regime only sets in for higher degrees of freedom because of the small angles of 30 degrees in the triangulation.

Figure 5.7 shows representative adaptive meshes, where the colour scale highlights the residual-based indicator values for each element. As expected, mesh refinements concentrate in the corners according to their sharpness.

From Experiments 2, 3 and 4 we conclude that the convergence rate does not depend on the angles of the triangle, and therefore the corner singularity. The convergence rate of

around $\frac{1}{2}$ on uniform meshes matches the rate theoretically expected for the approximation of the edge singularity [61], while the approximation error from the corner singularities is of higher order. The adaptive convergence rates of around 0.78 are compatible with the convergence rates of around 0.8 for the time-independent Laplace equation in [30]. The rates are slightly reduced in Example 4, with angles of 30 degrees, possibly because of the necessarily thin triangles in the triangulation.

## 5.9 Towards Space-Time Adaptivity

### 5.9.1 Motivation

The previous sections presented an adaptive mesh refinement procedure based on time-independent meshes. While these provide efficient approximations for solutions with time-independent, geometric singularities, wave phenomena naturally include singularities which move in space-time, such as travelling wave crests.

The time-averaged error indicators used above are inadequate in such settings. However, the underlying a posteriori error estimates still apply and can be used to define residual error indicators in each space-time element. In a first step, we here show some preliminary explorations for space-time refinements based on ZZ indicators.

The following images illustrate a space-time refinement upon one of the simplest possible space-time meshes. We consider $\mathbb{R} \times \mathbb{R}$ space-time, so that we can easily display the space-time mesh on paper, although this is easily generalised to $n$ spatial dimensions.

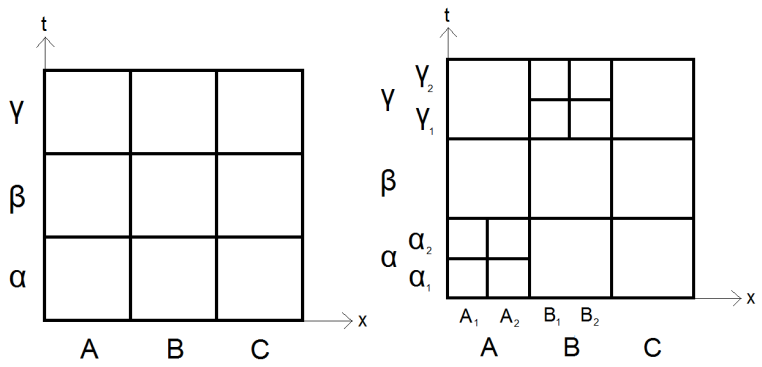


Figure 5.8: Test case in $\mathbb{R} \times \mathbb{R}$. left: original coarse mesh, right: a first space-time refinement.

The leftmost image shows a coarse, uniform 3 by 3 space-time mesh, and on the right this has been refined once in space-time at the bottom-left and top-centre locations. We refine in both space and time this way in order to keep the CFL number fixed locally.

Every box in the image represents a space-time basis function. Greek letters index the individual nodes on the time interval, and Latin letters index the spatial nodes on the mesh. This example shows a space-time mesh which has two refinement-layers (in both space and time). Further refinements would increase the number of layers.

$\alpha$ represents a $p = 1$ hat function spanning a certain $\Delta t$ and $\alpha_1, \alpha_2$ represent two $p = 1$ hat functions in time which each have the reduced discretisation parameter $\frac{\Delta t}{2}$, so as to fill the same space on the time interval. Similarly in space, $A$ represents a spatial basis function and $A_1, A_2$ represents two spatial basis functions whose support is the same space as $A$.

There are 9 $\mathbb{R} \times \mathbb{R}$ space-time basis functions represented by the coarse mesh (left), which are: $\alpha A$, $\alpha B$, $\alpha C$, $\beta A$, $\beta B$, $\beta C$, $\gamma A$, $\gamma B$, $\gamma C$.

There are 15 $\mathbb{R} \times \mathbb{R}$ space-time basis functions represented by the refined mesh (right), which are: $\alpha_1 A_1$, $\alpha_1 A_2$, $\alpha_2 A_1$, $\alpha_2 A_2$ , $\alpha B$, $\alpha C$, $\beta A$, $\beta B$, $\beta C$, $\gamma A$, $\gamma_1 B_1$, $\gamma_1 B_2$, $\gamma_2 B_1$, $\gamma_2 B_2$, $\gamma C$.

Note that the refinement process has introduced 4 extra spatial nodes and 4 extra temporal nodes into the geometry.

Further refinements could be made to the mesh from this point on, which would introduce more layers than the two shown here. We need an efficient way of keeping track of such things, and all the other relevant data contained in this mesh.

### 5.9.2 Aliasing

The uniform and space-only adaptive methods required the population of a block-banded space-time Galerkin matrix. The bands were composed of repeating the same block down the band. This meant that only one block needed to be computed for every temporal basis function. We now no longer have this banded structure to exploit in this way.

There is now a degree of independence between the blocks in a band.

In some cases, such as when only a few refinements have been made (relative to the size of the space-time mesh), we have a lot of similarity and we can say that the mesh exhibits only a small degree of independence. Such a mesh will allow (at least partially) repeating blocks to be populated down a time-block band.

Alternatively, if there have been many refinements made, and at different depths of refinement, a space-time mesh will exhibit a much higher degree of independence. Each space-time block will be unique or close to unique.

Due to the added power of a refinement in space-time rather than space alone, we plan on making refinements in such a way that we remain in the low-independence regime (few refinements relative to mesh size). In order to take advantage of the dependence in the first set of cases, we introduce the idea of aliasing.

We have identified the criteria by which matrix entries $\alpha$ and $\beta$ have the same entry. The entries are the same if and only if:

Firstly, the time discretisation parameter must be the same. This requires that $\Delta t_\alpha = \Delta t_\beta$.

Secondly, the difference $n - m$ must be the same. i.e. $n_\alpha - m_\alpha = n_\beta - m_\beta$, where $n, m$ index the time step of the temporal test and ansatz functions repectively.

Thirdly, the spatial node associated to $\alpha$ and $\beta$ must be the same.

The image below shows the full space-time matrix arranged into its time blocks. We have highlighted 3 bands of the matrix in the various colours. In each band, both our criteria are satisfied. Depending on the level of dependence that exists in space-time, some of the information in each band will be repeated further down the band in different blocks. For efficiency, we wish to avoid re-calculating such matrix entries.

On the right, we take a closer look at one of the bands - it contains 8 blocks which we number from 0 to 7. Block 0 is refered to as the master block. All entries in master blocks are computed.

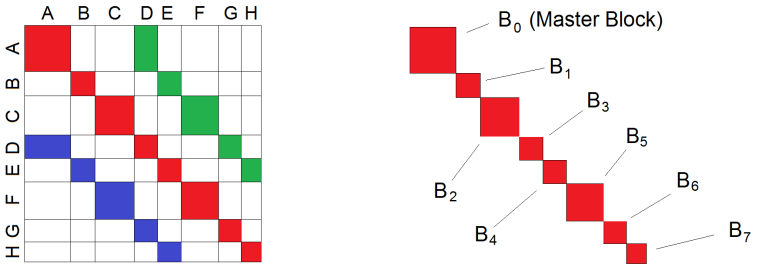


Figure 5.9: The full space-time matrix and its new bands.

Before the computation of the full space-time matrix is started, we run our aliasing algorithm. This consists of going through each block in the matrix (apart from the master blocks), then each entry in the block, and for each entry we check every other entry further back in the band to see if the third criteria (same spatial node) is satisfied in both entries. If a match is found, we store the row and column of the earlier entry. This is to mark it so that we only calculate the entry once.

Although the computation cost can be quite large (the worst case being quadratic time complexity, like the matrix computation), this process is much faster than computing the matrix entries.

### 5.9.3 Space-Time Adaptive Algorithm

**Space-Time Adaptive Algorithm:**

Input: Spatial mesh $\mathcal{T} = \mathcal{T}_0$, refinement parameter $\theta \in (0, 1)$, tolerance $\epsilon > 0$, data $f$.

1. Solve $V\dot{\varphi}_{h,\Delta t} = \dot{f}$ on $\mathcal{T}$.
2. Compute the error indicators $\eta(t, \triangle)$ in each triangle $\triangle \in \mathcal{T}$, and at each time step $t_j \in [0, T]$.
3. Find $\eta_{\max} = \max_{t_j, \triangle} \eta(t_j, \triangle)$.
4. Stop if $\sum_{i,j} \eta^2(t_j, \triangle_i) < \epsilon^2$.
5. Mark all $\triangle \in \mathcal{T}$ with $\eta(t, \triangle_i) > \theta\eta_{\max}$.
6. Refine each marked triangle into 4 new triangles to obtain a new mesh $\mathcal{T}$
7. Go to 1.

Output: Approximation of $\dot{\varphi}$.

### 5.9.4 Preliminary Results

We consider a sinusoidal travelling wave front, with the solution depicted in Figure 5.10. It shows the time evolution of this wave as it approaches the mesh from the lower right at $t = 0$, ending at around the centre of the mesh at $t = 2.5$. Figure 5.11 and 5.12 show the first refinements when applying space-time adaptive method. One can see the refinements tracking the travelling wave from outside the bottom-right corner of the mesh to about centre.

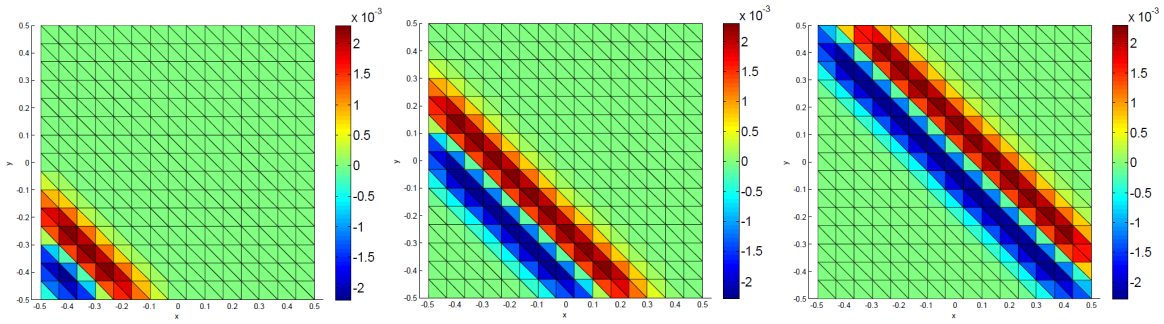

Figure 5.10: Density $\phi$, for a travelling wave at $t = 0.5, 1.0, 2.5$.

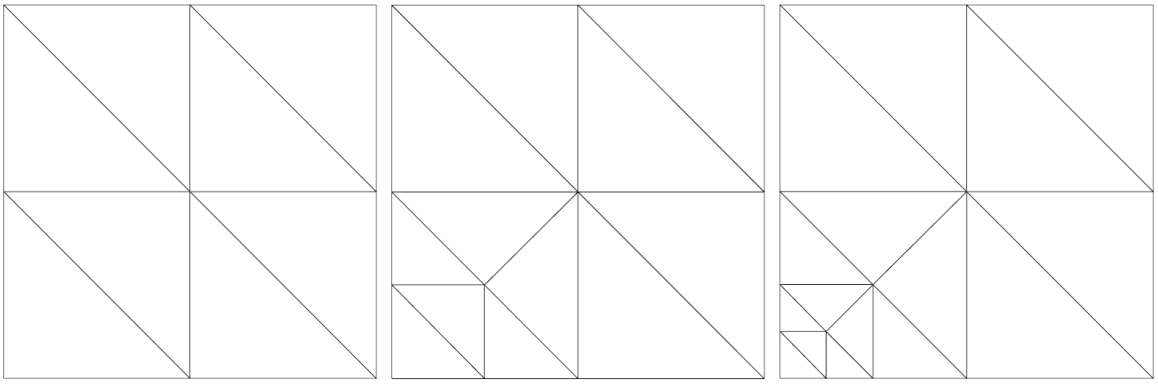

Figure 5.11: Meshes 1, 2, 3 generated by space-time adaptive refinements, relating to $t = 0.1, 0.3, 0.5$.

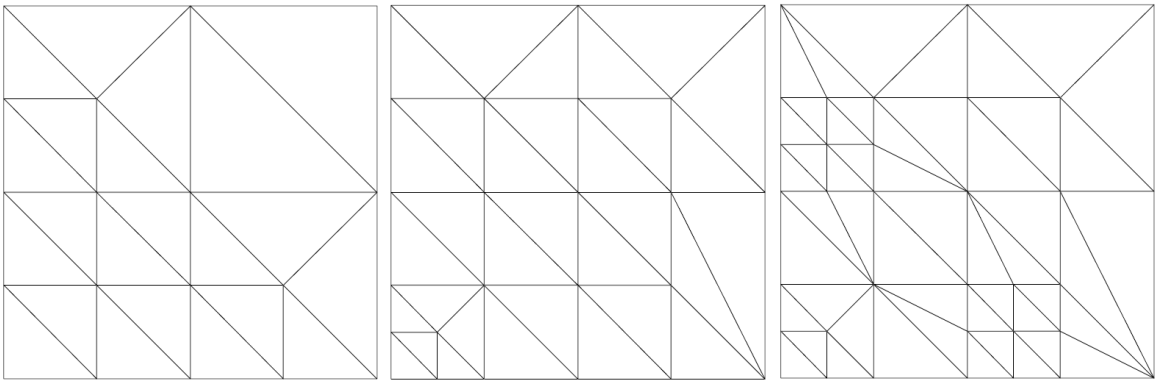

Figure 5.12: Meshes 4, 5, 6 generated by space-time adaptive refinements, relating to $t = 1.2, 2.3, 2.5$.

# Chapter 6

# Space-Time $p$-Methods

This chapter is based on joint work [63] with H. Gimperlein and E.P. Stephan.

## 6.1 Introduction

In previous chapters we have focused on $h$-versions of the time-domain boundary method, where the degree $p$ of the elements is fixed and convergence to an exact solution is obtained by mesh refinements. For time independent problems also $p$-versions of the boundary element method have been considered, going back to [9, 116]. For the $p$-version one considers a fixed mesh and increases the accuracy of the solution by increasing the degree $p$ of the elements. The analogous approach for finite elements was first investigated by Babuska and his students [13, 14, 43, 44]. See [112] for a comprehensive discussion of analysis in the time-independent case. More recent optimal convergence results for boundary elements on screens have been obtained, for example, in [24, 25, 78].

In this chapter we introduce a space-time $p$-version of the time domain boundary element method. Similar to the time-independent case, we fix a coarse space-time mesh and obtain convergence by increasing the polynomial degree $p$ in space and time.

To be specific, for a polyhedral screen $\Gamma \subset \mathbb{R}^3$ with connected complement $\Omega = \mathbb{R}^3 \setminus \overline{\Gamma}$

this chapter considers the wave equation

$$c^{-2}\partial_t^2 u(t,x) - \Delta u(t,x) = 0 \quad \text{in } \mathbb{R}_t^+ \times \Omega_x \tag{6.1a}$$

$$Bu = g \quad \text{on } \Gamma = \partial\Omega \tag{6.1b}$$

$$u(0,x) = \partial_t u(0,x) = 0 \quad \text{in } \Omega\ . \tag{6.1c}$$

As before, we choose units such that $c = 1$ and consider either Dirichlet ($Bu = u$) or Neumann boundary conditions ($Bu = \partial_n u$) on $\Gamma$.

Similar to the analysis of the $h$-version on graded meshes, the singularities of the solution have implications for the approximation rate of $p$-version time domain boundary elements. Based on the asymptotic expansion of the solution $u$ and its normal derivative on $\Gamma$, we obtain sharp convergence rates on polyhedral domains and screens.

We formulate (6.1) as a time dependent integral equation on $\Gamma$ for the single layer or double layer operator. The Dirichlet trace $u|_\Gamma$ is approximated by tensor products of piecewise polynomial functions $\widetilde{V}_{\Delta t,h}^{p,q}$ on a fixed mesh in space and a uniform mesh in time of step size $\Delta t$. Our main result for the approximation of the solutions to the boundary integral equations in space-time anisotropic Sobolev spaces is a consequence of:

**Theorem E.** *Let* $\varepsilon > 0$.

*a) Let $u$ be a strong solution to the homogeneous wave equation with inhomogeneous Neumann boundary conditions $\partial_n u|_\Gamma = g$, with $g$ smooth. Further, let $\phi_{h,\Delta t}^\beta$ be the best approximation in the norm of $H_\sigma^r(\mathbb{R}^+, \widetilde{H}^{\frac{1}{2}-s}(\Gamma))$ to the Dirichlet trace $u|_\Gamma$ in $\widetilde{V}_{\Delta t,h}^{p,1}$.* Then $\|u - \phi_{h,\Delta t}^\beta\|_{r,\frac{1}{2}-s,\Gamma,*} \leq C_{\beta,\varepsilon} p^{-1-2s+\varepsilon}$, where $s \in [0, \frac{1}{2}]$ and $r \in [0, p)$.

*b) Let $u$ be a strong solution to the homogeneous wave equation with inhomogeneous Dirichlet boundary conditions $u|_\Gamma = g$, with $g$ smooth. Further, let $\psi_{h,\Delta t}^\beta$ be the best approximation in the norm of $H_\sigma^r(\mathbb{R}^+, \widetilde{H}^{-\frac{1}{2}}(\Gamma))$ to the Neumann trace $\partial_n u|_\Gamma$ in $V_{\Delta t,h}^{p,0}$.* Then $\|\partial_n u - \psi_{h,\Delta t}^\beta\|_{r,-\frac{1}{2},\Gamma,*} \leq C_{\beta,\varepsilon} p^{-1+\varepsilon}$, where $r \in [0, p+1)$.

It implies an approximation result for the solution to the boundary integral formulations:

**Corollary F.** *Let $\varepsilon > 0$.*

*a) Let $\phi$ be the solution to the hypersingular integral equation $W\phi = g$ and $\phi^{\beta}_{h,\Delta t}$ the best approximation in the norm of $H^r_\sigma(\mathbb{R}^+, \widetilde{H}^{\frac{1}{2}-s}(\Gamma))$ to $\phi$ in $\widetilde{V}^{p,1}_{\Delta t,h}$. Then $\|\phi - \phi^{\beta}_{h,\Delta t}\|_{r,\frac{1}{2}-s,\Gamma,*} \leq C_{\beta,\varepsilon} p^{-1-2s+\varepsilon}$, where $s \in [0, \frac{1}{2}]$ and $r \in [0, p)$.*

*b) Let $\psi$ be the solution to the single layer integral equation $V\psi = f$ and $\psi^{\beta}_{h,\Delta t}$ the best approximation in the norm of $H^r_\sigma(\mathbb{R}^+, \widetilde{H}^{-\frac{1}{2}}(\Gamma))$ to $\psi$ in $V^{p,0}_{\Delta t,h}$. Then $\|\psi - \psi^{\beta}_{h,\Delta t}\|_{r,-\frac{1}{2},\Gamma,*} \leq C_{\beta,\varepsilon} p^{-1+\varepsilon}$, where $r \in [0, p+1)$.*

Indeed, on the flat screen the solutions to the integral equations are given by $\phi = [u]\,|_\Gamma$ in terms of the solution $u$ which satisfies Neumann conditions $Bu = \partial_n u|_\Gamma = g$, respectively $\psi = [\partial_n u]\,|_\Gamma$ in terms of the solution $u$ which satisfies Dirichlet conditions $Bu = u|_\Gamma = f$.

The proofs of Theorem E and Corollary F closely relate to the proofs of the corresponding results for graded meshes. They can be found in [63]. This reference also contains results for polyhedral domains, similar to [44] in the time-independent case.

Numerical experiments confirm the theoretical results for the singular exponents and achieve the predicted convergence rates for the Dirichlet problem on a square screen. The convergence rate in the energy norm is doubled compared to the convergence rate of the $h$-version on a uniform mesh. Numerical experiments on the icosahedron confirm the faster convergence of the $p$-method compared to the $h$-method.

## 6.2 Discretisation

For the time discretisation we consider a uniform decomposition of the time interval $[0, \infty)$ into subintervals $[t_{n-1}, t_n)$ with time step $\Delta t$, such that $t_n = n\Delta t$ $(n = 0, 1, \dots)$.

In $\mathbb{R}^3$, we may assume that $\Gamma$ consists of closed triangular faces $\Gamma_i$ such that $\Gamma = \cup_i \Gamma_i$. In $\mathbb{R}^2$, $\Gamma = \cup_i \Gamma_i$ is partitioned into line segments $\Gamma_i$.

We choose a basis $\{\xi^1_h, \cdots, \xi^{N_s}_h\}$ of the space $V^q_h(\Gamma)$ of piecewise polynomial functions of degree $q$ in space. Moreover we define $\widetilde{V}^q_h(\Gamma)$ as the space $V^q_h(\Gamma)$, where the polynomials

vanish on $\partial\Gamma$ for $q \geq 1$. For the time discretisation we choose a basis $\{\beta^1_{\Delta t}, \cdots, \beta^{N_t}_{\Delta t}\}$ of the space $V^p_t$ of piecewise polynomial functions of degree of $p$ in time (continuous and vanishing at $t = 0$ if $p \geq 1$).
Let $\mathcal{T}_S = \{\Delta_1, \cdots, \Delta_N\}$ be a quasi-uniform triangulation of $\Gamma$ and $\mathcal{T}_T = \{[0, t_1), [t_1, t_2), \cdots, [t_{M-1}, T)\}$ the time mesh for a finite subinterval $[0, T)$.

We consider the tensor product of the approximation spaces in space and time, $V^q_h$ and $V^p_{\Delta t}$, associated to the space-time mesh $\mathcal{T}_{S,T} = \mathcal{T}_S \times \mathcal{T}_T$, and we write

$$V^{p,q}_{\Delta t,h} := V^p_{\Delta t} \otimes V^q_h \ . \tag{6.2}$$

We analogously define

$$\tilde{V}^{p,q}_{\Delta t,h} := V^p_{\Delta t} \otimes \tilde{V}^q_h \ . \tag{6.3}$$

The Galerkin discretisation of the Dirichlet problem is then given by:

Find $\psi_{\Delta t,h} \in V^{p,q}_{\Delta t,h}$ such that for all $\Psi_{\Delta t,h} \in V^{p,q}_{\Delta t,h}$

$$\int_0^\infty \int_\Gamma (V\psi_{\Delta t,h}(t,\mathbf{x}))\partial_t \Psi_{\Delta t,h}(t,\mathbf{x}) \ ds_x \ d_\sigma t = \int_0^\infty \int_\Gamma f(t,\mathbf{x})\partial_t \Psi_{\Delta t,h}(t,\mathbf{x}) \ ds_x \ d_\sigma t \ . \tag{6.4}$$

For the Neumann problem, we have:

Find $\phi_{\Delta t,h} \in \widetilde{V}^{p,q}_{t,h}$ such that for all $\Phi_{\Delta t,h} \in \widetilde{V}^{p,q}_{t,h}$

$$\int_0^\infty \int_\Gamma (W\phi_{\Delta t,h}(t,\mathbf{x}))\partial_t \Phi_{\Delta t,h}(t,\mathbf{x}) \ ds_x \ d_\sigma t = \int_0^\infty \int_\Gamma g(t,\mathbf{x})\partial_t \Phi_{\Delta t,h}(t,\mathbf{x}) \ ds_x \ d_\sigma t \ . \tag{6.5}$$

From the weak coercivity of $V$, respectively $W$, the discretized problems (6.4) and (6.5) admit unique solutions.

## 6.3 Algorithmic Details

### 6.3.1 Spatial Elements

Figure 6.1 shows the locations of the local nodes as we increase $p$. These are known as Lagrange nodes, since Lagrange interpolation is used here.

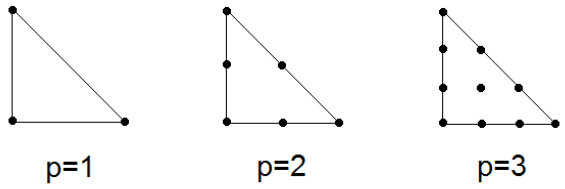


Figure 6.1: Local nodes for $p = 1, 2, 3$.

Starting with the cubic basis ($p = 3$) and higher, we have our first occurance of a local node which is completely inside an element. We refer to such nodes as 'bubble nodes' and their corrresponding local basis function as a 'bubble function'.

We can calculate the number of local nodes from $p$, by using the Equation (6.6):

$$\text{local DOF} := \frac{p^2 + 3p + 2}{2} \tag{6.6}$$

We also note that there are $p + 1$ nodes on each element edge. This information along with the above formula allows us to easily work out the coordinates of each Lagrange node in the reference triangle. When applied to the full spatial mesh, we have nodes as in Figure 6.2.

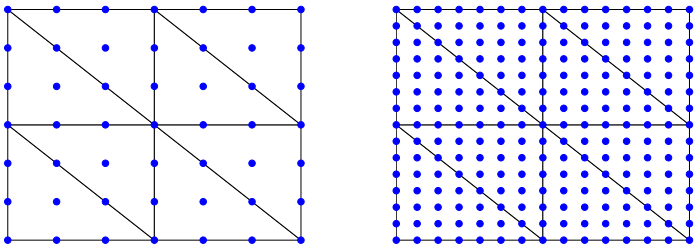

Figure 6.2: Lagrange nodes for polynomial degree $p = 3$ (left) and $p = 7$ (right).

The general formula for a $p = n$ basis function, where $p > 2$ is:

$$\phi := \underbrace{c_0}_{p=0} + \underbrace{c_1 x + c_2 y}_{p=1} + \underbrace{c_3 x^2 + c_4 y^2 + c_5 xy}_{p=2} + \dots \tag{6.7}$$

where we have grouped the formula into new terms for each added degree, so that it becomes clear to see how this generalises for any higher $p$.

The coefficients for any $p$ can be calculated by solving a simple linear system of equations.

On the RHS, we have something very similar to what is discussed here in this section for the matrix. Each entry in the RHS vector represents a global basis function, and we integrate over its support.

### 6.3.2 Temporal Elements

As we increase $p$ in time, the number of bubble functions present in a given sub-interval increases, since more nodes are required in the sub-interval to fix higher-$p$ functions. For cubic functions ($p = 3$) we require two extra nodes in the interval $[t_n - \Delta t, t_n]$ at $t_n - \frac{2\Delta t}{3}$ and $t_n - \frac{\Delta t}{3}$.

The generalised temporal basis functions for order $p$ have the form:

$$\phi := c_0 + c_1 t + c_2 t^2 + c_3 t^3 + c_4 t^4 + ... + c_{p+1} t^p \tag{6.8}$$

To calculate the coefficients, we also use the linear system method discussed in the spatial section (Lagrange interpolation). There are fewer coefficients in one dimension - other than this the method is very similar.

We make use of the reference interval [0,1] discussed earlier. That is to say that we choose our temporal nodes in [0,1] and use a simple linear transformation to project to other areas of the full time interval. We do this so that our basis functions (which are calculated for this reference element) can be used many times without having to keep solving the above-mentioned linear system at every time system, to get new coefficients.

If we wish to project a function from the reference interval $[0, 1]$ to $[\alpha, \alpha + \Delta t]$ we only need to consider the following polynomial where the coefficients are the same as before:

$$\phi := c_0 + c_1 \left( \frac{t - \alpha}{\Delta t} \right) + c_2 \left( \frac{t - \alpha}{\Delta t} \right)^2 + c_3 \left( \frac{t - \alpha}{\Delta t} \right)^3 + ... + c_{p+1} \left( \frac{t - \alpha}{\Delta t} \right)^p \tag{6.9}$$

The RHS is dealt with in a similar fashion.

Figure 6.3 show the Lagrange polynomials in $t$, for various $p$, calculated on the reference interval using the method described here:

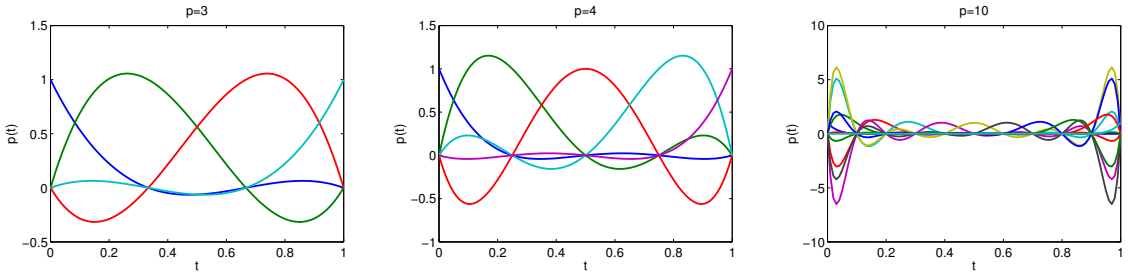


Figure 6.3: The reference interval $[0, 1]$ with polynomials in $t$ of degrees $p = 3$, $p = 4$, and $p = 10$.

## 6.4 Numerical Experiments

### 6.4.1 *p*-version on the Screen

**Example 6.** *Using the discretisation by piecewise polynomials of degree p described above, we compute the solution to the integral equation* $V\phi = f$ *on* $\mathbb{R}_t^+ \times \Gamma$ *with the square screen* $\Gamma = \{(x, y, 0) : -\frac{1}{2} \leq x, y \leq -\frac{1}{2}\}$ *depicted in Figure 6.4. We use a discretisation with* 8 *triangles and* 9 *nodes in space, a time step* $\Delta t = 0.5$*, resp.* 1.0*, and study the convergence of the numerical solution as the polynomial degree is increased. Several right hand sides f are considered. We compute the solution up to times* $T = 5$ *and compare to an extrapolated benchmark energy.*

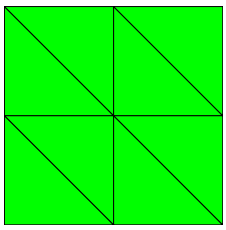

Figure 6.4: A coarse screen with 8 triangular elements and 9 nodes.

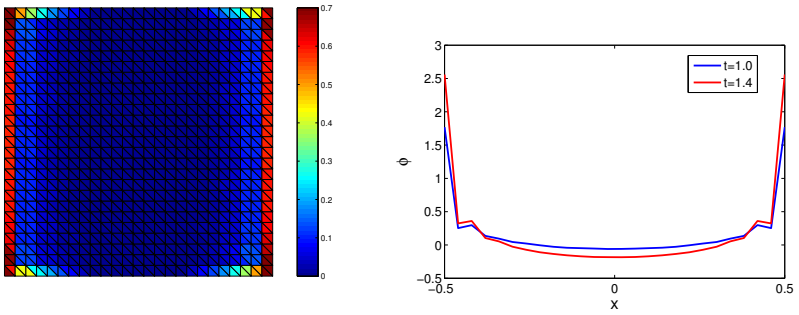


Figure 6.5: Density $\phi$ computed by $h$-method on a uniform mesh with 1250 triangles for $f_1$ (left), cross section $y = 0$ at $t = 1.0, 1.4$ (right).

From Chapter 4 and [61], the convergence rate in energy norm of the uniform $h$-method

on the screen is 0.5 as $h$ tends to 0. A picture of the solution for the right hand side

$$f_1(t, \mathbf{x}) = \sin^5(t)x^2$$

is shown in Figure 6.5, for a uniform triangulation of $\Gamma$ with 1250 triangles. The cross section at $y = 0$ shows the edge singularities of the solution, as well as the difficulty to approximate them numerically.

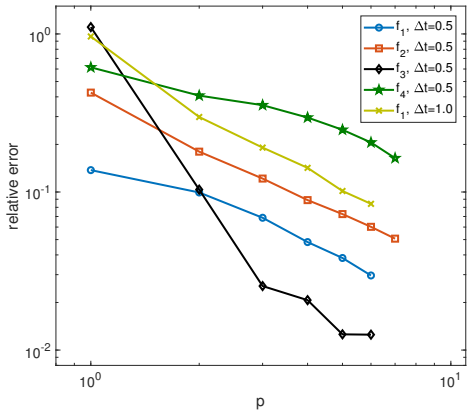


Figure 6.6: Energy error for single-layer equation on square screen, Example 6.

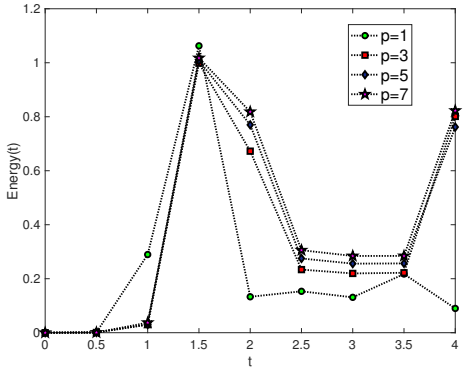


Figure 6.7: Energy as function of time for time-singular $f_4$, Example 6.

For this right hand side $f_1$, Figure 6.6 considers the convergence in energy norm of a $p$-method up to polynomial degree $p = 6$ in space and time. The empirical convergence rate, in $p$, for $\Delta t = 0.5$ (blue dots) turns out to be 1.21. For $\Delta t = 1.0$ the convergence

rate is 1.18 (yellow crosses). The results reflect the expected doubling of the convergence rate for the $p$-method, compared to the $h$-method.

The results are confirmed for plane-wave scattering at low frequencies. For the right hand side

$$f_2(t, \mathbf{x}) = \exp(-2/t^2)\cos(\omega t - \mathbf{kx}) \ ,$$

with $\mathbf{k} = (2, 0.5, 0.1)$ and $\omega = |\mathbf{k}|$, Figure 6.6 (red squares) shows the convergence in energy norm of the $p$-version with rate 1.02 up to $p = 7$, for $\Delta t = 0.5$. Again this is double the rate 0.5 of the $h$-method. For the higher-frequency wave

$$f_3(t, \mathbf{x}) = \exp(-2/t^2)\cos(\omega t - \mathbf{kx}) \ ,$$

with $\mathbf{k} = (6, 0.5, 0.1)$ and $\omega = |\mathbf{k}|$, piecewise linear or quadratic polynomials provide a poor approximation, as shown in Figure 6.6 (black diamonds) when $\Delta t = 0.5$. Nevertheless, at higher $p$ the convergence improves rapidly, and the rate becomes approximately 1.01.

Finally, a source which is nonsmooth in time is considered,

$$f_4(t, \mathbf{x}) = \sin^5(t)|1 - t|^\alpha \cos(\mathbf{k} \cdot \mathbf{x}) \ ,$$

with $\alpha = \frac{1}{2}$ and $\mathbf{k} = (6, 0.5, 0.1)$. Note the square-root singularity in time in this right hand side. Figure 6.7 shows the energy as a function of time at multiples of the time step 0.5, for $p = 1, 3, 5, 7$. While the solutions for different $p$ closely agree for short times, after the kink only high $p$ provide a qualitative approximation. The convergence rate in energy norm here is 0.78, see Figure 6.6 (green stars), less than for $f_1$, $f_2$ and $f_3$.

### 6.4.2 $p$-version on the Icosahedron

**Example 7.** *Using the discretisation by piecewise polynomials of degree p described above, we compute the solution to the integral equation $V\phi = f$ on $\mathbb{R}_t^+ \times \Gamma$ with the icosahedron $\Gamma$ depicted in Figure 6.8. We use the discretisation given by the* 20 *triangular faces with* 12 *vertices and a time step $\Delta t = 0.5$. The convergence of the numerical solution is studied*

*as the polynomial degree is increased. Different right hand sides $f$ are considered. We compute the solution for times up to $T = 11$ and compare to an extrapolated benchmark energy.*

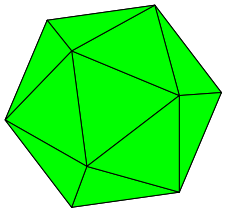

Figure 6.8: Icosahedron with 20 triangles and 12 vertices.

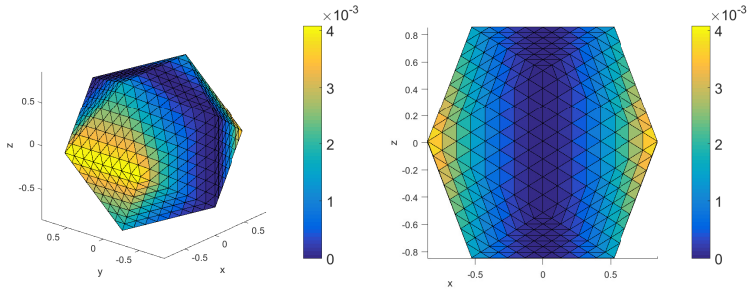


Figure 6.9: Density $\phi$ computed by $h$-method on a uniform mesh with 1280 triangles for $f_1$.

A picture of the smooth solution at time $t = 0.5$ for the right hand side

$$f_1(t, \mathbf{x}) = \sin^5(t)x^2$$

is shown in Figure 6.9, computed using an $h$-method on a uniform triangulation of $\Gamma$ with 1280 triangles and time step $\Delta t = 0.1$. The convergence of the $h$-method in Figure 6.10 (left) shows a convergence rate of 1.13 in $h$, or 0.376 in degrees of freedom.

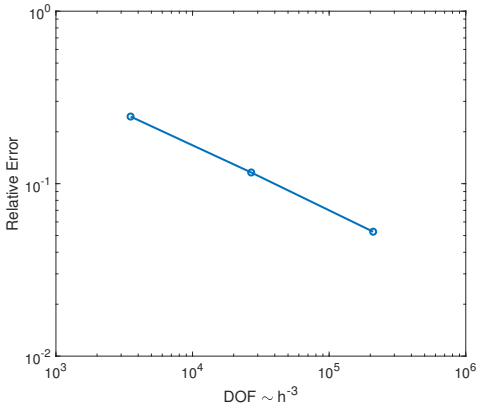


Figure 6.10: Energy error of $h$-method for single-layer equation on icosahedron, Example 7.

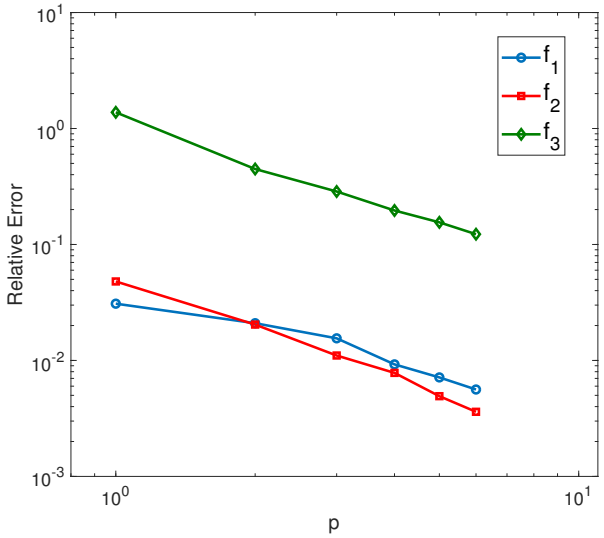


Figure 6.11: Energy error of $p$-method for single-layer equation on icosahedron, Example 7.

Figure 6.11 shows the convergence of the $p$-method in the energy norm for the right hand side $f_1$ from above (blue circles). The empirical convergence rate is 1.46 as the polynomial degree $p$ is increased. Figure 6.12 shows the possibility of long-time simulations and plots the energy of the numerical solution with $p = 6$ as a function up to time $t = 11$ at multiples of the time step 0.5. Figure 6.13 depicts the difference $|E_6(t) - E_p(t)|$ between the energy of the $p$-method solution for $p = 6$ and the numerical solutions for $p = 1, 2, \ldots, 5$. The error remains stable over the time interval and tends to 0 as $p$ increases.

A second right hand side investigates a plane-wave

$$f_2(t, \mathbf{x}) = \exp(-2/t^2)\cos(\omega t - \mathbf{kx}) \ ,$$

with $\mathbf{k} = (3, 0.5, 0.1)$ and $\omega = |\mathbf{k}|$. The convergence rate in this case is approximately 1.61.

Finally, a right hand side with a singularity in space is considered,

$$f_3(t, \mathbf{x}) = \sin^5(t)|\sin(\mathbf{kx})|^\alpha \ ,$$

$\alpha = \frac{1}{2}$ and $\mathbf{k} = (2, 0.5, 0.1)$. The convergence rate here is 1.22. Note that the solution $\phi$ has a singularity in space on the lines $\mathbf{kx} = k\pi$, $k \in \mathbb{Z}$, similar to the edge singularities in Example 6. The convergence rate is therefore reduced to values similar to those seen for screen problems in Example 6.

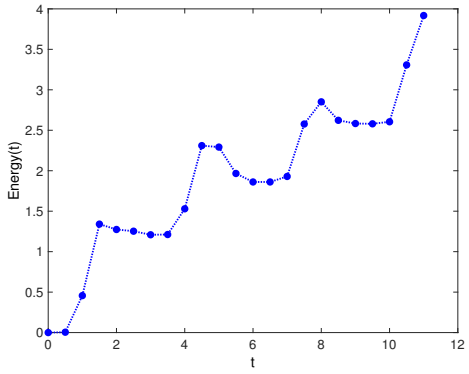


Figure 6.12: Energy as function of time up to $t = 11$ for the right hand side $f_1$, Example 7.

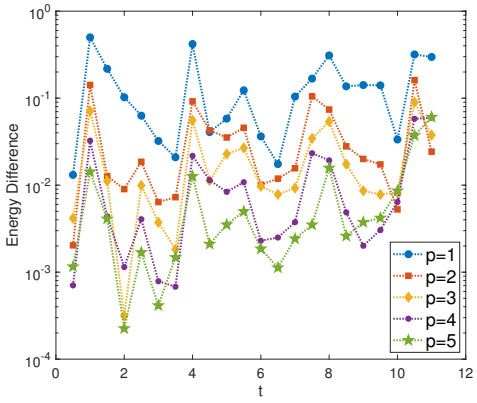


Figure 6.13: Energy difference between $p = 6$ and lower $p$, as function of time, Example 7.

# Chapter 7

# Enriched Methods

This chapter is based on joint work [62, 57] with H. Gimperlein.

## 7.1 Introduction

This work presents the algorithmic aspects behind a recently introduced time domain partition-of-unity method for the efficient solution of time-domain boundary integral equations such as Equation 7.3, based on travelling plane waves as ansatz and test functions in space and time. This is the first approach to *space − time enriched* partition-of-unity methods, here applied to a time-dependent integral equation. It extends its counterparts for time-harmonic wave propagation to truly transient problems at higher frequencies, but still allows to work on coarse meshes. Future applications are expected in the computational acoustics of concert halls [32], the noise of inner-city traffic and high-speed trains [22].

After a short review of relevant earlier works in TDBEM and partition-of-uniy methods, we here discuss the algorithmic background of the method. We focus on the new challenges arising in time-domain with non-polynomial basis functions on coarse mesh grids. Details of the accurate quadrature to assemble the Galerkin matrix are discussed, extending the methods known for standard $h$-version TDBEM. We then address the efficient numerical solution of the space-time system and its preconditioning. Numerical results demonstrate key aspects of the method: Reductions of the degrees of freedom of

around a factor 8, the efficient solution of the space-time system by a preconditioner, and condition numbers which are much reduced compared to partition-of-unity methods in frequency domain.

## 7.2 Formulation

### 7.2.1 Integral Formulation of the Wave Equation

Recall from the introduction the initial problem for the wave equation with inhomogeneous Dirichlet boundary conditions:

$$\begin{aligned} \partial_t^2 u(t,\mathbf{x}) - c^2 \Delta u(t,\mathbf{x}) &= 0 \qquad && \text{for } \mathbf{x} \in \Omega \\ u(t,\mathbf{x}) &= f(t,\mathbf{x}) && \text{for } \mathbf{x} \in \Gamma \\ u(t,\mathbf{x}) &= 0 && \text{for } t \leq 0. \end{aligned} \tag{7.1}$$

As before, we set $c = 1$. We make an ansatz for the sound pressure in $u$ in terms of the single-layer potential in 3 dimensions:

$$u(t,\mathbf{x}) = \int_\Gamma \frac{\phi(t - |\mathbf{x}-\mathbf{y}|, \mathbf{y})}{4\pi|\mathbf{x}-\mathbf{y}|} ds_y \qquad (\mathbf{x} \in \mathbf{\Omega}) \tag{7.2}$$

The condition $\phi = 0$ for $t \leq 0$ represents the causal propagation of waves on the light cone. Combining 7.2 with the boundary condition 7.1, we obtain a formulation of the wave equation as an integral equation of the first kind on $\Gamma$:

$$V\phi(t,\mathbf{x}) = \int_\Gamma \frac{\phi(t - |\mathbf{x}-\mathbf{y}|, \mathbf{y})}{4\pi|\mathbf{x}-\mathbf{y}|} ds_y = f(t,\mathbf{x}) \qquad (\mathbf{x} \in \mathbf{\Gamma}). \tag{7.3}$$

The solution to the original problem 7.1 in a point $\mathbf{x} \in \Gamma$ is recovered from $\phi$ by evaluating the integral 7.3 in a postprocessing step.

Anisotropic space-time sobolev spaces provide the proper analytic framework for Equa-

tion 7.3. The space $H^s_\sigma(\mathbb{R}^+, H^r(\Gamma))$ consists of those distributions $\phi$ on $[0,\infty)\times\Gamma$ which vanish at $t = 0$ and whose space-time Fourier-Laplace transform $F\phi$ satisfies in local coordinates:

$$||\phi||_{s,r,\Gamma} = \left( \int\int |\omega + i\sigma|^{2s}(\omega + i\sigma)^2 + |\xi|^2)^r |F\phi(\omega + i\sigma, \xi|^2 \quad d\xi d\omega \right)^{\frac{1}{2}} < \infty \qquad (7.4)$$

See [56, 71] for a detailed presentation.

The numerical solution of 7.3 is based on the following coercive weak formulation: Find $\phi$ such that for all $\psi$

$$\int_0^\infty \int_\Gamma (V\phi(t,\mathbf{x}))\partial_t\psi(t,\mathbf{x})\ ds_x\ d_\sigma t = \int_0^\infty \int_\Gamma f(t,\mathbf{x})\partial_t\psi(t,\mathbf{x})\ ds_x\ d_\sigma t\ , \qquad (7.5)$$

with $d_\sigma t = e^{-2\sigma t}dt$. While a theoretical analysis requires $\sigma > 0$, practical computations use $\sigma = 0$ [16].

This weak formulation is well posed [71]:

**Theorem G**. If $f \in H^2_\sigma(\mathbb{R}^+, H^{\frac{1}{2}}(\Gamma))$ then the retarded potential equation (7.3) admits a unique solution $\phi \in H^1_\sigma(\mathbb{R}^+, H^{-\frac{1}{2}}(\Gamma))$ satisfying:

$$||\phi||_{1,-\frac{1}{2},\Gamma} \leq C||f||_{2,\frac{1}{2},\Gamma} \qquad (7.6)$$

### 7.2.2 Partition-of-Unity Space-Time Discretisation

For the solution of 7.5, [65] proposes a time-dependent partition-of-unity boundary element method based on numerical approximation by travelling plane waves.

To be specific, for the time discretisation we consider a decomposition of the time interval $\mathbb{R}^+$ into subintervals $[t_{n-1}, t_n]$ with constant time step $\Delta t$, such that $t = n\Delta t, \quad (n = 0, 1, 2, ..., N_t)$.

In space, we approximate $\Gamma$ by a polygonal surface and denote the approximation again by $\Gamma$. We assume that $\Gamma = \cup_{i=1}^{N} \Gamma_i$, is a quasi-uniform triangulation, with triangular faces $\Gamma_i$. We choose a basis $\{\Lambda_1, \Lambda_2, ..., \Lambda_{N_s}\}$ of hat functions for the space of piecewise polynomials associated to the triangulation, continuous if the degree $\geq 1$. Similarly, for the time discretisation we choose a basis $\{\widetilde{\Lambda}_1, \widetilde{\Lambda}_2, ..., \widetilde{\Lambda}_{N_s}\}$ of piecewise polynomial hat functions, which are continuous and vanish at $t = 0$ if the degree $\geq 1$. The enrichment is best on a lattice of frequency vectors $\mathbb{K} \subset \mathbb{R}^3$.

We consider test and ansatz spaces based on tensor products of functions in space and time:

$$V_{h,\Delta t} = \text{span}\Big\{ G^i_{jl}(t, \mathbf{x}) := \widetilde{\Lambda}_i(t)\Lambda_j(\mathbf{x}) \cos\left(\omega_i(t - t_i) - \mathbf{k}_l \cdot \mathbf{x} + \sigma_l\right) : \mathbf{k}_l \in \mathbb{K}, \omega_l = |\mathbf{k}_l|, \sigma_l \in \{0, \frac{\pi}{2}\} \Big\} \tag{7.7}$$

The spatial part of the enrichment corresponds to the plane waves $\cos(\mathbf{k}_l \cdot \mathbf{x} + \sigma_l)$ routinely used in partition-of-unity methods in frequency domain [103]. The spatial part has recently been used in space-enriched methods for the time domain [45, 75].

For $u_{\Delta t,h} \in V_{h,\Delta t}$ we thus may write

$$u_{\Delta t,h}(t, \mathbf{x}) = \sum_{i=0}^{N_t} \sum_{j=0}^{N_s} \sum_{k_l \in \mathbb{K}} c^i_{jl} G^i_{jl}(t, \mathbf{x}). \tag{7.8}$$

The partition-of-unity discretisation of the weak formulation 7.5 now reads: Find $\phi_{h,\Delta t} \in V_{h,\Delta t}$ such that for all $\psi_{h,\Delta t} \in V_{h,\Delta t}$ such that

$$\int_0^\infty \int_\Gamma (V\phi_{h,\Delta t}(t, \mathbf{x}) \partial_t \psi_{h,\Delta t}(t, \mathbf{x}) ds_x dt = \int_0^\infty \int_\Gamma f(t, \mathbf{x}) \partial_t \psi_{h,\Delta t}(t, \mathbf{x}) ds_x dt \tag{7.9}$$

From the solution $\phi_{h,\Delta t}$, the numerical approximations $u_{h,\Delta t}$ to the solution of the wave equation 7.1 is obtained in $\Omega$ by evaluating the integral of the single-layer potential in 7.2

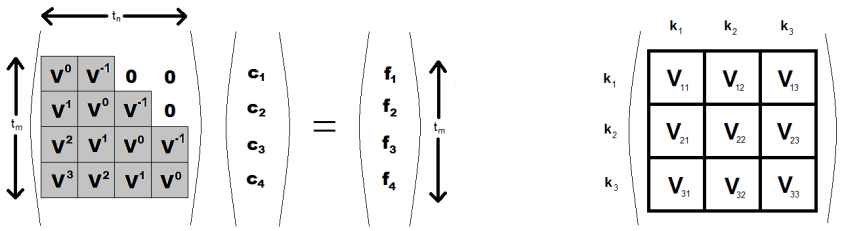


Figure 7.1: Full PUBEM space-time system for piecewise linear hat functions and decomposition of the blocks $V^j$.

numerically.

As a conforming Galerkin discretisation, Equation 7.9 admits a unique solution and leads to a stable partition-of-unity method in space-time.

### 7.2.3 Quadrature Method for Retarded Potentials

A main challenge of the PUBEM 7.9 is the accurate and efficient assembly of the Galerkin matrix. As depicted in Figure 7.1, the matrix is a block Toeplitz matrix where every block corresponds to a time step. Each of the blocks decomposes into blocks for the individual enrichments $\mathbf{k}_i$. Because of causality the spacetime matrix is almost lower triangular: If the hat functions in time are piecewise polynomials of degree $q$, blocks which are more than $q$ bands above the diagonal vanish.

The blocks of the matrix are explicitly given by

$$V^i = \int_0^\infty \int_{E(T)\cap\hat{T}} \int_{E(\mathbf{x})\cap T} \frac{G^m_{jl}(t-|\mathbf{x}-\mathbf{y}|)}{4\pi|\mathbf{x}-\mathbf{y}|} \partial_t G^{m+i}_{j'l'}(t,\mathbf{x}) \quad ds_y ds_x dt \tag{7.10}$$

Here $T$ and $\hat{T}$ are the test and trial elements. $E(\mathbf{x})$ the light cone around $\mathbf{x}$ and $E(T)$ the union of light cones around points in $T$. See Figure 7.2. $i \in \{1, 2, ..., N_t\}$ indexes the time nodes. After an analytical evaluation of the time integral, the inner ($\mathbf{y}$) integral requires integration over geometrically complicated intersections of triangles with lightcone shells, with a singular integrand $|\mathbf{x}-\mathbf{y}|^{-1}$:

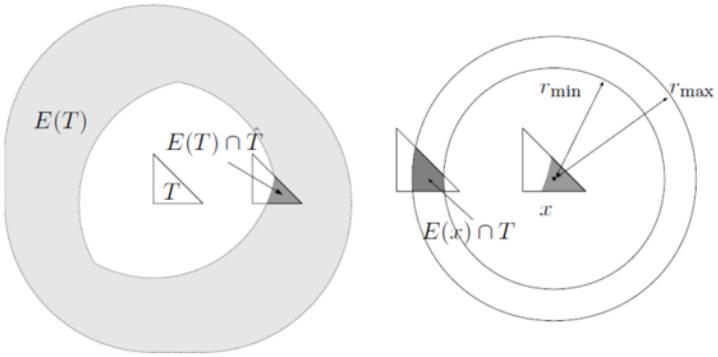


Figure 7.2: Outer (left) and inner (right) integration. Figure taken from [102].

$$V^i = \int_0^\infty \int_{E(T)\cap\hat{T}} \int_{E(\mathbf{x})\cap T} \frac{1}{|\mathbf{x}-\mathbf{y}|} \Lambda_j(\mathbf{y})\Lambda_{j'}(\mathbf{x}) F(\mathbf{y},\mathbf{x},\mathbf{k}_l,\omega_l,\mathbf{k}_{l'},\omega_{l'}) \tag{7.11}$$

for an explicitly given function $F$, given below in Section 7.2.4.

Difficulties arise: Kernel singularities when $|\mathbf{x}-\mathbf{y}|$ approaches zero, geometric singularities in $F$ at the boundary of light cones (see below), and the oscillatory behaviour of the basis functions for large $\mathbf{k}_l$, $\mathbf{k}_{l'}$. The first problem is standard in BEM, and we avoid it by using a quadrature *hp*-graded towards the singularity at $|\mathbf{x}-\mathbf{y}| = 0$.

More precisely, the following graded quadrature is performed to evaluate an integral of the form $\int_0^b f\,ds$ in the normal direction to $s = |\mathbf{x}-\mathbf{y}| = 0$. Denote by $Q_n^{[0,b]} f := \sum_{i=1}^n w_i f(x_i)$ the Gauss -Legendre quadrature rule with $n$ quadrature points. Given a subdivision of $[0,b]$ into $m$ subintervals $I_j$, define a composite Gauss rule with degree vector $\mathbf{n} = (n_1,\ldots,n_m)$ by $Q_{n,m,\sigma} f := \sum_{j=1}^m Q_{n_j}^{I_j} f$ . We use a geometric subdivision of $[0,b]$ with $m$ levels and grading parameter $\sigma \in (0,1)$: $[0,b] = \bigcup_{j=1}^m I_j$, where for $j = 1,\ldots,m$ we let $I_j := [x_{j-1}, x_j]$, $x_0 := 0$, $x_j := b\sigma^{m-j}$ with suitable $\mathbf{n}$. See [111] for an analysis of this quadrature for time-independent integral equations.

For the second problem, we project the point of observation $\mathbf{x}$ onto the triangle plane and use a careful decomposition of the area of integration into smple standard shapes $D_i$

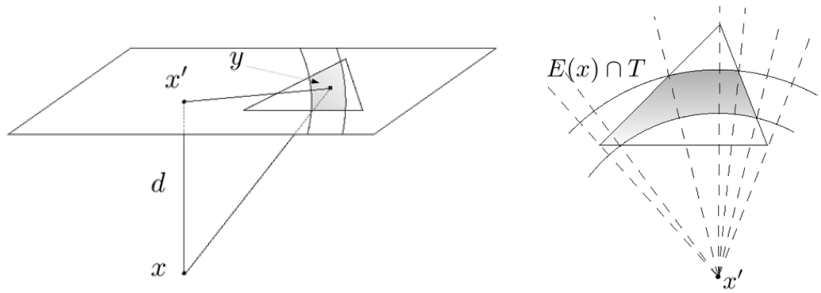


Figure 7.3: Projection of point of observation ($\mathbf{x}$) onto the triangle plane (left). Partitioning of the area of integration for inner quadrature (right). Figure taken from [102].

in polar coordinates. The inner integral thus becomes:

$$\sum_{l=1}^{n_d} \int_{D_l} |d^2 + r^2|^{\frac{p-1}{2}} \Lambda(\mathbf{y}) ds_y \tag{7.12}$$

To evaluate the integrals over $D_i$, we apply seperate graded quadratures in the radial and angular variables, with at least 10 Gauss points per wave length to resolve oscillations. See Figure 7.3.

The outer integral is less singular and ses a standard composite Gauss quadrature with at least 10 points per wavelength.

### 7.2.4 Detailed Analysis of Integration in $F$

A more detailed analysis shows that the matrix entries are of the form:

$$= \int_0^\infty \int_\Gamma \int_\Gamma \frac{1}{|\mathbf{x}-\mathbf{y}|} \widetilde{\Lambda}_m\big(t-|\mathbf{x}-\mathbf{y}|\big) \Lambda_m(\mathbf{y}) \cos\left(\omega_m\big(t-t_m-|\mathbf{x}-\mathbf{y}|\big) - \mathbf{k}_m\cdot\mathbf{y}+\sigma_m\right) ds_y$$

$$\cdot \quad \left[\dot{\widetilde{\Lambda}}_n(t)\Lambda_n(\mathbf{x}) \cos\left(\omega_n(t-t_n)-\mathbf{k}_n\cdot\mathbf{x}+\sigma_n\right) - \widetilde{\Lambda}_n(t)\Lambda_n(\mathbf{x}) \sin\left(\omega_n(t-t_n)-\mathbf{k}_n\cdot\mathbf{x}+\sigma_n\right)\omega_n\right] ds_x dt. \tag{7.13}$$

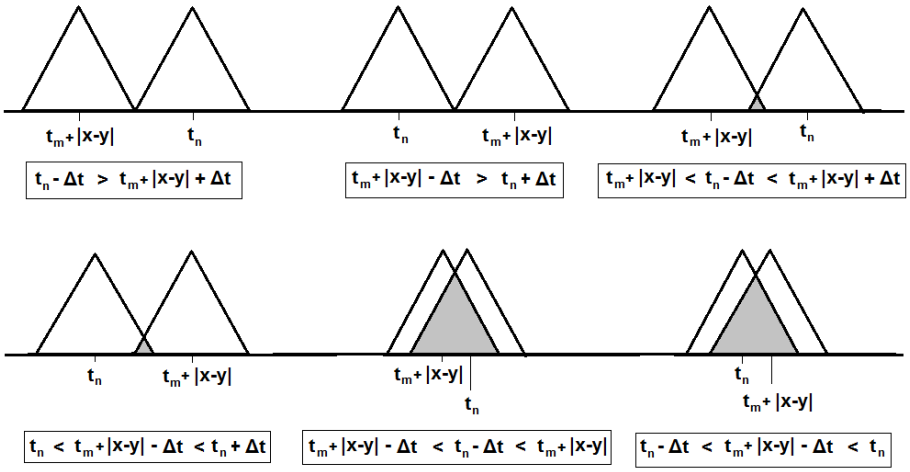


Figure 7.4: Possible intersections of temporal basis functions. Figure taken from [62].

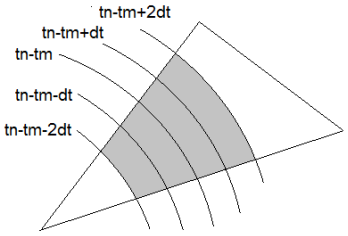


Figure 7.5: Division into light cones corresponding to cases in Figure 7.4. Figure taken from [62].

The hat functions $\widetilde{\Lambda}_m$ and $\widetilde{\Lambda}_n$ exhibit four nontrivial cases of overlap, see Figure 7.4. The resulting kinks in $F$ are exhibited in Figure 7.5.

### 7.2.5 A Preconditioner for PUBEM

The space-time systems as in Figure 7.1, which arise from standard polynomial $h$-method time domain Galerkin boundary element discretisations with piecewise constant test functions hat functions $\widetilde{\Lambda}_n(t)$ in time, are lower triangular. Indeed, for a matrix block

$$V^i = \int_0^\infty \int_{E(T)\cap\hat{T}} \int_{E(\mathbf{x})\cap T} \frac{\widetilde{\Lambda}_m(t-|\mathbf{x}-\mathbf{y}|)}{4\pi|\mathbf{x}-\mathbf{y}|} \partial_t \widetilde{\Lambda}_{m+i}(t,\mathbf{x}) \quad ds_y ds_x dt \tag{7.14}$$

with piecewise constant test functions $\widetilde{\Lambda}_{m+i}$, the argument $t-|\mathbf{x}-\mathbf{y}|$ of the ansatz function lets the integrand vanish whenever $i < 0$. In particular, the block $V^{-1}$ in Figure 7.1 is 0. The resulting space-time system may then be solved by backsubstitution, which leads to efficient time stepping schemes.

For test functions of order $q$, the space-time systems has $q$ bands of blocks above the diagonal. Nevertheless, an extrapolation leads to efficient time stepping schemes with engineering accuracy, as is adequate for the use in partition-of-unity methods. We discuss the approach for piecewise linear functions.

Denoting the solution vector at time $t_{j+1}$ by $c^{j+1}$, one approximates its value from previous time steps by extrapolation $c^{j+1} \approx c^j + (c^j - c^{j-1})$ in order to eliminate the blocks $V^i$ for $i < 0$ in Figure 7.1. For smooth solutions the error of this approximation is of the order of the time step $\Delta t$, and therefore of a similar size as the error from the finite element approximation. Substituting this value $c^{j+1} \approx c^j + (c^j - c^{j-1})$ into the space-time systems:

$$F^j = V^1 c^{j-1} + V^0 c^j + V^{-1} c^{j+1} \approx (V^1 - V^{-1}) c^{j-1} + (V^0 + 2V^{-1}) c^j. \tag{7.15}$$

The result is a block Toeplitz equation $\widetilde{V} c = F$ in space-time, which is block lower triangular in the sense that $\widetilde{V}^i = 0$ for $i < 0$. This system can now be stably solved by backsubstitution. Here the bands are given by

$$\widetilde{V}^0 = (V^0 + 2V^{-1}), \widetilde{V}^1 = (V^1 - V^{-1}), \widetilde{V}^j = V^j \quad \text{if} \quad j > 1. \tag{7.16}$$

The resulting time-stepping scheme may be used either as a stand-alone solver or as a preconditioner for GMRES applied to the space-time matrix. Both have been studied in a variety of wave propagation and scattering problems in [64]. In the current paper we employ 7.16 as a preconditioner of the PUBEM.

Instead of preconditioned GMRES, one may use special solvers for Toeplitz systems.

However, the preconditioner suffices for all applications considered so far, and special solvers for non-symmetric block Toeplitz systems do not seem to be readily available in standard libraries.

## 7.3 Numerical Experiments

**Example 1** : For a regular icosahedron $\Gamma$, Figure 7.6, of diameter 2 and centered in $(0,0,0)$, we use the right hand side $f(t,\mathbf{x}) = \exp(-25/t^2)\cos(\omega_f t - \mathbf{k}_f \mathbf{x})$. $f$ represents a plane wave with $\mathbf{k}_f = (1.5, 3, 8.5)$ which is smoothly turned on for times $[0,5]$. The partition-of-unity TDBEM approximation from (7.9) is compared to an h-method TDBEM with piecewise linear ansatz and test functions on a uniform mesh with up to 1280 triangles and constant CFL ratio $\frac{\Delta t}{\Delta x} = 0.19$. Figure 7.6 depicts the h-method solution $\phi$ at times 3.8, 4.2 and 4.6 and the fine mesh of 1280 triangles used for its computation.

Figure 7.7 (left) illustrates the solution of the partition-of-unity method, evaluated in the centroid $(0.46, 0.46, 0.46)$ of a triangle. The partition-of-unity TDBEM uses a mesh of 20 triangles as in the left-most picture in Figure 7.6 and $n$ enrichment functions in each triangle, for $n \leq 15$ and $\Delta t = 0.1$, resp. 0.2.

For a variational method as discussed in this chapter, a natural measure of the error is the energy defined by the single layer operator, which is computed from the stiffness matrix $V$, the right hand side vector $f$ and the solution vector $c$ as $E(c) = \frac{1}{2}c^\top V c - c^\top F$. We compute the relative energy error with respect to the energy $E_\infty$ of an extrapolated benchmark energy as $\frac{E(c)-E_\infty}{E_\infty}$. This energy error is is relevant also because it controls the resulting pointwise error of the sound pressure $u$ to the original problem (1.1), as obtained from $\phi$ by evaluating the integral (8.2).

Figure 7.7 (right) compares the convergence of the relative energy error between the above-described $h$-method and the partition-of-unity method as the total number of space-time degrees of freedom is increased. While the $h$-method is consistent with the well-known linear convergence [61], the partition-of-unity method exhibits its typical

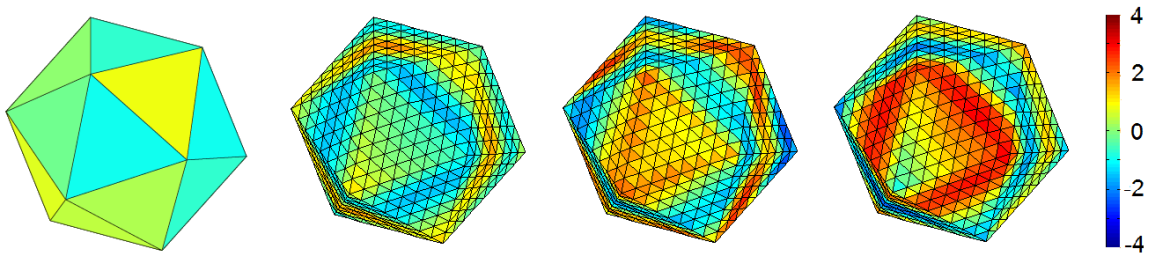


Figure 7.6: Example 1 - meshes for PU (20 triangles) and h-method (1280 triangles), density at $t = 3.8, 4.2, 4.6$.

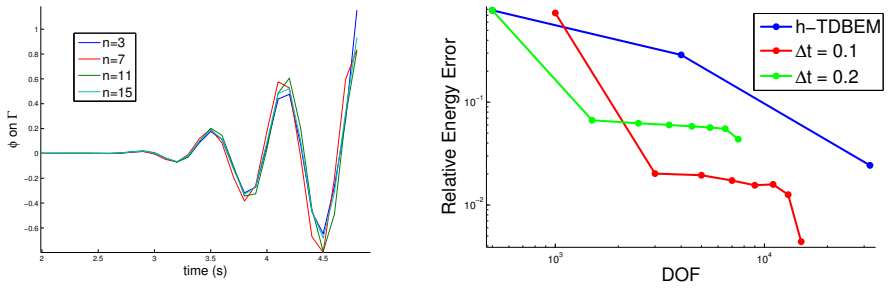


Figure 7.7: Example 1 - a) density $\phi$ at point $(0.46, 0.46, 0.46)$, b) relative error in energy: h-method, PU with $\Delta t = 0.1, 0.2$, for $n = 1, 3, 5, ..15$ enrichment functions.

nonlinear convergence with abrupt decreases. The precise errors are detailed in Table 7.1. The partition-of-unity method here reduces the space-time degrees of freedom by a factor up to 8, indicating the potential of the method. The savings in the degrees of freedom translate into reduced computation times also in the time-domain, see [45, 83].

**Example 2** : For the same regular icosahedron $\Gamma$, Figure 7.6, of diameter 2 and centered in $(0, 0, 0)$, we consider the right hand side:

$$f(t, \mathbf{x}) := \exp\left(\frac{-25}{t^2}\right) \cos\left(\omega_f(x_1)t - \mathbf{k}_f(x_1)\mathbf{x}\right). \tag{7.17}$$

| n | DOF | error PU ($\Delta t = 0.2$) | DOF | error PU ($\Delta t = 0.1$) | DOF | rel. error h |
|---|---|---|---|---|---|---|
| 1 | 500 | 0.78 | 1000 | 0.76 | 500 | 0.78 |
| 3 | 1500 | 0.065 | 3000 | 0.020 | 4000 | 0.28 |
| 5 | 2500 | 0.063 | 5000 | 0.019 | 20000 | 0.025 |
| 7 | 3500 | 0.060 | 7000 | 0.017 | | |
| 9 | 4500 | 0.058 | 9000 | 0.0145 | | |
| 11 | 5500 | 0.057 | 11000 | 0.015 | | |
| 13 | 6500 | 0.055 | 13000 | 0.012 | | |
| 15 | 7500 | 0.0042 | 15000 | 0.0043 | | |

Table 7.1: Errors of the PU and h-methods corresponding to Figure 7b.

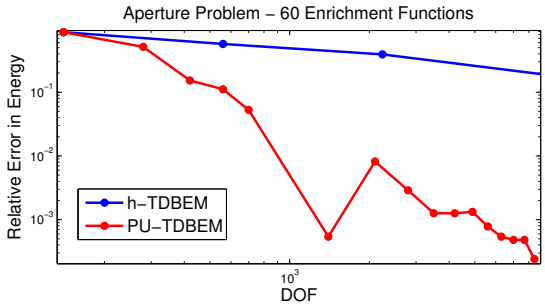


Figure 7.8: Example 2 - Relative energy error.

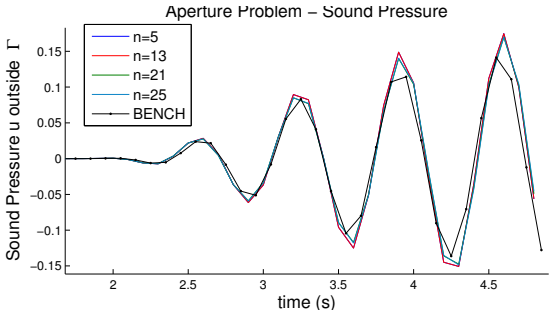


Figure 7.9: Example 2 - Sound pressure evaluated at (1.6, 0.1, 0.2) outside of $\Gamma$.

with:

$$\mathbf{k}_f(x_1) = \begin{bmatrix} 8.5 \\ 3 \\ 0.5 \end{bmatrix} + \alpha \begin{bmatrix} x_1 \\ 0 \\ 0 \end{bmatrix}, \qquad \text{where } \alpha = 0.5 \tag{7.18}$$

Using up to 60 enrichment functions, the partition-of-unity TDBEM approximation from (7.9) is compared to an h-method TDBEM with piecewise linear ansatz and test functions on a uniform mesh with up to 1280 triangles and constant CFL ratio $\frac{\Delta t}{\Delta x} = 0.19$. Figure 7.8 depicts the relative error in energy comparison between the PU-method and the $h$-method solution. Figure 7.9 shows the sound pressure evaluated at a point outside $\Gamma$ at $(1.6, 0.1, 0.2)$, for PU with various numbers of enrichments.

Figure 7.10 shows how the condition number grows in the Galerkin matrix, as more enrichments are included.

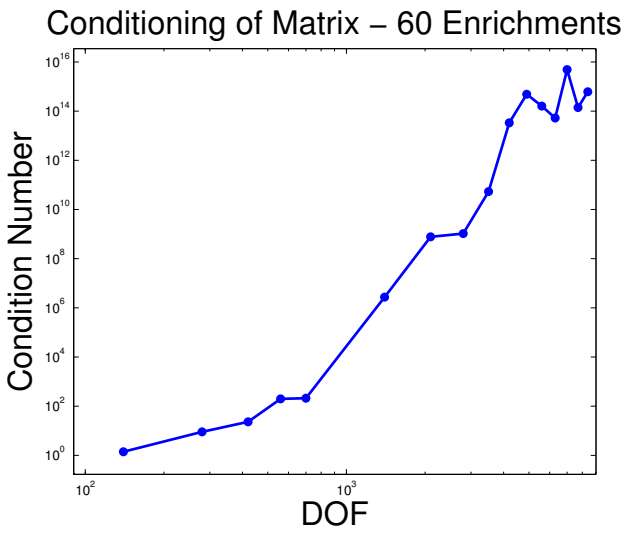


Figure 7.10: Example 2 - Condition number vs DOF.

# Chapter 8

# Solving the TDBEM Linear System

This chapter is based on joint work [64] with H. Gimperlein.

## 8.1 Introduction

This chapter studies a time stepping scheme to solve the space time systems arising from time domain Galerkin boundary element discretisations for higher order test functions. It approximates the algebraic system using linear extrapolation and may be used as either a preconditioner for the full space-time equation or as a fast, quasi-exact standalone solver of the integral equation for large numbers of degrees of freedom. Our method inherits the approximation properties and long-time stability of the Galerkin method.

In Section 8.2 we recall the boundary integral formulation of the wave equation and its numerical discretisation using boundary elements. The MOT time stepping scheme for the resulting space-time system is described in Section 8.3. Section 8.4 investigates the scheme as a preconditioner and as a standalone solver in numerical experiments on closed surfaces, screens and with non-polynomial basis functions.

## 8.2 Problem Formulation

We consider transient sound radiation problems in the exterior of a scatterer $\Omega^-$, where $\Omega^-$ is a bounded polygon or a screen with connected complement $\Omega = \mathbb{R}^3 \setminus \overline{\Omega^-}$. The

acoustic sound pressure field $u$ due to an incident field or sources on $\Gamma = \partial\Omega$ satisfies the linear wave equation for $t \in \mathbb{R}$:

$$c^{-2}\partial_t^2 u(t,\mathbf{x}) - \Delta u(t,\mathbf{x}) = 0 \quad \text{for } (t,\mathbf{x}) \in \mathbb{R}\times\Omega, \tag{8.1}$$
$$u(t,\mathbf{x}) = f(t,\mathbf{x}) \quad \text{for } \mathbf{x}\in\Gamma, \quad u(t,\mathbf{x}) = 0 \quad \text{for } t \le 0.$$

Here $c$ is the wave speed, and in the following we set $c = 1$ for simplicity. A single-layer ansatz for $u$,

$$u(t,\mathbf{x}) = \int_\Gamma \frac{\phi(t-|\mathbf{x}-\mathbf{y}|,\mathbf{y})}{2\pi|\mathbf{x}-\mathbf{y}|} ds_y, \tag{8.2}$$

results in an equivalent weak formulation of (8.1) as an integral equation of the first kind in space-time anisotropic Sobolev spaces [54]: Find $\phi \in H^1_\sigma(\mathbb{R}^+, \widetilde{H}^{-\frac{1}{2}}(\Gamma))$ such that for all $\psi \in H^1_\sigma(\mathbb{R}^+, \widetilde{H}^{-\frac{1}{2}}(\Gamma))$

$$\int_0^\infty \int_\Gamma (V\phi(t,\mathbf{x}))\partial_t\psi(t,\mathbf{x})\; ds_x\; d_\sigma t = \int_0^\infty \int_\Gamma f(t,\mathbf{x})\partial_t\psi(t,\mathbf{x})\; ds_x\; d_\sigma t\;, \tag{8.3}$$

where

$$V\phi(t,\mathbf{x}) = \int_\Gamma \frac{\phi(t-|\mathbf{x}-\mathbf{y}|,\mathbf{y})}{2\pi|\mathbf{x}-\mathbf{y}|} ds_y\;,$$

and $d_\sigma t = e^{-2\sigma t}dt$. A theoretical analysis requires $\sigma > 0$, but practical computations use $\sigma = 0$ [16, 54].

We study time dependent boundary element methods to solve (8.3), based on approximations by piecewise polynomial ansatz and test functions from the space $V^{p,q}_{h,\Delta t}$ spanned by

$$\phi_i(t,\mathbf{x}) = \widetilde{\Lambda}_i(t)\Lambda_i(\mathbf{x})\;. \tag{8.4}$$

Here, $\Lambda_i$ a piecewise polynomial shape function of degree $p$ in space and $\widetilde{\Lambda}_i$ a corresponding shape function of degree $q$ in time. For $p \ge 1$, resp. $q \ge 1$, the shape functions are assumed to be continuous.

We obtain a numerical scheme for the weak formulation (8.3): Find $\phi_{h,\Delta t} \in V^{p,q}_{h,\Delta t}$ such

that for all $\psi_{h,\Delta t} \in V_{h,\Delta t}^{p,q}$

$$\int_0^\infty \int_\Gamma \big(V\phi_{h,\Delta t}(t,\mathbf{x})\big)\partial_t\psi_{h,\Delta t}(t,\mathbf{x})\; ds_x\; dt = \int_0^\infty \int_\Gamma f(t,\mathbf{x})\partial_t\psi_{h,\Delta t}(t,\mathbf{x})\; ds_x\; dt\;. \tag{8.5}$$

From $\phi_{h,\Delta t}$, the sound pressure $u_{h,\Delta t}$ is obtained in $\Omega$ by evaluating the integral in (8.2) numerically.

Equation (8.5) leads to a linear system of equations in space-time, Figure 8.1, where

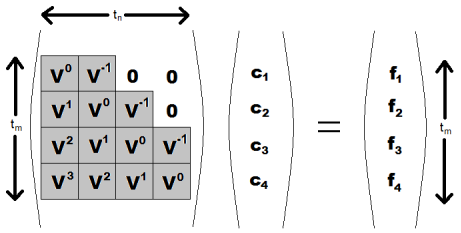


Figure 8.1: Full space-time system showing the bands $\mathbf{V}^j$.

the stiffness matrix

$$\mathbf{V}_{mn} = \int_0^\infty \int_\Gamma \int_\Gamma \frac{\phi_m(t-|\mathbf{x}-\mathbf{y}|,\mathbf{y})}{2\pi|\mathbf{x}-\mathbf{y}|}\partial_t\phi_n(t,\mathbf{x})\; ds_y\; ds_x\; dt$$

has a block-banded structure corresponding to the time steps.

A main challenge is the accurate assembly of $\mathbf{V}_{mn}$. After an analytical evaluation of the time integral, the $y$ integral requires integration over geometrically complicated intersections of triangles with light cone shells, with a singular integrand $|\mathbf{x}-\mathbf{y}|^{-1}$. It is evaluated in polar coordinates with a geometrically-graded *hp*-composite Gauss quadrature [54]. A regular Gauss quadrature is used for the $x$ integral.

We also consider a time domain *partition of unity* method. Here, the ansatz and test functions are, instead of (8.4), given by travelling plane waves

$$\phi(t,\mathbf{x}) = \widetilde{\Lambda}_i(t)\Lambda_j(\mathbf{x})\cos(\omega_i t - \mathbf{k}_l\cdot\mathbf{x} + \sigma_l)\;, \tag{8.6}$$

where $\omega_i = \|\mathbf{k}_l\|_2$, and $\sigma_l = \{0, \frac{\pi}{2}\}$. In this case each of the time step blocks in addition decomposes into blocks for the individual $\mathbf{k}_l$. See Figure 8.1.

.

## 8.3 Time Stepping Scheme for the Space-Time System

Because the blocks $\mathbf{V}^{-1}$ above the diagonal are nonzero for test functions of degree $\geq 1$ in time, in general the full space-time system (8.5) has to be solved for all time steps at once. Solving such large systems iteratively, e.g. using GMRES, can take a substantial number of iterations (and time) to achieve an acceptable tolerance. On the other hand, for test functions of degree 0 in time, $\mathbf{V}^{-1} = \mathbf{0}$, and backsubstitution leads to an efficient and popular time stepping scheme (MOT, *marching in on time*).

In this chapter we compare (8.5) with a similar time stepping scheme obtained from a lower-triangular approximation $\widetilde{\mathbf{V}}$ for $\mathbf{V}$. We use $\widetilde{\mathbf{V}}$ both as a preconditioner for GMRES and investigate its accuracy as a stand-alone solver.

For simplicity we restrict ourselves to piecewise linear functions in time, $q = 1$. The matrix $\widetilde{\mathbf{V}}$ is obtained from a linear extrapolation in time to approximate the solution vector for the next time step:

$$\mathbf{c}_{j+1} \simeq \mathbf{c}_j + (\mathbf{c}_j - \mathbf{c}_{j-1}) \ .$$

Inserting this into the $j$-th equation in Figure 8.1,

$$\mathbf{V}^{j-1}\mathbf{c}_1 + \cdots + \mathbf{V}^2\mathbf{c}_{j-2} + \mathbf{V}^1\mathbf{c}_{j-1} + \mathbf{V}^0\mathbf{c}_j + \mathbf{V}^{-1}\mathbf{c}_{j+1} = \mathbf{f}_j \ ,$$

we obtain

$$\begin{aligned} \mathbf{V}^{j-1}\mathbf{c}_1 + \cdots + \mathbf{V}^2\mathbf{c}_{j-2} + \mathbf{V}^1\mathbf{c}_{j-1} + \mathbf{V}^0\mathbf{c}_j + \mathbf{V}^{-1}(2\mathbf{c}_j - \mathbf{c}_{j-1}) &\simeq \mathbf{f}_j \\ \mathbf{V}^{j-1}\mathbf{c}_1 + \cdots + \mathbf{V}^2\mathbf{c}_{j-2} + \underbrace{(\mathbf{V}^1 - \mathbf{V}^{-1})}_{\widetilde{\mathbf{V}}^1}\mathbf{c}_{j-1} + \underbrace{(\mathbf{V}^0 + 2\mathbf{V}^{-1})}_{\widetilde{\mathbf{V}}^0}\mathbf{c}_j &= \quad . \end{aligned}$$

Therefore, we define $\widetilde{\mathbf{V}}$ as the lower-triangular block Toeplitz matrix with bands $\widetilde{\mathbf{V}}^i = \mathbf{V}^i$

for $i > 1$, $\widetilde{\mathbf{V}}^1 = \mathbf{V}^1 - \mathbf{V}^{-1}$ and $\widetilde{\mathbf{V}}^0 = \mathbf{V}^0 + 2\mathbf{V}^{-1}$. Solving the lower triangular system $\widetilde{\mathbf{V}}\mathbf{c} = \mathbf{F}$ by backsubstitution, we obtain a modified MOT scheme.

## 8.4 Numerical Results

We explore the relevance of $\widetilde{\mathbf{V}}$ in three model problems for plane-wave scattering from an icosahedron or sphere, resp. a screen. For all three problems, we use ansatz and test functions in $V_{h,\Delta t}^{0,1}$. As a preconditioner within GMRES, the computational cost is similar to a matrix-vector multiplication and approximately doubles the cost of each GMRES iteration.

**Example 1:** First we consider a sphere $\Gamma = S^2$ with right hand side $f(t,x) = \sin(2t)^5$. The exact solution is given by $\phi(t,x) = 10\cos(2t)\sin(2t)^4$. We choose a time interval $[0,T] = [0,2.5]$ and uniform meshes of 320 triangles with time step $\Delta t = 0.04$, resp. 1280 triangles with $\Delta t = 0.02$, thereby keeping the CFL number $\frac{\Delta t}{\Delta x}$ fixed.

We solve the resulting system with standard GMRES and with the $\widetilde{\mathbf{V}}$-preconditioned GMRES until the standard residual error indicator for GMRES is smaller than $10^{-9}$; for GMRES this indicator is $\|\mathbf{V}\mathbf{c} - \mathbf{F}\|_2$, while it is $\|\widetilde{\mathbf{V}}^{-1}(\mathbf{V}\mathbf{c} - \mathbf{F})\|_2$ for the preconditioned GMRES. Figure 8.4 compares the residual $\|\mathbf{V}\mathbf{c} - \mathbf{F}\|_2$ in each iteration. Note that the preconditioner not only reduces the number of iterations compared to the standard GMRES, but fewer preconditioned GMRES iterations are required for 1280 triangles: The extrapolation in time used to construct $\widetilde{\mathbf{V}}$ becomes exact as $\Delta t$ tends to 0, provided $\phi$ is sufficiently regular. We explore the stability and accuracy of the preconditioner in detail for more realistic scattering problems below.

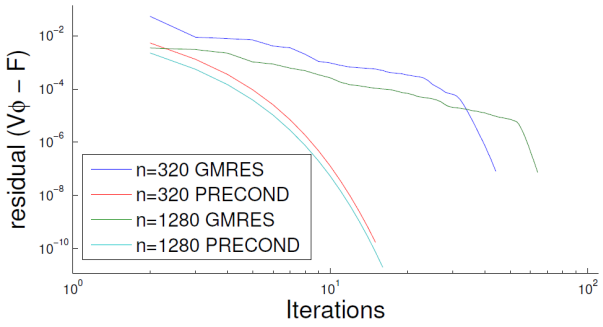


Figure 8.2: Residual of GMRES for $\Gamma = S^2$ with 320, 1280 triangles.

For the current example, we can easily compare the resulting error of GMRES with the discretisation error in the density $\phi$. Figure 8.3 shows that the error $\|\phi - \phi_{h,\Delta t}\|_{L^2([0,T]\times\Gamma)}$ is dominated by the discretisation error for both 320 and 1280 triangles. However, the contribution of the GMRES error increases for finer meshes and is nonnegligible in the first iterations.

For the preconditioned GMRES the error is negligible already after one iteration. Indeed, Figure 8.4 shows the relative error from the results of Figure 8.3 for the preconditioned GMRES. For both 320 and 1280 DOF, the density converges to the exact density of the discretized problem at approximately the same rate and magnitude.

We also consider the error between the solutions to $\widetilde{\mathbf{V}}\mathbf{c} = \mathbf{F}$ and $\mathbf{V}\mathbf{c} = \mathbf{F}$, i.e. the use of the preconditioner as a stand-alone solver: As described in Table 8.1, the relative error in energy is well below 1% after an application of the preconditioner, resp. a single step of preconditioned GMRES. For 1280 triangles, a single iteration of the preconditioner yields a practically exact energy. Analogous results are obtained for the density instead of the energy, see e.g. Figure 8.4. Figure 8.5 finally shows that standard convergence plots for the error of either the energy or the norm $L^2([0,T]\times\Gamma)$ may be calculated from the preconditioner as a standalone solver: The convergence rates coincide with those calculated from numerical solutions using the preconditioned GMRES solver.

| Example | Geometry | spatial DOF | Energy | Preconditioner | 1 precond. GMRES |
|---|---|---|---|---|---|
| 1 | sphere | 320 | 8.5692 | 8.5470 (.26%) | 8.5481 (.25%) |
| | | 1280 | 8.6059 | 8.6059 ($\ll$ 1%) | 8.5954 (.12%) |
| 2 | icosahedron | 320 | 20.5388 | 21.4801 (4.6%) | 21.6785 (5.5%) |
| | | 1280 | 19.8796 | 20.1434 (1.3%) | 20.159 (1.4%) |
| 3 | screen | 288 | 0.4233 | 0.4497 (6.2%) | 0.4522 (6.8%) |
| | | 1250 | 0.4589 | 0.4716 (2.8%) | 0.4721 (2.9%) |
| 4 | icosahedron | 7 enrichments | 23.6226 | 23.126 (2.1%) | 16.897 (28.5%) |
| | (using PU) | 15 enrichments | 22.9151 | 22.685 (1.0%) | 20.947 (8.6%) |

Table 8.1: Energy and relative errors in energy for preconditioner, resp. a single step of preconditioned GMRES.

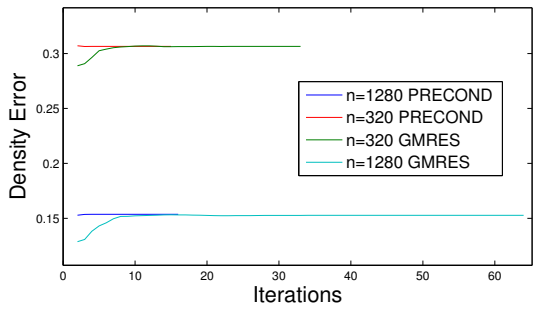


Figure 8.3: Error $\|\phi - \phi_{h,\Delta t}\|_{L^2([0,T]\times\Gamma)}$ for $\Gamma = S^2$ with 320, 1280 triangles.

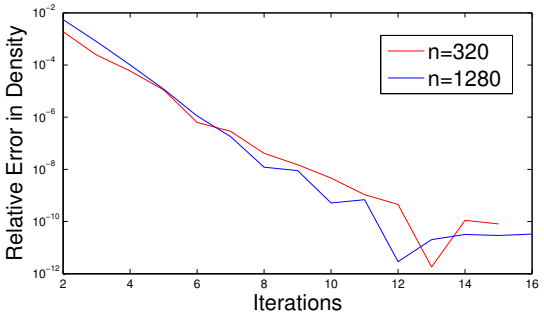


Figure 8.4: Relative error in Figure 8.3 for the preconditioned GMRES with 320, 1280 triangles.

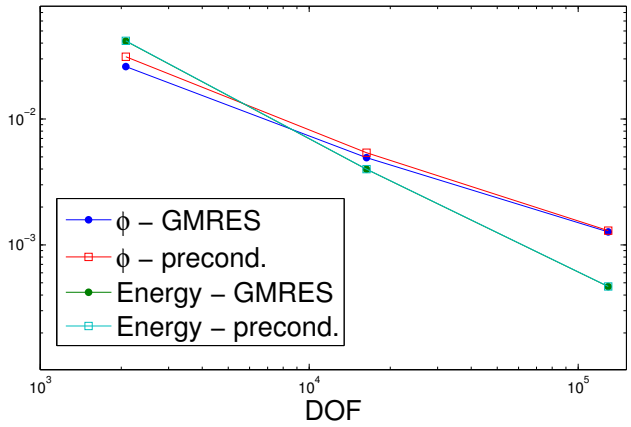


Figure 8.5: Convergence of TDBEM using preconditioned GMRES, resp. the preconditioner as standalone solver: relative errors in energy and $L^2([0,T]\times\Gamma)$.

**Example 2:** The second experiment considers plane-wave scattering from an icosahedron of diameter 2 centred in $\mathbf{0}$. The right hand side is given by $f(t,\mathbf{x}) = \exp(-25/t^2)\cos(\omega_f t - \mathbf{k}_f\mathbf{x})$, where $\mathbf{k}_f = (1.5, 3, 8.5)$ and $\omega_f = \|\mathbf{k}_f\|_2$. For the discretisation we consider uniform meshes with 20, 80, 320, 1280, 5120 triangles and corresponding time steps $\Delta t = 0.16,\ 0.08,\ 0.04,\ 0.02,\ 0.01$ in the time interval [0,T]=[0,5]. The icosahedron and snapshots of the numerical solution for 1280 triangles are shown in Figure 8.6.

Figure 8.7 depicts the number of iterations needed to achieve a residual error indicator as in Example 1 of $< 10^{-7}$ for increasing degrees of freedom. Unlike the standard GMRES solver, the preconditioned GMRES is stable, and its iteration count even decreases from 25 to 19 for the considered meshes. Figure 8.8 shows the convergence of the residuals in each iteration for 320 and 1280 triangles, with and without preconditioner. The preconditioner leads to a consistently larger reduction of the residual in every step, and for the finer mesh the norm of the residual of the preconditioned GMRES is reduced by a multiplicative constant. Similarly, Figure 8.9 shows the improved convergence of the energy. This reinforces our conclusion from Example 1 that the preconditioner becomes exact as $\Delta t$ to 0 in a realistic scattering problem.

Unlike in Example 1, however, Table 8.1 shows that the error of a single step of preconditioned GMRES, resp. the preconditioner alone, does not decrease the error of the energy below 1% for this more realistic scattering problem. The relative error of the energy decreases to around 1%, though, for 1280 triangles, an accuracy that may suffice

for large scale engineering applications.

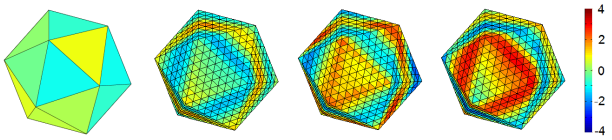


Figure 8.6: Meshes for icosahedron with 20 and 1280 triangles.

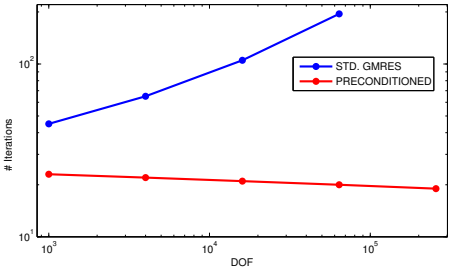


Figure 8.7: Iterations vs. DOF to achieve a residual $< 10^{-9}$ on the icosahedron.

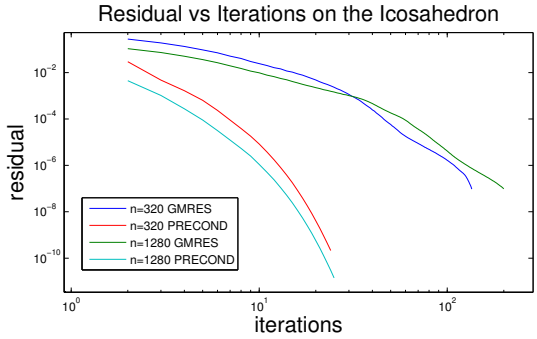


Figure 8.8: Residual of GMRES for icosahedron with 320, 1280 triangles.

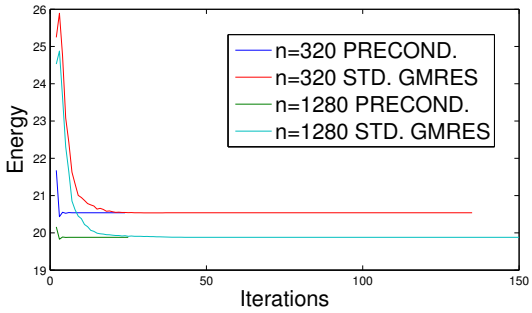


Figure 8.9: Energy convergence for icosahedron with 320, 1280 triangles.

**Example 3:** We now investigate plane-wave scattering from a screen, the square $\Gamma = [0, 0.5]^2 \times \{z = 0\} \subset \mathbb{R}^3$. Here one expects edge and corner singularities and a cor-

responding nonsmooth behaviour of the solution in time. The resulting effect on the preconditioner is of particular interest, as it is based on a Taylor expansion in time.

We again choose a plane wave right hand side $f(t, \mathbf{x}) = \exp(-4/t^2)\cos(\omega_f t - \mathbf{k}_f \mathbf{x})$, with $\mathbf{k}_f = (2, 2, 2)$ and $\omega_f = \|\mathbf{k}_f\|_2$. The square $\Gamma$ is discretized with uniform meshes of 288 and 1250 triangles, and we use corresponding time steps of $\Delta t = 0.1$, resp. 0.05, for the time interval $[0, T] = [0, 2.5]$. Figure 8.10 shows the mesh with 8 triangles as well as snapshots of the numerical solution for for 1250 triangles.

In Figure 8.11 we plot the number of iterations needed to achieve an error indicator as in Example 1 of $< 10^{-7}$ for increasing degrees of freedom. The number of iterations for the preconditioned GMRES is no longer stable, but grows with the DOF, though with a smaller exponent than without preconditioner.

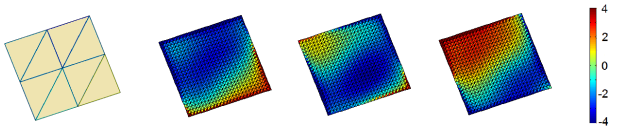


Figure 8.10: Meshes for screen with 8 and 1250 triangles.

Figure 8.12 shows the convergence of the residuals in each iteration for 288 and 1250 triangles, with and without preconditioner, while Figure 8.13 depicts the convergence of the energy. The results reconfirm the relevance of the preconditioner also for the less regular solutions that naturally arise on a screen. However, unlike for the closed surfaces of Examples 1 and 2, an application of the preconditioner or a single preconditioned GMRES iteration still yields a larger error in the energy of around 6% for 288 triangles and less than 3% for 1250 triangles, see Table 8.1.

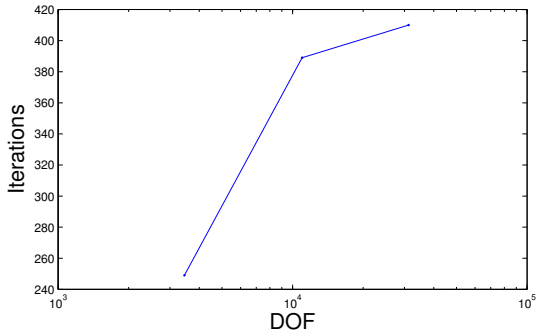


Figure 8.11: Iterations vs. DOF to achieve a residual $< 10^{-7}$ with preconditioned GMRES on the screen.

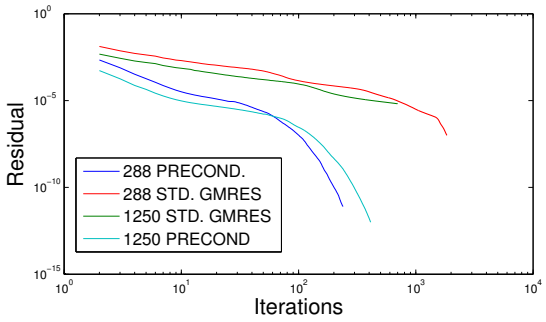


Figure 8.12: Residual of GMRES for screen with 288, 1250 triangles.

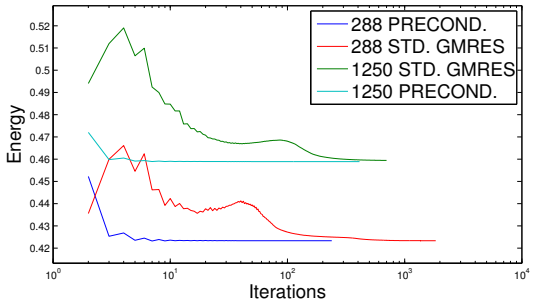


Figure 8.13: Energy convergence for screen with 288, 1250 triangles.

**Example 4:** We finally solve the space-time system for a partition of unity method based on ansatz and test functions of the form (8.6), with piecewise linear shape functions in time and piecewise constant shape functions in space. As in Example 2 we consider an icosahedron of diameter 2 centred in $\mathbf{0}$. The right hand side is given by $f(t, \mathbf{x}) = \exp(-25/t^2)\cos(\omega_f t - \mathbf{k}_f \mathbf{x})$, where $\mathbf{k}_f = (8.5, 3, 0.5)$ and $\omega_f = \|\mathbf{k}_f\|_2$. For the discretisation we consider the 20 faces of the icosahedron, depicted in Figure 8.6, and use

up to 15 travelling plane waves per triangle. We fix the time step $\Delta t = 0.1$ in the time interval $[0, T] = [0, 2.5]$.

In Figure 8.14 we plot the number of iterations needed until the standard residual error indicator for GMRES is smaller than $< 10^{-6}$ for increasing numbers of enrichments. A comparison between the residuals of GMRES and preconditioned GMRES for 15 enrichment functions is shown in Figure 8.15.

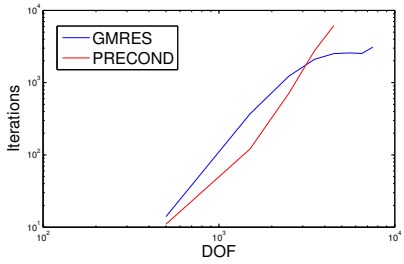


Figure 8.14: Iterations vs. DOF to achieve a residual $< 10^{-6}$ with a partition of unity method.

Even though the preconditioner is not justified here, it still significantly reduces the number of iterations for small numbers of enrichment functions. For larger numbers of enrichment functions, however, the reduction in the final iteration count becomes less clear. From Table 8.1, a simple application of the preconditioner reduces the energy error to 2.1% for 7, resp. 1% for 15 enrichment functions, much below the error of a single preconditioned GMRES iteration. Note that the partition of unity method leads to poorly-conditioned linear systems. So in addition to using an unjustified preconditioner, for larger degrees of freedom floating point errors become relevant. The condition number here (of the $V^0$ matrix) is up to $3.8 \times 10^{13}$.

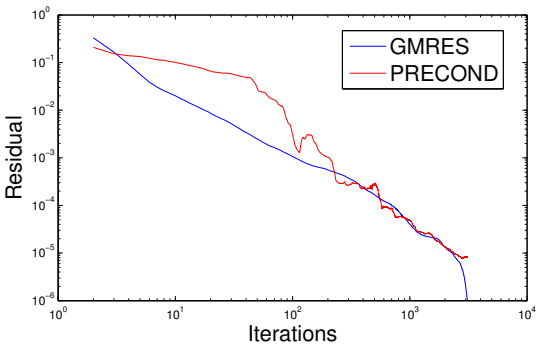


Figure 8.15: Residual of GMRES for the partition of unity method on the icosahedron with 15 enrichment functions per triangle.

# Chapter 9

# Conclusions

In this thesis we presented mesh refinements and high-order methods for the time domain boundary element method for the wave equation in $\mathbb{R}^3$. This work particularly discussed scattering problems for polyhedral scatterers or screens.

For the arising geometric singularities at edges and corners, an $h$-version on graded meshes was shown to recover optimal approximation rates for the solution to both Dirichlet and Neumann problems. The approach allowed accurate computations of the sound emission of tyres at a comparatively low number of degrees of freedom.

In order to approximate more general features of the solution, a reliable and efficient a posteriori error estimate provided the basis for adaptive mesh refinement procedures. It was shown that the resulting algorithms recovered the convergence rates known for time-independent problems. The a posteriori error estimate and many of the algorithmic aspects did not only apply to time domain BEM, but to general discretisations. They are therefore relevant also for alternative approaches such as convolution quadrature.

With a view towards smooth solutions, the thesis introduced high-order methods based on nonlinear basis functions, both a $p$-version of the time domain boundary element method with polynomials of higher order and a partition-of-unity method based on plane-wave enrichments. The $p$-version on the screen was shown to converge to the singular solution at twice the rate of the $h$-version, and for smooth solutions significantly improved rates were obtained as compared to the $h$-version. The partition-of-unity method showed significant reductions in examples for low degrees of freedom, but the correct shape of the enrichments in time-domain remains a challenging question for further study.

The systems arising in our work could often be solved efficiently with a time-stepping scheme based on linear extrapolation. For high accuracy the time-stepping scheme was used as a preconditioner in GMRES.

Further directions for future research may include space-time adaptivity, both $h$, $hp$ and with non-polynomial functions, and this thesis provides many of the foundations to do so. While the thesis was focused on the Dirichlet problem for the acoustic wave equation, extensions to other boundary conditions and coupled problems are explored within the research group. Extensions to linear elasticity and electromagnetism are of interest.

# Bibliography


[1] T. Abboud, P. Joly, J. Rodriguez, I. Terrasse, Coupling discontinuous Galerkin methods and retarded potentials for transient wave propagation on unbounded domains, Journal of Computational Physics, 230 (2011), 5877-5907

[2] A. Aimi, M. Diligenti, A. Frangi, C. Guardasoni, Energetic BEM-FEM coupling for wave propagation in 3D multidomains, Internat. J. Numer. Methods Engrg. 97 (2014), 377-394.

[3] A. Aimi, M. Diligenti, A. Frangi, C. Guardasoni, Neumann exterior wave propagation problems: computational aspects of 3D energetic Galerkin BEM, Comput. Mech. 51 (2013), 475-493.

[4] A. Aimi, M. Diligenti, C. Guardasoni, S. Panizzi, Energetic BEM-FEM coupling for wave propagation in layered media, Commun. Appl. Ind. Math. 3 (2012), 418-438.

[5] A. Aimi, M. Diligenti, A. Frangi, C. Guardasoni, A stable 3D energetic Galerkin BEM approach for wave propagation interior problems, Eng. Anal. Bound. Elem. 36 (2012), 1756-1765.

[6] A. Aimi, M. Diligenti, C. Guardasoni, On the energetic Galerkin boundary element method applied to interior wave propagation problems, J. Comput. Appl. Math. 235 (2011), 1746-1754.

[7] A. Aimi, M. Diligenti, C. Guardasoni, I. Mazzieri, S. Panizzi, An energy approach to space-time Galerkin BEM for wave propagation problems, Internat. J. Numer. Methods Engrg. 80 (2009), 1196-1240.

[8] A. Aimi, M. Diligenti, C. Guardasoni, Numerical integration schemes for the Galerkin BEM related to wave propagation problems, Quaderni Dip. Mat. Univ. Parma. 495, 1-34.

[9] E. Alarcon and A. Reverter, p-adaptive boundary elements, Internat. J. Numer. Methods Engrg. 23 (1986), 801-829.

[10] H. Antes, J. Baaran, Noise radiation from moving surfaces, Engineering Analysis with Boundary Elements 25 (2001), 725-740.

[11] I. Babuska, B. Q. Guo, Regularity of the solution of elliptic problems with piecewise analytic data. I. Boundary value problems for linear elliptic equation of second order, SIAM J. Math. Anal. 19 (1988), 172-203.

[12] I. Babuška, Finite element method for domains with corners, Computing 6 (1970), 264-273.

[13] I. Babuska and M. Suri, The optimal convergence rate of the p-version of the finite element method, SIAM J. Numer. Anal. 24 (1987), 750-776.

[14] I. Babuska, B. A. Szabo and I. N. Katz, The p-version of the finite element method, SIAM J. Numer. Anal. 18 (1981), 515-545.

[15] I. Babuška, R. B. Kellogg, J. Pitkäranta, Direct and inverse error estimates for finite elements with mesh refinements, Numer. Math. 33 (1979), 447-471.

[16] A. Bamberger, T. Ha Duong, Formulation variationnelle espace-temps pour le calcul par potentiel retard de la diffraction d'une onde acoustique. Math. Methods in the Appl. Sciences 8 (1986); 405–435 and 598–608.

[17] L. Banjai, M. Kachanovska, Fast convolution quadrature for the wave equation in three dimensions, J. Comp. Phys. 279 (2014), 103-126.

[18] L. Banjai, M. Schanz. Wave propagation problems treated with convolution quadrature and BEM. Lecture Notes Applied Computational Mechanics 63, Fast boundary element methods in engineering and industrial applications, pp. 145-184. Springer, (2012).

[19] L. Banjai, S. Sauter, Rapid solution of the wave equation in unbounded domains, SIAM J. Numer. Anal. 47 (2008/09), 227-249.

[20] L. Banjai, C. Lubich, F.-J. Sayas, Stable numerical coupling of exterior and interior problems for the wave equation, Numer. Math. 129 (2015), 611-646.

[21] L. Banjai, Time-domain Dirichlet-to-Neumann map and its discretisation, IMA J. Numer. Anal. 34 (2014), 1136-1155.

[22] L. Banz, H. Gimperlein, Z. Nezhi, E. P. Stephan. Time domain BEM for sound radiation of tires. Computational Mechanics 58 (2016), 45-57.

[23] E. Becache, T. Ha-Duong, A space-time variational formulation for the boundary integral equation in a 2d elastic crack problem, RAIRO 28 (1994), 141-176.

[24] A. Bespalov and N. Heuer, The p-version of the boundary element method for hypersingular operators on piecewise plane open surfaces, Numer. Math. 100 (2005), 185-209.

[25] A. Bespalov and N. Heuer, The p-version of the boundary element method for weakly singular operators on piecewise plane open surfaces, Numer. Math. 106 (2007), 69-97.

[26] J. H. Bramble, J. E. Pasciak, O. Steinbach, On the stability of the $L^2$ projection in $H^1(\Omega)$, Math. Comp. 71 (2002), 147-156.

[27] C. Carstensen, Efficiency of a posteriori BEM-error estimates for first-kind integral equations on quasi-uniform meshes, Math. Comp. 65 (1996), 6984.

[28] C. Carstensen, D. Praetorius, Averaging techniques for the effective numerical solution of Symm's integral equation of the first kind, SIAM J. Sci. Comp. 27 (2006), 1226-1260.

[29] C. Carstensen, E. P. Stephan, A posteriori error estimates for boundary element methods, Math. Comp. 64 (1995), 483-500.

[30] C. Carstensen, M. Maischak, E. P. Stephan, A posteriori error estimate and h-adaptive algorithm on surfaces for Symm's integral equation, Numer. Math. 90 (2001), 197-213.

[31] C. Carstensen, M. Maischak, D. Praetorius, E. P. Stephan, Residual-based a posteriori error estimate for hypersingular equation on surfaces, Numer. Math. 97 (2004), 397-426.

[32] J. Chabassier, A. Chaigne, P. Joly. Modeling and simulation of a grand piano, J. Acoustical Society of America, vol. 1 (2013), 666–685.

[33] S. N. Chandler-Wilde, I. G. Graham, S. Langdon, E. A. Spence. Numerical-asymptotic boundary integral methods in high-frequency acoustic scattering. Acta Numerics 21 (2012), 89-305.

[34] S. N. Chandler-Wilde, S. Langdon, L. Ritter. A high-wavenumber boundary element method for an acoustic scattering problem. Philosophical Transaction of the Royal Society A, vol. 362 (2004), 647-671.

[35] M. Costabel, Time-dependent problems with the boundary integral equation method. In Encyclopedia of Computational Mechanics, E. Stein, R. de Borst, and J. R. Hughes, Eds. John Wiley & Sons, Chichester, 2004, pp. 703-721.

[36] M. Costabel, Boundary integral operators on Lipschitz domains: elementary results, SIAM J. Math. Anal. 19 (1988), 613-626.

[37] T. A. Cruse, F. J. Rizzo. A direct formulation and numerical solution of the general transient elastodynamic problem, I. J. Math. Analysis Appl. 22:244-259, (1968).

[38] M. Dauge, Elliptic boundary value problems in corner domains, Lecture Notes in Mathematics 1341, Springer-Verlag, 1988.

[39] P. J. Davies, D. B. Duncan, Convolution-in-time approximations of time domain boundary integral equations, SIAM J. Sci. Comput. 35 (2013), B43–B61.

[40] P. J. Davies, D. B. Duncan, Convolution spline approximations for time domain boundary integral equations, J. Integral Equations Applications 26 (2014), 369–412.

[41] L. Demkowicz, Computing with *hp*-adaptive finite elements, Vol. 1, Chapman & Hall/CRC, 2007.

[42] Y. Ding, A. Forestier, T. Ha Duong, A Galerkin scheme for the time domain integral equation of acoustic scattering from a hard surface, J. Acoust. Soc. Am. 86 (1989), 1566–1572.

[43] M. R. Dorr, The approximation theory for the p-version of the finite element method, SIAM J. Numer. Anal. 21 (1984), 1180-1207.

[44] M. R. Dorr, The approximation of solutions of elliptic boundary-value problems via the p-version of the finite element method, SIAM J. Numer. Anal. 23 (1986), 58-77.

[45] M. Drolia, M. S. Mohamed, O. Laghrouche, M. Seaid, J. Trevelyan. Enriched finite elements for initial-value problem of transverse electromagnetic waves in time domain. Computers and Structures. 182, p. 354-367

[46] C. L. Epstein, L. Greengard, T. Hagstrom, On the stability of time domain integral equations for acoustic wave propagation, Discr. Continuous Dynamical Syst. 36 (2016), 4367–4382.

[47] V. Ervin, E. P. Stephan, A boundary-element method with mesh refinement for a weakly singular integral equation, Communications in Applied Numerical Methods 7 (1991), 273-280.

[48] V. Ervin, E. P. Stephan, An improved boundary element method for the charge density of a thin electrified plate in $\mathbb{R}^3$, Mathematical Methods in the Applied Sciences 13 (1990), 291-303.

[49] B. Faermann, Local a-posteriori error indicators for the Galerkin discretisation of boundary integral equations, Numer. Math. 79 (1998), 43-76.

[50] B. Faermann, Localization of the Aronszajn-Slobodeckij norm and application to adaptive boundary element methods. II. The three-dimensional case, Numer. Math. textbf92 (2002), 467-499.

[51] M. Filipe, Etude mathematique et numerique d'un probleme d'interaction fluide–structure dependant du temps par la methode de couplage elements finis – equations integrals, Ph.D. thesis, Ecole Polytechnique, 1994.

[52] M. Friedmann, R. Shaw, Diffraction of pulses by cylindrical obstacles of arbitrary cross section, J. Appl. Mech. 29 (1962), 40–46.

[53] T. P. Fries, T. Belytschko. The extended/generalised finite element method: An overview of the method and its applications. International Journal for Numerical Models in Engineering 84 (2010), 253-304.

[54] H. Gimperlein, M. Maischak, E. P. Stephan. Adaptive time domain boundary element methods and engineering applications. Journal of Integral Equations and Applications 29 (2017), 75-105.

[55] H. Gimperlein, F. Meyer, C. Oezdemir, E. P. Stephan. Time domain boundary elements for dynamic contact problems, Computer Methods in Applied Mechanics and Engineering 333 (2018), 147-175.

[56] H. Gimperlein, Z. Nezhi, E. P. Stephan. A priori error estimates for a time-dependent boundary element method for the acoustic wave equation in a half-space, Math. Methods in the Appl. Sciences 40 (2017), 448-462.

[57] H. Gimperlein, D. Stark. A partition-of-unity boundary element method for transient wave propagation, preprint.

[58] H. Gimperlein, C. Özdemir,D. Stark, E. P. Stephan, A residual a posteriori error estimate for the time domain boundary element method, preprint.

[59] H. Gimperlein, C. Özdemir, E. P. Stephan, Time domain boundary element methods for the Neumann problem and sound radiation of tires: Error estimates and acoustic problems, J. Comp. Mathematics, 36 (2018), 70-89.

[60] H. Gimperlein, E. P. Stephan, Analysis of a time–dependent FEM/BEM coupling method for fluid–structure interaction, draft.

[61] H. Gimperlein, F. Meyer, C. Oezdemir, D. Stark, E. P. Stephan, Boundary elements with mesh refinements for the wave equation, Numer. Math. (2018), to appear.

[62] H. Gimperlein, D. Stark, Algorithmic aspects of enriched time domain boundary element methods, submitted.

[63] H. Gimperlein, D. Stark, E. P. Stephan, A $p$-version boundary element method for the wave equation, in preparation.

[64] H. Gimperlein, D. Stark, Extrapolation as preconditioner for time domain boundary element methods, preprint.

[65] H. Gimperlein, D. Stark, A partition-of-unity boundary element method for transient wave propagation, preprint.

[66] M. Gläfke, Adaptive Methods for Time Domain Boundary Integral Equations. Ph.D. thesis, Brunel University, 2012.

[67] M. Gläfke, M. Maischak, Regularity of 2D time domain boundary integral operators, preprint.

[68] M. Gläfke, M. Maischak, Wave-number explicit generalised mapping properties for Helmholtz boundary integral operators , applied to time domain boundary integral operators, preprint.

[69] J. Gwinner, E. P. Stephan, Advanced Boundary Element Methods – Treatment of Boundary Value, Transmission and Contact Problems, draft of book (2017).

[70] T. Ha Duong, B. Ludwig and I. Terrasse, A Galerkin BEM for transient acoustic scattering by an absorbing obstacle, Internat. J. Numer. Methods Engrg. 57 (2003), 1845–1882.

[71] T. Ha Duong. On retarded potential boundary integral equations and their discretisations. Topics in computational wave propagation, Lect. Notes Comput. Sci. Eng., Vol. 31. Springer: Berlin, 301336.

[72] T. Ha-Duong, Equations integrales pour la resolution numerique de preblemes de diffraction d'onded acoustiques dans $\mathbb{R}^3$, Ph.D. thesis, Université Pierre et Marie Curie Paris (1987).

[73] T. Ha-Duong, On the transient acoustic scattering by a flat object, Japan J. Appl. Math. 7 (1990), 489-513.

[74] C. Hager, P. Hauret, P. Le Tallec, B. I. Wohlmuth, Solving dynamic contact problems with local refinement in space and time, Comput. Methods Appl. Mech. Engrg. 201/204 (2012), 25-41.

[75] S. Ham, K.J. Bathe, A Finite Element Method Enriched For Wave Propagation Problems, Computers And Structures 94-95 (2012), 1-12.

[76] G. D. Hatzigeorgiou, D. E. Beskos. Dynamic inelastic structural analysis by the BEM: A review. Engineering Analysis with Boundary Elements, 35:159-169, (2011).

[77] P. Hauret, J. Salomon, A. A. Weiss, B. I. Wohlmuth, Energy-consistent corotational schemes for frictional contact problems, SIAM J. Sci. Comput. 30 (2008), 2488-2511.

[78] N. Heuer, M. Maischak, and E. P. Stephan, Exponential convergence of the *hp*-version for the boundary element method on open surfaces, Numer. Math. 83 (1999), 641-666.

[79] D. P. Hewett, S. Langdon, N. Chandler-Wilde, A Frequency-independent Boundary Element Method for Scattering by Two-Dimensional Screens and Apertures, IMA Journal of Numerical Analysis 35 (2015), 1698-1728.

[80] H. Holm, M. Maischak, E. P. Stephan, The hp-version of the boundary element method for Helmholtz screen problems, Computing 57 (1996), 105-134.

[81] G. C. Hsiao, T. Sanchez-Vizuet, F.-J. Sayas, Boundary and coupled boundary-finite element methods for transient wave-structure interaction. IMA J. Numer. Anal. 37 (2017), 237-265.

[82] G. C. Hsiao, F.-J. Sayas, R. J. Weinacht, Time-dependent fluid-structure interaction. Math. Meth. Appl. Sci. 40 (2017), 486-500.

[83] M. Iqbal, H. Gimperlein, M. S. Mohamed, O. Laghrouche. An a posteriori error estimate for the generalised finite element method for transient heat diffusion problems. International Journal for Numerical Methods In Engineering 110 (2017), 1103-1118.

[84] A. Y. Kokotov, P. Neittaanmäki, B. A. Plamenevskiĭ, The Neumann problem for the wave equation in a cone, J. Math. Sci. 102 (2000), 4400-4428.

[85] A. Y. Kokotov, P. Neittaanmäki, B. A. Plamenevskiĭ, Diffraction on a cone: The asymptotics of solutions near the vertex, J. Math. Sci. 109 (2002), 1894-1910.

[86] A. Y. Kokotov, P. Neittaanmäki, B. A. Plamenevskiĭ, On the asymptotic behavior of solutions of the Neumann problem for hyperbolic systems in domains with conical points, Algebra i Analiz 16 (2004), 56-98.

[87] W. Kropp, F. X. Becot, S. Barrelet, On the sound radiation from tyres, Acta Acustica united with Acustica 86 (2000), 769-779.

[88] O. Laghrouche, P. Bettess, E. Perrey-Debain, J. Trevelyan. Wave interpolation fine elements for Helmholtz problems with jumps in the wave speed. Computer Methods in Applied Mechanics and Engineering, 194(2):367-381, (2005).

[89] M. Maischak, E. Ostermann, E. P. Stephan, TD-BEM for Sound Radiation in three Dimensions and the Numerical Evaluation of Retarded Potentials, International Conference on Acoustics, NAG/DGA. 2009.

[90] M. Maischak, E. P. Stephan, The h-p-version of the BEM with geometric meshes in 3D, Boundary Element Topics (1997), 351-362.

[91] M. Maischak, Manual of the software package maiprogs, Version 3.7.1 ed., August, 2012.

[92] W. J. Mansur, A time-stepping technique to solve wave propagation problems using the boundary element method, Ph.D. thesis, University of Southampton, 1983.

[93] S. I. Matyukevich, B. A. Plamenevskiĭ, On dynamic problems in the theory of elasticity in domains with edges, Algebra i Analiz 18 (2006), 158-233.

[94] V. G. Mazya, J. Rossmann, Elliptic equations in polyhedral domains, Mathematical Surveys and Monographs, Vol. 162, American Mathematical Society, Providence, RI, 2010.

[95] J. M. Melenk, I. Babuska. The partition of unity finite element method: Basic theory and applications. Computer Methods in Applied Mechanics and Engineering, 139(1):289-314, (1996).

[96] J. M. Melenk, I. Babuska. The partition of unity method. International Journal for Numerical Methods in Engineering, 40:727-758, (1997).

[97] M. S. Mohamed, M. Seaid, J. Trevelyan, O. Laghrouche. A partition of unity FEM for time-dependent diffusion problems using multiple enrichment functions. International Journal for Numerical Methods in Engineering 93 (2013), 245-265.

[98] F. Müller, C. Schwab, Finite Elements with mesh refinement for wave equations in polygons, J. Comp. Appl. Math. 283 (2015), 163-181.

[99] Z. Nezhi, Adaptive Time Domain Boundary Element Method for Sound Radiation of tires, Ph.D. thesis, Leibniz Universität Hannover, 2014.

[100] M. Ochmann, The complex equivalent source method for sound propagation over an impedance plane, J. Acoust. Soc. Am. 116 (6), 2004.

[101] M. Ochmann, Closed form solutions for the acoustical impulse response over a masslike or an absorbing plane, J. Acoust. Soc. Am. 129 (6), 2011.

[102] E. Ostermann, Numerical Methods for Space-Time Variational Formulations of Retarded Potential Boundary Integral Equations, Ph.D. thesis, Leibniz Universität Hannover, 2009.

[103] E. Perrey-Debain, J. Trevelyan, P. Bettess. Wave boundary elements: A theoretical overview presenting applications in scattering of short waves. Engineering Analysis with Boundary Elements 28 (2004), 131-141.

[104] E. Perrey-Debain, J. Trevelyan, P. Bettess. On Wave Boundary Elements for Radiation and Scattering Problems with Piecewise Constant Impedance. IEEE Transactions on Antennas and Propagation 53 (2005), 876-879.

[105] B. A. Plamenevskiĭ, On the Dirichlet problem for the wave equation in a cylinder with edges, Algebra i Analiz 10 (1998), 197-228.

[106] K. M. Rasmussen, S. R. K. Nielsen, P. H. Kirkegaard, Boundary element method solution in the time domain for a moving time-dependent force, Computers and Structures 79 (2001), 691-701.

[107] B. Sako, A model for the Crack and Punch Problems in Elasticity, Ph.D. thesis, University of California, Los Angeles (1986).

[108] F. J. Sayas. Retarded potentials and time domain boundary integral equations: a road-map. Springer Series in Comp. Math. 50, Springer (2016).

[109] S. Sauter, A. Veit, Adaptive time discretisation for retarded potentials, Numer. Math. 132 (2016), 569-595.

[110] S. Sauter, C. Schwab, Boundary Element Methods, Springer Series in Computational Mathematics 39, Springer, 2011.

[111] S. Sauter, M. Schanz, Convolution quadrature for the wave equation with impedance boundary conditions, J. Comp. Phys. 334 (2017), 442-459.

[112] C. Schwab, $p$- and $hp$- finite element methods: theory and applications in solid and fluid mechanics, Oxford University Press, 1998.

[113] G. E. Stavroulakis, H. Antes, P. D. Panagiotopoulos, Transient elastodynamics around cracks including contact and friction, Computer Methods in Applied Mechanics and Engineering 177 (1999), 427-440.

[114] O. Steinbach, Stability estimates for hybrid coupled domain decomposition methods, Lecture Notes in Mathematics 1809, Springer, 2003.

[115] E. P. Stephan, M. Maischak, E. Ostermann, Transient boundary element method and numerical evaluation of retarded potentials, Computational Science–ICCS, 2008.

[116] E. P. Stephan and M. Suri, On the convergence of the $p$-version of the boundary element Galerkin method, Math. Comp. 52 (1989), 31-48.

[117] T. Strouboulis, I. Babuska, R. Hidajat. The generalized finite element method for Helmholtz equation: Theory, computation, and open problems. Computer Methods in Applied Mechanics and Engineering, 195(37):4711-4731, (2006).

[118] T. Strouboulis, R. Hidajat, I. Babuska. The generalized finite element method for Helmholtz equation part ii: Effect of choice on handbook functions, error due to

absorbing boundary conditions and its assessment. Computer methods in Applied Mechanics and Engineering, 197(5):364-380, (2008).

[119] G. Sylvand, La Methode Multipole Rapide en Electromagnetisme: Performances, Parallelisation, Applications, Ph.D. thesis, Ecole Nationale des Ponts et Chaussees, 2002.

[120] I. Terrasse. Resolution mathematique et numerique des equations de Maxwell instationnairs par une methode de potentiels retardes. Ph.D. thesis, Ecole Polytechnique, (1993).

[121] A. Veit, Numerical methods for the time domain boundary integral equations, Ph.D. thesis, Universität Zürich, 2011.

[122] A. Veit, M. Merta, J. Zapletal, D. Lukas, Efficient solution of time domain boundary integral equations arising in sound hard scattering, Internat. J. Numer. Meth. Eng. 107 (2016), 430-449.

[123] O. von Estorff et al., Abschlussbericht SPERoN 2020 – Teil II, Entwicklung einen performanten Rechenmodells zur Berechnung und Reduzierung der Geruschabstrahlung von Reifen, 2014.

[124] T. von Petersdorff, Randwertprobleme der Elastizitätstheorie für Polyeder-Singularitäten und Approximation mit Randelementmethoden, Ph.D. thesis, Technische Universität Darmstadt (1989).

[125] T. von Petersdorff, E. P. Stephan, Regularity of mixed boundary value problems in $\mathbb{R}^3$ and boundary element methods on graded meshes, Math. Methods Appl. Sci. 12 (1990), 229-249

[126] T. von Petersdorff, E. P. Stephan, Decompositions in edge and corner singularities for the solution of the Dirichlet problem of the Laplacian in a polyhedron, Math. Nachr. 149 (1990), 71-103.

[127] T. von Petersdorff, E. P. Stephan, Singularities of the solution of the Laplacian in domains with circular edges, Appl. Analysis 45 (1992), 281-294.

[128] W. Wendland, D. Yu, Adaptive boundary element methods for strongly elliptic integral equations, Numer. Math. 53 (1988), 539-558.

[129] A.E. Yilmaz, J.-M. Jin, E. Michielssen. Time domain adaptive integral method for surface integral equations. IEEE Transactions on Antennas and Propagation 52 (2004), 2692 – 2708.